2013-07-03

Characterization of InGaAs Quantum Dot Chains

Tyler Drue Park
Brigham Young University - Provo

Characterization of InGaAs Quantum Dot Chains

Tyler Park

A thesis submitted to the faculty of
Brigham Young University
in partial fulfillment of the requirements for the degree of

Master of Science

John Colton, Chair
Karine Chesnel
Richard Vanfleet

Department of Physics and Astronomy

Brigham Young University

July 2013

ABSTRACT

Characterization of InGaAs Quantum Dot Chains

Tyler Park
Department of Physics and Astronomy, BYU
Master of Science

InGaAs quantum dot chains were grown with a low-temperature variation of the Stranski-Krastanov method, the conventional epitaxial method. This new method seeks to reduce indium segregation and intermixing in addition to giving greater control in the growth process. We used photoluminescence spectroscopy techniques to characterize the quality and electronic structure of these samples. We have recently used a transmission electron microscope to show how the quantum dots vary with annealing temperature. Some questions relating to the morphology of the samples cannot be answered by photoluminescence spectroscopy alone. Using transmission electron microscopy, we verified flattening of the quantum dots with annealing temperature and resolved the chemical composition with cross-section cuts and plan view cuts.

Keywords: masters thesis, quantum dots, quantum dot chains, InGaAs, transmission electron microscopy

ACKNOWLEDGMENTS

I would like to thank Felipe Rivera and Thomas McConkie, who helped me earlier in the project to produce my cross-section cuts, spending many hours just trying to figure out what to do. Also I'd like to acknowledge Dr. Jeff Farrer, who has spent months helping me to prepare and image samples; and Dr. Richard Vanfleet for helping me prepare the most recent plan view cuts. I would also like to thank my advisor who has spent hours helping me proofread this thesis.

Contents

Table of Contents **iv**

1 Introduction **1**
1.1 Overview . . . 1
1.2 Background . . . 2
1.2.1 Nanostructures . . . 2
1.2.2 A Two Quantum Well Example . . . 5
1.2.3 Epitaxial Techniques . . . 7
1.2.4 Similar Work . . . 8
1.2.5 Sample Growth . . . 9
1.2.6 Summary . . . 11

2 Techniques **12**
2.1 Photoluminescence . . . 12
2.1.1 Technique . . . 14
2.2 Transmission Electron Microscopy . . . 15
2.2.1 Sample Preparation . . . 20

3 Photoluminescence Results **26**
3.1 Optical Properites of QDs Induced by Annealing . . . 26
3.1.1 Summary . . . 26
3.1.2 Sample Growth . . . 27
3.1.3 Method . . . 28
3.1.4 Measurements and Discussion . . . 29
3.1.5 Conclusion . . . 33

4 TEM Results **34**
4.1 Cross-Section Results . . . 34
4.1.1 Identifying the QD Layer . . . 34
4.1.2 Chemical Analysis . . . 35
4.2 Plan View Results . . . 36
4.2.1 Measurements . . . 39

4.2.2 Cross-section Measurements 39
4.3 Interpretation 42

5 Conclusion **45**

Bibliography **47**

A MATLAB Code for a Dual-Well System **56**

B Characterization of Nickel Nanostrand Nanocomposites Through Dielectric Spectroscopy and Nanoindentation **60**

C T_1 Spin Lifetime Measurements **69**

D Critical annealing temperature for optical properties of InGaAs quantum nanostructures **77**

Index **85**

Chapter 1

Introduction

1.1 Overview

Since the early 1990s, there has been a rising fascination in the scientific community with quantum nanostructures, most particularly, the quantum dot (QD) [1]. Although the theory and manufacturing techniques for quantum dots have been around for decades, we are just now beginning to see new uses for these structures in electronics and other technologies.

This thesis work focuses on a set of controlled-growth QD samples received from Dr. Haeyeon Yang[1], where the dots form in chain structures. The purpose of this study is to verify the nature of epitaxially grown InGaAs quantum dot chains which has not been verifiable using photoluminescence spectroscopy or scanning tunneling microscopy prior to its capping layer deposition. It is possible that the GaAs capping layer may alter the nature of the dots, such as geometry or chemical properties [2]. Morphological characterization was done by using a transmission electron microscope (TEM).

Other students have reported on some results of our photoluminesence spectroscopy experiments and time-resolved photoluminesence experiments [3,4]. A summary of those results will be

[1] Collaborator now working at South Dakota School of Mines and Technology

included.

The transmission electron microscope helped us to verify a number of things: the nature of the wetting layer after post-capping growth, the distribution of the quantum dots, the segregation of the indium, and the sizes of the dots.

Quantum dots generally have a wide range of applications, such as infrared lasers [5], infrared detectors [6], electro-optical devices [7], and quantum computing [8]. These technologies can be achieved by increasing our understanding of their physical and electrical properties and further researching proper growth techniques. For example, by changing physical attributes of the quantum dots, one is able to make the dots emit a tunable wavelength of light. By controlling the homogeneity of the size, spacing and composition of the quantum dots, one controls the quality of the produced light. Numerous growth techniques are used for greater control of the geometry and chemical composition of quantum dots.

1.2 Background

1.2.1 Nanostructures

Nanostructures are structures in which one or more critical dimensions are on a nanometer scale. Although the possibilites of such structures are many, I will only review three main structures that restrict carriers in multiple dimensions. A quantum well constricts carriers in one dimension, allowing them ideally to move freely in the other two dimensions. This is done by creating a potential barrier around the well region. In class III-V semiconductor quantum wells, the potential barrier is made by surrounding the well layer with another semiconducting medium that has a larger band gap. The charge carriers are restricted electronically by the surrounding medium's band structure, therefore they are confined in the well unless they have the energy to overcome the potential barrier. See Figure 1.1.

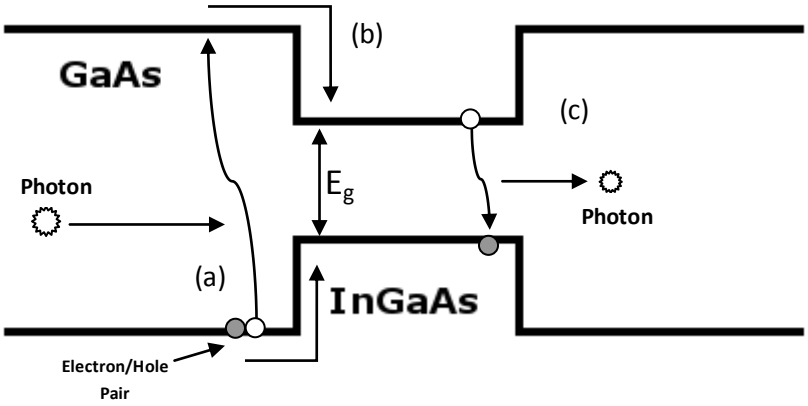

Figure 1.1 A simplified band gap and photoluminescence process diagram for a quantum well/dot. The photon is absorbed by the GaAs (a) exciting electrons across the bandgap, leaving behind a hole. The electron and hole falls into the InGaAs structure since the energy states are below that of GaAs (b). The carriers become confined in the central region (well) unless they have enough energy to overcome the barrier. However, the electron may relax and recombine with a hole. As the electron recombines with its hole, it releases a photon (c) corresponding to the band gap energy of InGaAs.

A quantum wire constricts two dimensions, allowing transport in only one dimension. A quantum dot constricts in all three spatial dimensions, essentially trapping the carriers in a local region.

The growth techniques of these structures have been extensively studied [10]. One technique is lithography, which is writing or printing the nanostructures by using a beam of electrons, photons, or ions to generate an exposure pattern, or creating an exposure mask, onto which additional layers may be grown [11]. Another method is chemical etching, which removes part of the material to produce the needed geometry [12, 13].

Growth conditions and uses for quantum dot chains have been studied recently [14–19]. Quantum dot chains are quantum dots grown closer in one dimension than the other, creating rows of nearly-connected dots. Different shapes such as quantum dashes and quantum wires have also been reported by others in the community [20].

Quantum dot arrays or quantum dot chains look like promising candidates for transferring quantum information in applications such as quantum computing or spintronics due to their ability to couple with neighboring dots [21]. This effect is shown in section 1.2.2.

Nickel Nanostrands

Although the main focus of my research deal with characterizing quantum dot chains, I have been involved in other projects characterizing nanostructures. One of which was a collaborative project with mechanical engineering student Michael Koecher, a graduate student from David Fullwood's group, that characterized nickel nanostrand (a type of nanowire) nanocomposites through dielectric spectoscopy [22]. Dielectric spectroscopy is a method that measures dielectric properties of a material as a function of frequency. We measured the capacitances to deduce the junction distance between conductive particles in a dielectric medium with an impedance analyzer at various frequences between 5 Hz and 13 MHz. The data recorded was then fitted to a theorectical model known as the Cole-Cole equation to yield some of the parameters used to find the junction distance:

$$\varepsilon^*(\omega) - \varepsilon_\infty = \frac{\Delta\varepsilon}{1 + (i\omega\tau)^{1-\alpha}} \tag{1.1}$$

where $\varepsilon^*(\omega) - \varepsilon_\infty$ is the measured dielectric constant, $\Delta\varepsilon$ describes the relative dielectric constant in the limit as the frequency ω goes to 0, τ is a time constant, and α is the exponent parameter [23]. Other necessary parameters for this model, such as barrier height, were found by Koecher's collaborators at Los Alamos National Laboratories. To find out the junction distance, we used the equation derived by Fritzsche et al. [24] based on the tunneling resistivity in the barrier between two conductive particles:

$$\frac{1}{\tau} = \frac{3e^2}{16\pi^2\hbar\varepsilon_0}\frac{k_0}{\varepsilon}\exp(-k_0\delta) \tag{1.2}$$

where e is the charge of an electron, ε is the relative permittivity, $k_0 = 4\pi\sqrt{2m_e\lambda}/\hbar$, λ is the barrier height, and δ is the junction distance.

The published paper (Ref. [22]) based on our measurements can be found in Appendix B of this thesis.

T_1 Spin Lifetime Measurements

Another project I was involved in was our research group's work on T_1 spin lifetime measurements of a 14 nm (100) GaAs quantum well [25]. This utilized the Kerr effect or Kerr rotation, which is a magnetic effect that rotates the polarization of light [26]. By tuning the wavelength of our Ti:Sapph probe laser and maximizing the Kerr rotation signal received, we located the resonant wavelength of the well. By tuning a time-resolved pump-probe Kerr rotation technique as described in reference [27], we were able to measure the spin decays at various fields. We studied the spin decays at both 5K and 1.5K. Spin lifetimes from 44 ns to 170 ns were measured at 5 K, and lifetimes from 44 ns to 1040 ns were measured at 1.5 K. These lifetimes significantly exceeded values in associated articles quoted in reference [25].

The published paper (Ref. [27]) based on our experiments can be found in Appendix D of this thesis. Additional information about the measurement technique can be found in Ref. [25].

1.2.2 A Two Quantum Well Example

In order to show how two wells/dots placed close together allow for transport of electrons from one well to the next, I present the following model. There are numerous examples of quantum well models in textbooks. One such model I wish to bring up is a double-well/single-barrier model as shown in Numerical Methods for Physics by Garcia [28, p. 293, problem 9.15]. I have changed the code slightly so that a barrier exists at the origin in addition to the edges of the plot (x = $\pm$50). The code may be found in Appendix A. Running this with 100 grid points, 0.1 time step, and 0.1

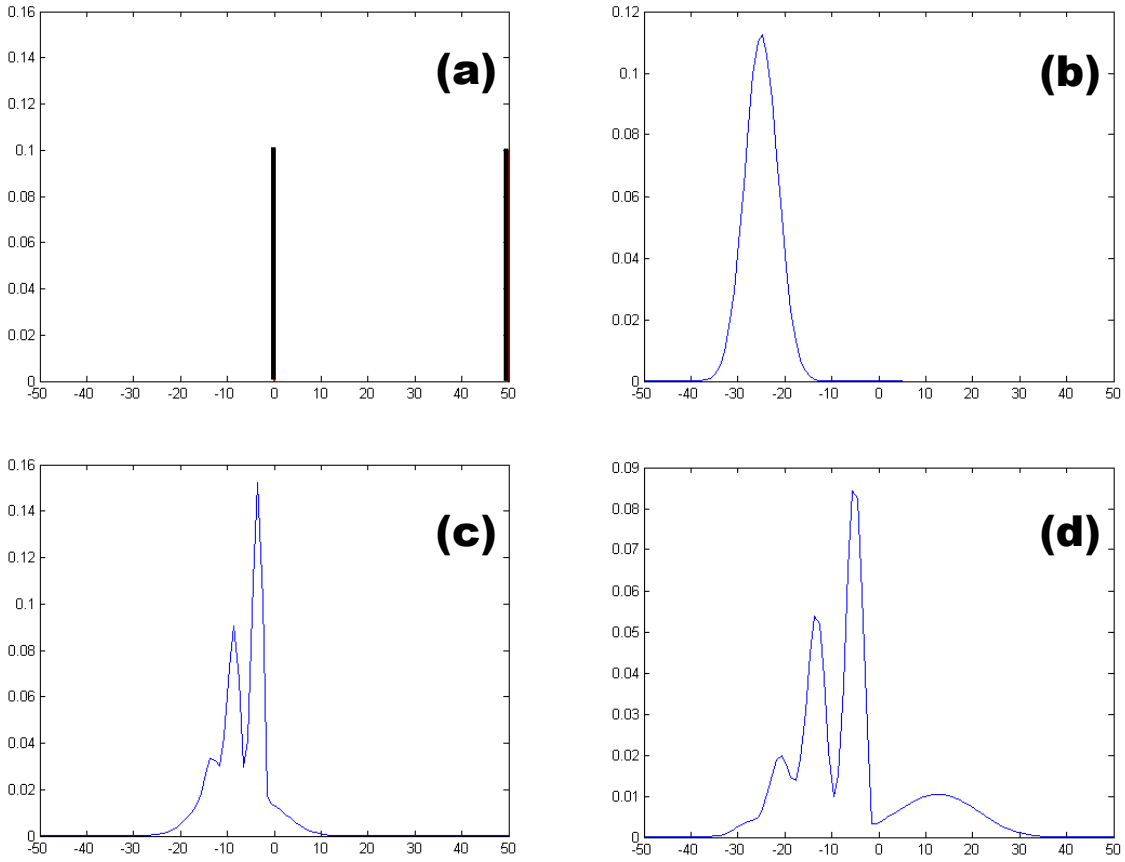

Figure 1.2 A two-well computational model with a barrier at x=0 as seen in the potential plot in (a). (b) The particle, represented by the gaussian distribution, approaches the barrier. (c) The particle interacts with the barrier, and (d) we see there is a probability of having the particle tunnel through to the next well. The x-axis for these graphs uses arbitrary units of space, and the y-axis uses arbitrary units, such that $|\psi^*\psi|$ integrated over all space equals 1.

for the delta potential amplitude, I get the following results. Also notice in the code that mass and $\hbar$ are both unitized.

A particle with forward momentum at t = 0 approaches the barrier. The plot shown in Figure 1.2 is the particle's magnitude-squared wavefunction, such that it represents the probability of finding the particle at that location in x (i.e. $\psi^*\psi$). Since the barrier is high and infinitely narrow, there is

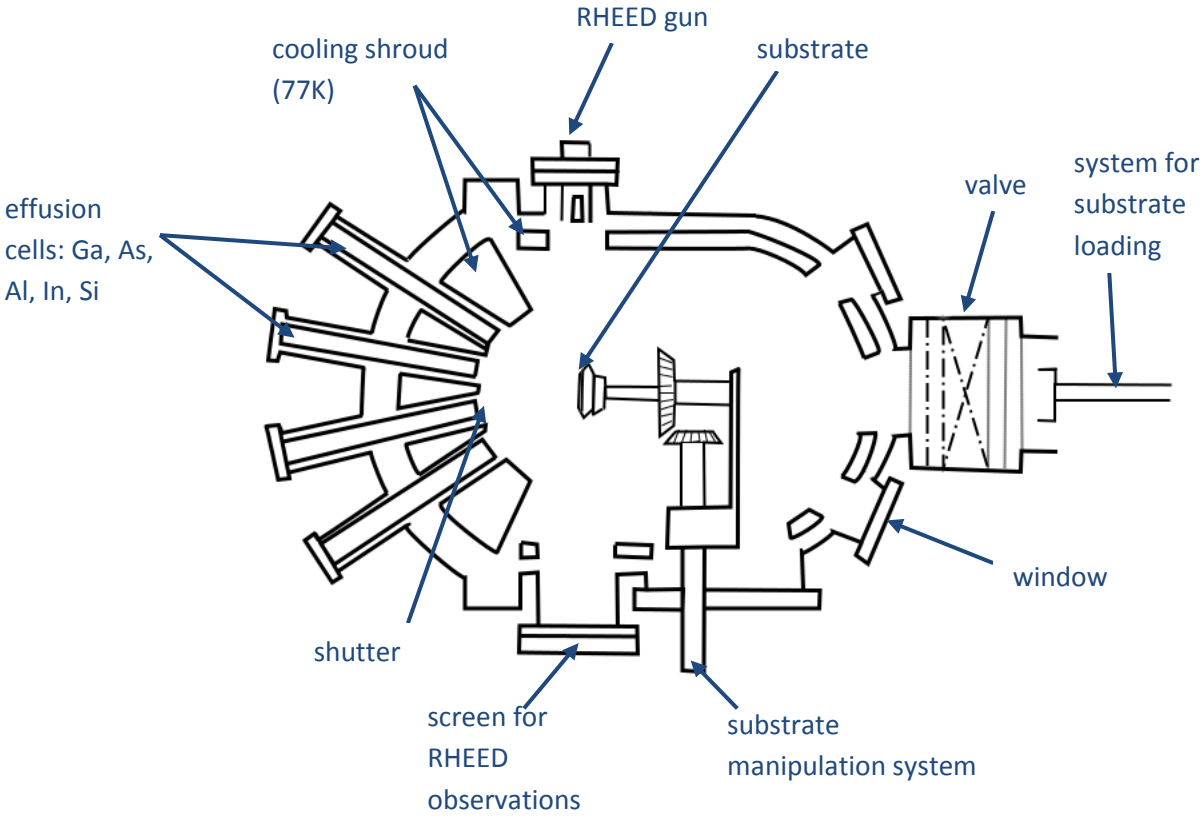

Figure 1.3 Diagram of a typical MBE machine.[i]

a probability that the particle will tunnel through the barrier, although it may be much smaller than the probability that it stays in its current well.

In the case with our quantum dot chains, obviously the barriers are not infinitely narrow or high, but the principle still applies that there is a probability for a particle in one quantum dot to transport into a neighboring dot.

1.2.3 Epitaxial Techniques

Molecular beam epitaxy (MBE) is a popular technique for growing quantum nanostructures. This involves placing a substrate in an environmentally-controlled (temperature-controlled and ultra-high vacuum) chamber and allowing atoms of various elements (e.g. In, Ga, As, Si, or Al) to

be deposited layer upon layer on the substrate by thermal diffusion. MBE is considered a slow process, ensuring a controlled epitaxial growth [29, 30]. A diagram of an MBE machine is shown in Figure 1.3

Of the primary methods used in epitaxy, the Stranski-Krastanov method is the most widely used. The Stranksi-Krastanov method, or the S-K method, involves depositing layers of atoms or molecules with a larger lattice parameter than the substrate's onto the substrate base, forming an initial wetting layer. After adding several monolayers to the wetting layer, the strain in the wetting layer will grow due to the difference in lattice parameters. At a critical thickness, the wetting layer lattice will buckle and form islands. These islands are the quantum dots. The materials used must be chosen so that the surrounding medium has a larger bandgap energy than the wetting layer materials; this ensures that a barrier effect is set up.

Our quantum dots were grown using a modified S-K technique. By growing the wetting layer on the (100) substrate face at a lower temperature (around 380°C), it prevents atomic rearrangement so the dots do not form yet. A post-annealing process is added which allows the quantum dots to form. This provides greater control in the growth process with the annealing temperature and wetting layer thickness. Further details of the growth process will be given in section 1.2.5.

The modified S-K growth process was observed in-situ using reflection high-electron energy diffraction (RHEED), which is a feature of the MBE machine used. Electrons are projected at the surface and scatter off to create a diffraction pattern. If the pattern develops pairs of streaks in the diffraction pattern, known as chevrons, this indicates the successful growth of quantum dots [31].

1.2.4 Similar Work

The Stranski-Krastanov (SK) method was invented in 1938, although it wasn't of much use until decades later [32]. In more recent decades, the popularity of quantum nanostructures has grown. The SK method has become a common method for producing epitaxial quantum dots and has been

extensively researched [5, 9, 33–36].

Control over the shapes and sizes of quantum dots have also been studied. Leonard et al. has looked at in situ techniques for controlling the uniformity of self-assembled dots and critical thickness of the wetting layer [33, 34]. Also recently, quantum dashes have been looked at and a relation between InAs layer thickness and dash size has been found [37].

In addition to collaborator Haeyeon Yang, whose technique is described in more detail below, Z. M. Wang and J. H. Lee have also been able to grow quantum dot chains on a pre-patterned substrate [14, 16, 38]. This has resulted in more uniform chains than what we see on our samples.

1.2.5 Sample Growth

Our samples were grown by Haeyeon Yang in an MBE machine equipped with a computer-controlled valved arsenic cracker cell and an *in situ* ultra high vacuum STM. The valved arsenic cracker cell aids in the material growth and repeatability by eliminating oxidation. The three samples examined for this thesis were labeled 032607A, 032607B, and 032907. The number corresponds to the date (032607 is March 26, 2007), and the letter corresponds to the order produced on the day the samples were grown.

In Yang's growth process, the wetting layer was grown at a cooler temperature compared to the S-K method, temporarily suppressing the otherwise expected 3D island formation. This low-temperature technique has advantages such as more uniform indium dispersion [39] and suppression of desorption [40] among others.

Kim and Yang found a low-temperature growth method with a high-temperature annealing process for controlling the shapes of the quantum dots [20]. Varying the wetting layer thickness prior to annealing (among other parameters) produces different magnitudes of strain in the lattice. This strain can dictate the shape of the nanostructures. In the case of our samples, the wetting layer was grown so that the nanostructures formed into quantum dot chains.

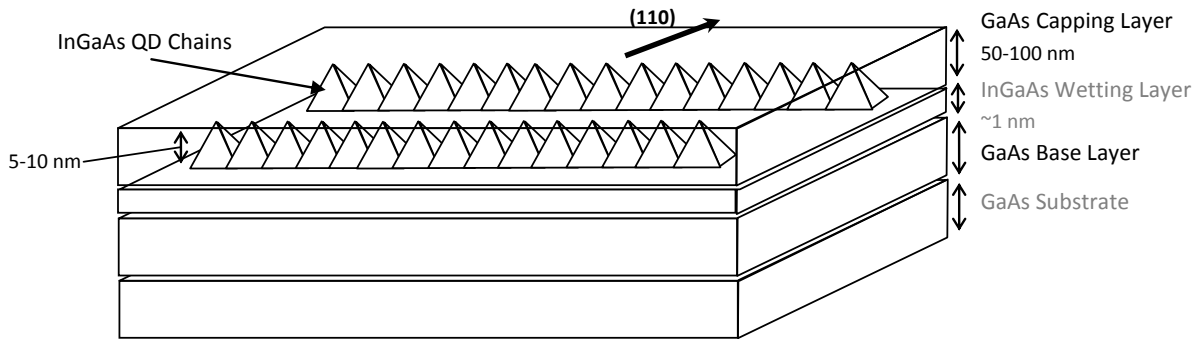

Figure 1.4 Example diagram of one of our samples.

For sample 032607A, the InGaAs wetting layer was grown to a thickness of 10 ML during 47 seconds with the arsenic gas cracker valve at 25%. It then went through an annealing process at 460°C. Sample 032607B was grown under similar conditions, except that it was annealed at 500°C with the arsenic valve at 40%. Sample 032907 was annealed at 480°C with the arsenic valve at 25%. For all three samples, a 100 nm thick GaAs capping layer was added, which is a necessity for electrical and optical purposes [2]. An example diagram of these samples can be found in Figure 1.4.

The Issue of Segregation and Intermixing

In the conventional S-K method, we see a problem arise with indium segregation and intermixing [36, 41]. Indium tends to clump, which leads to a thin layer of indium on the QD structure and wetting layer, or an area at the top of the dot with a high density of indium as was seen in Ref. [36]. Indium also has been known to seep into the substrate from the wetting layer, causing the strain to be less abrupt for QD formation, as seen in Ref. [41]. Yang's modified S-K method seeks to minimize these effects.

1.2.6 Summary

The upcoming chapters will address the setup and results of our group's photoluminescence spectroscopy experiments and of my TEM project. Chapter 2 introduces photoluminescence spectroscopy and our experimental technique. It will also cover TEM theory and my approach in preparing the samples for TEM imaging. Chapter 3 summarizes the photoluminescence results. Chapter 4 summarizes the TEM imaging results. The final chapter concludes this thesis.

Chapter 2

Techniques

2.1 Photoluminescence

Since quantum dots emit at discrete photon energies, photoluminescence (PL) spectroscopy is an ideal way to characterize the dots. By probing the QD samples with a laser with larger energy (smaller wavelength) than the barrier material's band gap, carriers are excited across the band gap and fall into the quantum dot material. When the carriers relax, they emit photons corresponding to the nature of the quantum dots [35, 42].

The light emitted from the quantum dot sample is then collected and passed into a monochromator and to a detector. The signal is then sent to a computer controlling the monochromator, scanning through a range of wavelengths, and recording the detector's voltage output corresponding to the wavelength. The data is then plotted, producing the sample's output spectrum. Possible variations of this technique include time-resolved, temperature dependent, or laser power dependent photoluminescence measurements.

Of particular interest in our photoluminescence experiments is attempting to observe the state-filling effect, which indicates high-quality dots. The state-filling effect happens when a high inten-

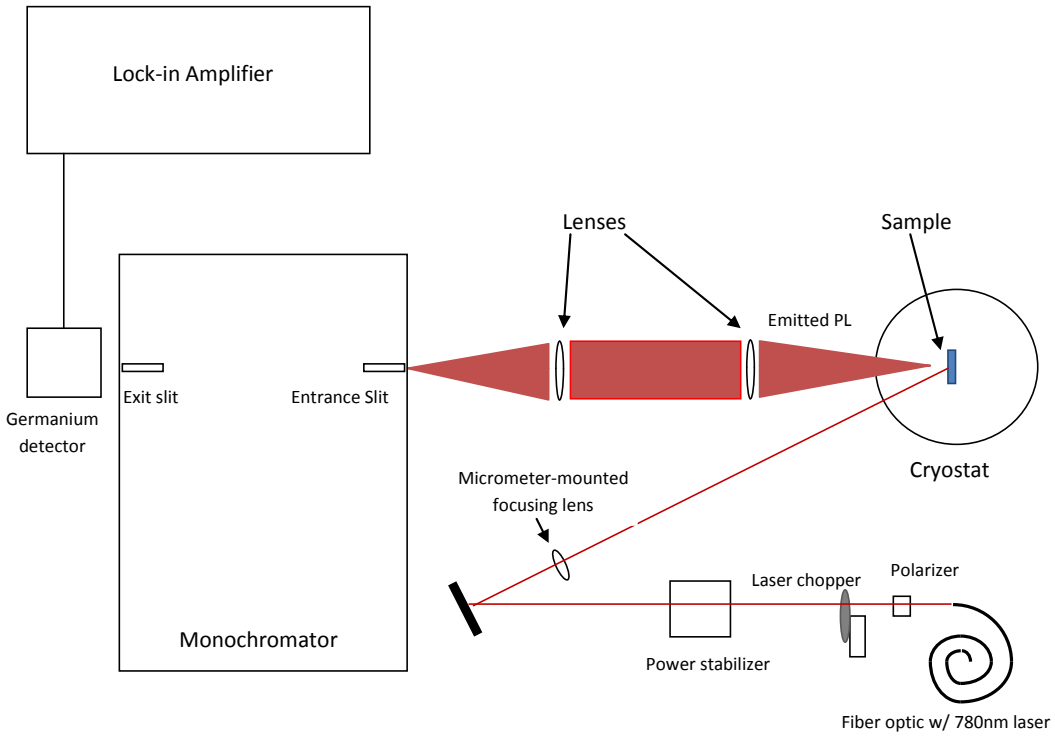

Figure 2.1 Our photoluminescence experiment setup.

sity excitation laser pumps the electrons into higher orbitals [43]. The lower energy levels fill up due to a large influx of electrons, thereby forcing the electrons into higher levels. When they relax, they relax at different energies resulting in a multi-peak PL spectrum.

Another noteworthy feature is peak width, which relates to the quality of the quantum dots [44]. With our method, we illuminate an area of the quantum dot sample, so the results show the characteristics of thousands of dots. If there is a large variation in the sizes or the chemical make up of the dots, the peak will show broadening because of the range of photon energies being emitted. In comparison, the narrower the peak, the more uniform and homogeneous the dots are.

2.1.1 Technique

The PL setup is shown in Figure 2.1. The samples were probed with an adjustable wavelength Spectra Physics 3900S Ti:Sapph laser fed through a fiber optic. A Oz Optics LPSC-04 adjustable focus single-mode fiber was used to safely pass the laser beam between optical tables. Note that although the fiber was not optimized for maintaining the light's polarization, the laser polarization remained mostly constant, but was sensitive to the positioning of the fiber.

The Ti:Sapph laser was pumped by a Spectra Physics Millenia V laser. The wavelength chosen to excite our samples was chosen to be 780 nm as seen in previous similar experiments, an energy higher than the bandgap energy of GaAs [45]. The laser was passed through a BEOC power controller for power stability within 0.1% and focused down on the sample.

Our samples were mounted to the cold-finger of a CryoIndustries 1.5W cryostat using vacuum grease. The typical temperature range for the cryostat is between 4 and 50 K, but using a secondary resistive heater we've extended that range up to 300 K.

The PL was then collected using a lens that matched the cryostat's f-number. A lens' f-number is given by

$$\text{f-number} = f/D, \tag{2.1}$$

where f is the focal length and D is the effective aperture diameter. By matching f-numbers, we maximize the amount of light collected. Once collimated by the collecting lens, the PL is then passed through a second lens with a f-number corresponding to the monochromator entrance slit. By matching the spectrometer's f-number, this illuminates the entire grating area and maximizes the spectral resolution within the monochromator.

The monochromator then scanned through a range of wavelengths which was fed to a Thorlabs PDF10C InGaAs detector. The detector output was connected to a Stanford Research Systems SR810/SR830 lock-in amplifier referenced to a chopper placed in the path of the excitation laser.

The chopper frequency was chosen to be approximately 20 Hz so not to coincide with 60 Hz light sources and due to the limitations of the detector. A computer recorded the voltage (PL intensity) from the lock-in amplifier as a function of wavelength.

2.2 Transmission Electron Microscopy

Using the Rayleigh criterion,

$$\sin\theta_R = 1.22\frac{\lambda}{d} \tag{2.2}$$

where θ_R is the angular resolution, λ is the wavelength of light (or particle) being used to image, and d is the diameter of the lens' aperture, it becomes obvious that there is a physical limit to what one can image with a microscope using visible light. For example, the range of $\sin\theta_R$ is 0 to 1. With the wavelength range $\approx 400-700$ nm, the resolution is restricted to the lower bound of about 500 to 900 nm. In order to image at a smaller scale, electron microscopes were developed. These use high-energy electrons and the dual wave-particle nature of matter to potentially image with subatomic scales. Although microscopists are not yet at that limit, they are able to see columns of atoms in high resolution electron microscope images [46–48].

The transmission electron microscope, or TEM, works by passing electrons through the sample of interest. Electrons from a high-energy electron source are accelerated to an energy range of 0 eV to a few hundred keV. The electrons then are collimated through a condensing electromagnetic lens. The beam of electrons passes through another condensing lens and aperture to narrow down and straighten the electron beam. The beam passes through the sample and the electrons that are transmitted through are passed through an objective lens and aperture and projected onto either a phosphorescent screen or a CCD camera. See Fig. 2.2.

The lenses in a TEM are made from electromagnetic coils which focus the beam of electrons.

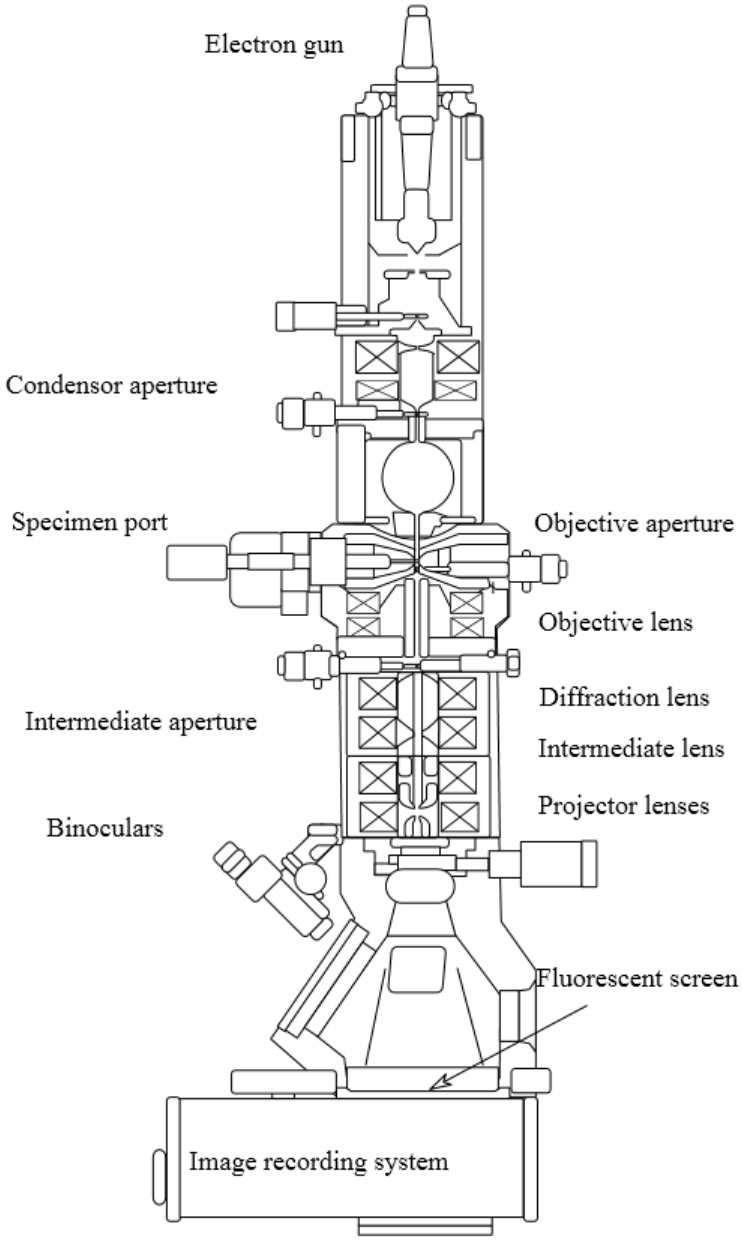

Figure 2.2 A schematic of a typical transmission electron microscope (TEM).[ii]

They create two directional magnetic fields: a radial field (H_r) and a vertical field (H_z) created by magnetic coils. An electron traveling partially in the z direction (downward), therefore, will be sent spiraling in a helical path due to the H_r field. It then interacts with the H_z field since part of its motion is now in the $\hat{\phi}$ direction, pulling the electron in closer to the center. By controlling the currents in these coils, one is able to focus the beam of electrons.

The electrons incident on the sample react a number of ways, as seen in Figure 2.3. As electrons are ionizing radiation, some of the interactions electrons may have with the sample are characteristic x-rays, Bremsstrahlung x-rays, backscattered or secondary electrons, and Auger electrons. Electrons that pass straight through the sample result in the direct beam. Electrons that pass through but are deflected by elastic or inelastic scattering result in the diffracted beam. In a scanning electron microscope (SEM), the backscattered electrons are collected for the image.

Imaging Methods

We have used a number of imaging techniques to image these dots; however, not all of them have proven useful. One method, called *mass-thickness contrast*, arises from incoherent eleastic scatter of electrons, similar to Rutherford scattering [49]. The higher the atomic number Z (or the mass and density) in a region of a sample, the more electrons will be scattered from the region, producing a dark spot in the image [47]. Since our samples contain a low amount of indium, this has given insufficient contrast for our purpose.

We used *diffraction contrast* as our primary imaging technique. To obtain good diffraction contrast, based on Bragg diffraction principles, the sample is tilted into a two-beam condition, in which only one diffracted beam is strong (see Figure 2.4). This will produce an image with strong contrast in the strains oriented with respect to the diffraction spot chosen for the two-beam condition in both bright field and dark field images [47].

Scanning transmission electron microscopy, or STEM mode is generally used for performing

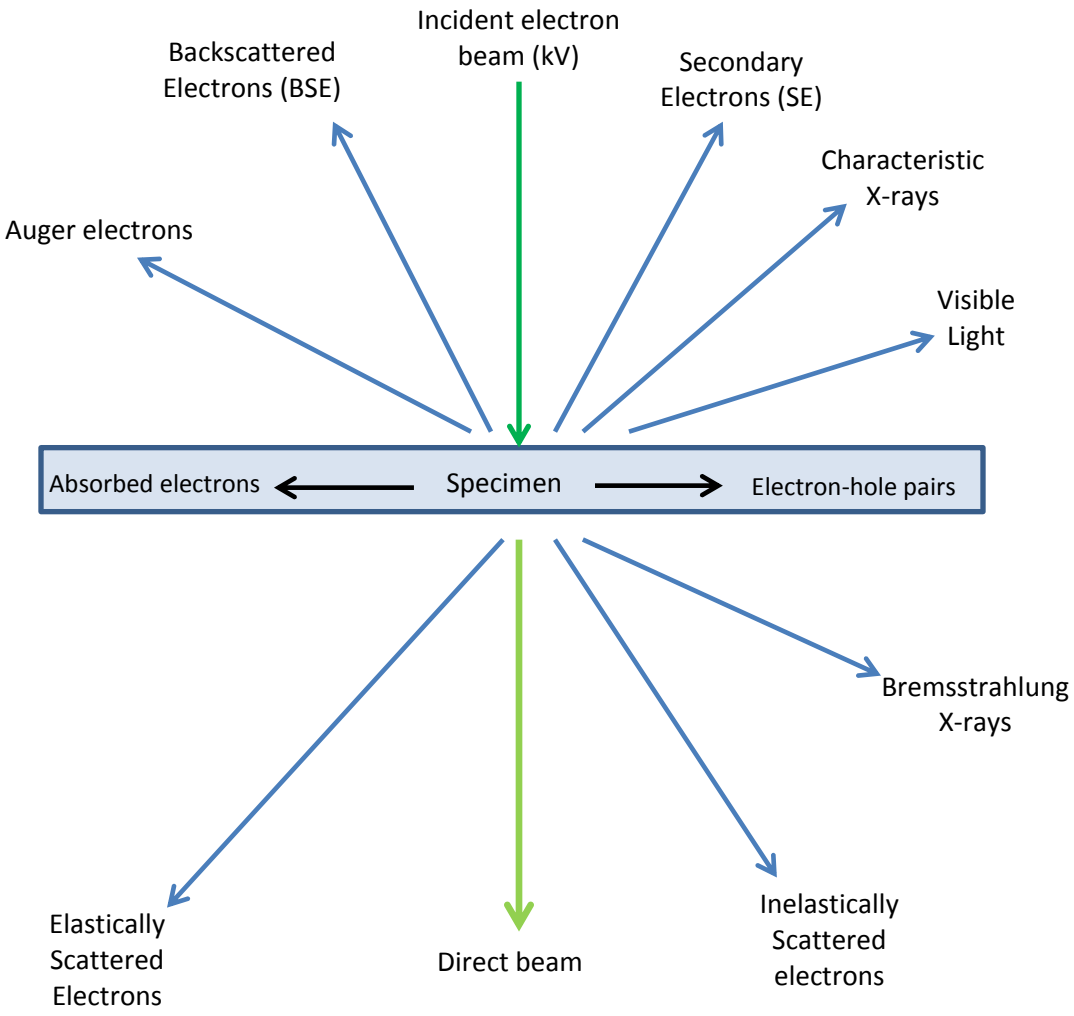

Figure 2.3 Electron beam interactions with the sample, as referenced in [47]

analytical transmission electron microscopy [47]. This is simply a focused electron beam which is scanned over the sample in a raster to get the image. Under the right conditions, it is able to resolve atomic scale resolution images. However, STEM images generally are noiser than TEM images. This is due to the beam rastering across the surface, and the fact that the beam size dominates the resolution. Both mass-thickness and diffraction contrast methods can be set up in STEM mode [47].

Of these methods, there is a subset of imaging modes. Bright field images are produced by

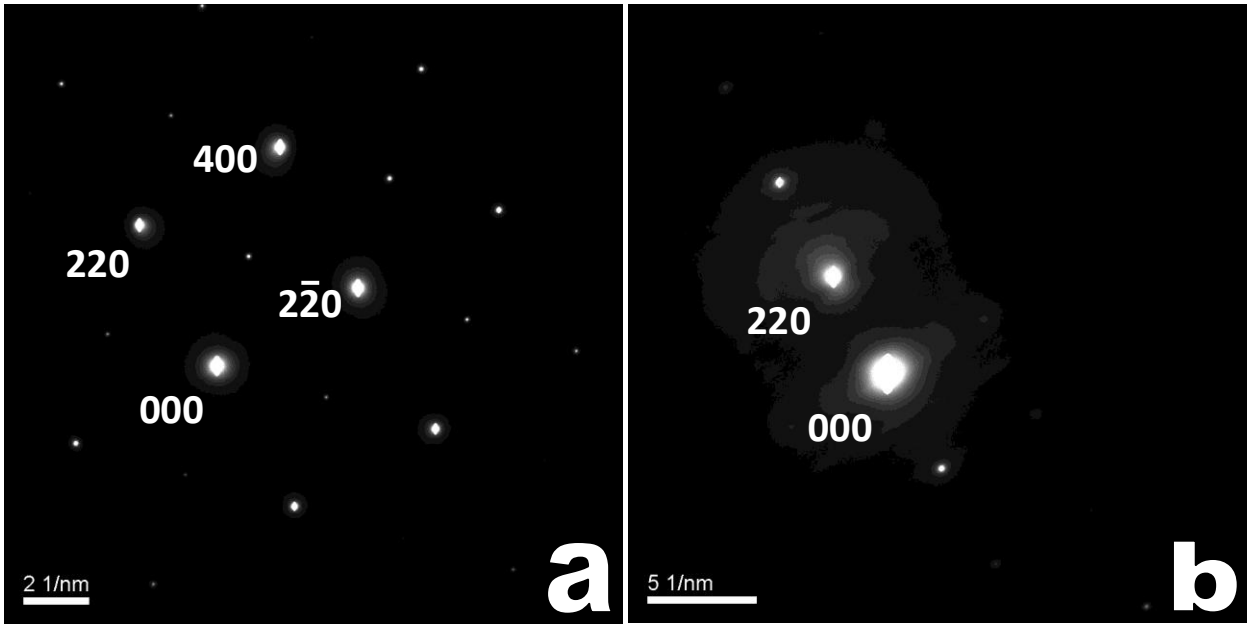

Figure 2.4 (a) Diffraction pattern in the (001) direction of a GaAs crystal. (b) As the sample is tilted into the (220) two-beam condition, the (220) spot becomes one of the two brightest diffraction spots.

looking at the direct beam, where dark field images are produced by looking at the scattered beam (see Fig. 2.3).

Analytical Methods

The FEI Tecnai T20 TEM used in our experiments is capable of performing analytical transmission electron microscopy (ATEM) to identify the chemical composition of the sample. Two of the methods used in ATEM are x-ray energy-dispersive spectrometry (XEDS or EDS) and electron energy-loss spectrometry (EELS). XEDS records spectra of characteristic x-rays superimposed upon a broader Bremsstrahlung spectrum. This is done by collecting the x-rays with a semiconductor detector, which generates a charge pulse proportional to the x-ray energy. This pulse is then assessed electronically and placed into a histogram of "counts" versus energy corresponding to the detected x-ray [47, 50].

EELS, on the other hand, measures the energy of the electrons lost while passing through the specimen. The inelastic interaction in a crystalline sample is mainly an electron-electron interaction, entailing loss of energy and change of momentum [48]. Note that PEELS is also used, meaning *parallel* electron energy-loss spectrometry. PEELS is a modern development where the detector makes parallel measurements, improving near-edge structure in EELS spectra [51].

EELS is more difficult to use than XEDS; however, it has advantages in measuring atomic composition and chemical bonding. It allows for the detection of elements at higher spatial resoution, phase identification, and bonding information. The resolution is better than XEDS, so that more structural information can be obtained from the fine structure in EELS [50].

XEDS has advantages in identifying the atomic composition in a material. The elemental composition within a probed area can be determined to a high degree of precision; however, it lacks somewhat in quantifying those elements [50].

XEDS has proven to be more useful than PEELS when analyzing our samples because of the difficulty of observing the indium peak in the PEELS spectra. This is later explained, along with XEDS results, in chapter 4.

2.2.1 Sample Preparation

In order to image the samples using the TEM, the sample must be cut thin enough to pass a beam of electrons through it. For GaAs, this thickness must be less than 100 nm. The other spatial dimensions are microns in size.

We used a Tecnai FEI Helios dual-beam (focused ion) scanning electron microscope (FIB/SEM) to prepare our samples. The FIB/SEM uses a Ga^+ focused ion beam (FIB) for milling. Both an electron beam and an ion beam may be used to image the sample in the FIB/SEM; however, by controlling the acceleration voltage and current of the ion beam, we are able to mill away the material in a small-scale region. We refer to the isolated piece left over from milling as a *cut*. Two

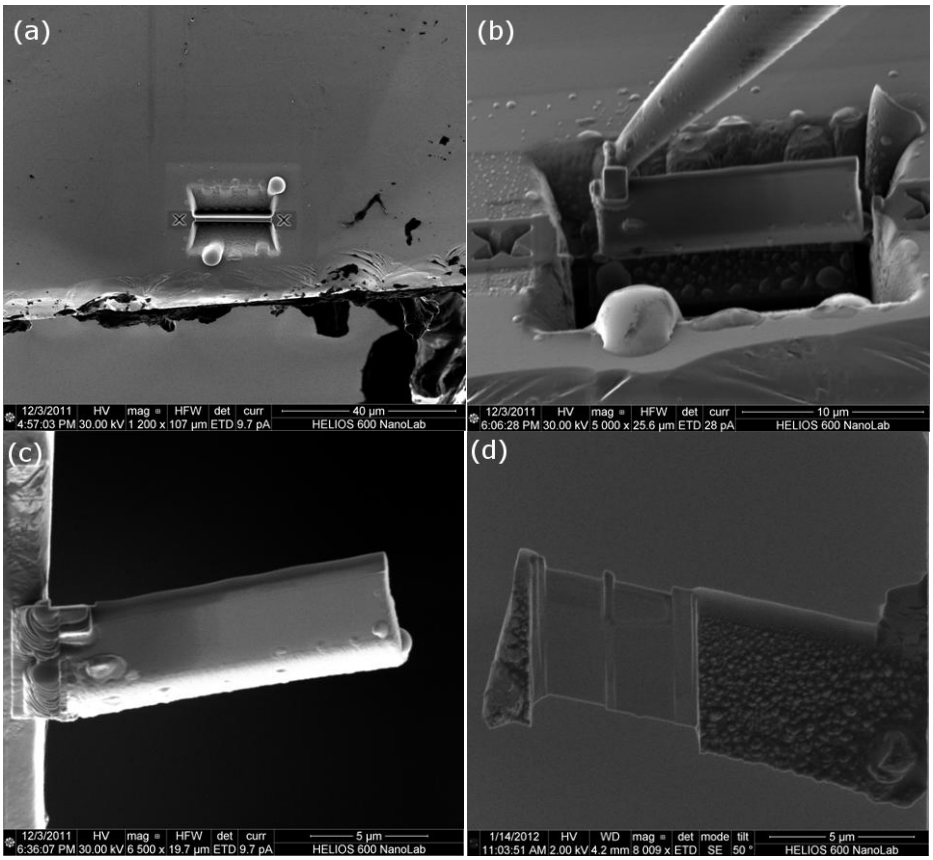

Figure 2.5 Four images that show the cross-section preparation process. (a) This shows a top-down view of the sample. A platinum layer is placed down, and two wedge-shaped pits are milled out. (b) Sample is cut around the edges, attached to a needle, and lifted out. (c) The sample is attached to the copper TEM grid and (d) regions are thinned to approximately 100 nm thick.

types of cuts were taken from each sample: a cross-section cut and a plan view cut.

Once the cut has been removed from the sample, it is then mounted on a copper lift-out grid, a mount for small specimens, for the TEM. A platinum gas insertion needle is used for mounting the sample to the grid with platinum.

Cross-section Cuts

Cross-section cuts are well-known and widely-used in the SEM/TEM community [52]. The first steps involve selecting the area you wish to cut your sample, depositing a thin protective layer of platinum via a platinum gas insertion needle, and identifying the initial width and thickness dimensions. The computer script will then mill out both sides of the rectangular bar previously designated to be your cut sample, as seen in Figure 2.5(a). These pits are milled in a staircase fashion with the deep end closest to the rectangular bar. Once both sides are milled, the narrow ends of the bar are then cut with one end left partially attached. An Omniprobe needle is then inserted into the sample area, piloted to the location of the sample, and the needle is attached to the free end of the sample using platinum deposition. The opposite end is cut from the sample (Figure 2.5(b)), and the Omniprobe needle is then piloted away, relocated to the copper grid, and the sample is attached to one of the prongs of the copper grid (Figure 2.5(c)). Once attached, the sample is thinned to less than 100 nm (Figure 2.5(d)) with additional FIB milling. The entire process takes two to six hours for us to complete for each cross-section cut.

Plan View Cuts

Many of the prior TEM plan view images of quantum dots have been obtained with help of multiple stacks of dots or having a high amount of indium inside the dot [53]. Our dots, however, are a single stack and contain low amounts of indium, which makes these dots difficult to image with the mass-thickness method. In addition, plan view cuts are difficult to obtain for GaAs because of its brittleness and the 100 nm thickness requirement for imaging in the TEM. To address this issue, we've developed techniques for obtaining plan view cuts, as described in the next few paragraphs, and have imaged the strain fields of the dots with two-beam diffraction contrast [54].

There are a number of potential methods for acquiring a plan view cut. Three options include: (a) milling it out from the sample with the FIB, (b) mechanically thinning it using diamond grit

polishing pads, or (c) a combination of the two. We have used all three options and have found the final option to be the best.

To prepare a plan view cut using the FIB is very similar to preparing a cross-section cut. Since the quantum dot layer is nearly 100 nm from the surface of the sample, we start the milling process for the trench approximately 1 micron from the surface at an angle between 5° - 10° relative to the surface plain (see Figure 2.6). This makes our cut wedge shaped so that there are varying thicknesses along the length of the cut. The rest of the process is similar to the cross-section lift-out method; however, special precautions must be made so that we do not deposit any platinum on the top surface (001) of the sample.

Once it has been mounted on the copper grid, the cut is thinned. The top GaAs layers must be milled off at a slight angle so that not all of the QD layer is milled. The bottom layer is thinned so that there are both thick (about 100 nm) and thin (about 50 nm) regions.

This entire process takes slightly longer than a cross-section cut.

We've encountered many problems using this method. Some cuts were lost by vibrations introduced by inserting the platinum gas insertion needle, shaking the sample off the Omniprobe needle when preparing to mount the sample to the copper grid. Another was lost when inserting the Omniprobe after the platinum insertion needle, unintentionally over-extending the Omniprobe and running it into the platinum insertion needle, thus bending the Omniprobe needle and losing the sample. Other times, we had unexplained platinum deposition on the viewing surface, rendering the TEM unable to make observations of InGaAs quantum dots.

Hand polishing the samples alone also proved to be unsatisfactory. Before the sample was thin enough for TEM imaging, the sample tended to break along cleavage planes. Instead, a hybrid method of mechanical thinning (hand polishing) and FIB was used.

The hybrid thinning method was used for two of our samples (specifically 032607A and 032907) [55]. The sample was polished at about a 1° angle from the (100) surface. Special

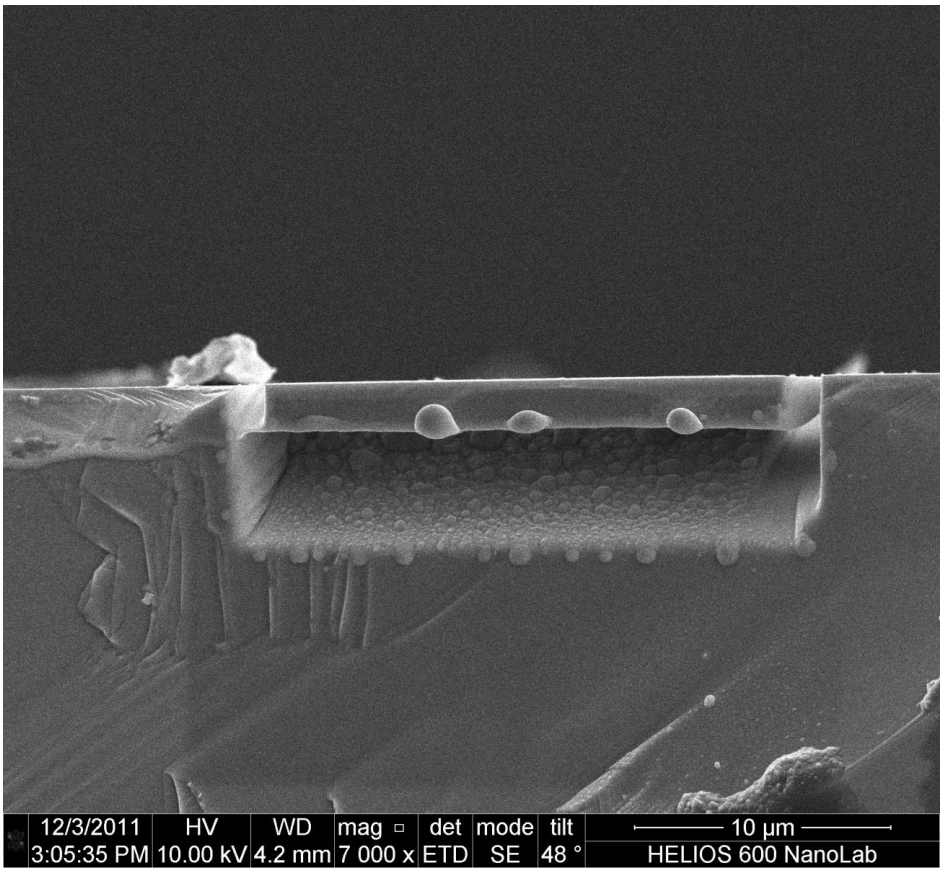

Figure 2.6 Plan view cut prepared with the FIB. Damage from the FIB (still apparent on the milled surfaces) will be milled away with a lower-current beam in later steps.

consideration was given to not polish along a GaAs cleave plain, knowing that GaAs can fracture easily. The sample was first washed thoroughly and mounted on a polishing tripod. Initial thinning began with 30 micron diamond grit sheets until a polished edge began to show. We used smaller grit (0.1 - 10 micron) sheets to slowly polish the layers away until the large scratches disappear and the polished edge becomes more defined. Suspended diamond grits (suspended in oil or water) and diluted grit compound were also used. In the end, we found that using 3 micron compound was the best option for thinning the sample, minimizing the possibility of large pieces breaking off and minimizing time spent polishing.

Once the sample was a few microns in thickness on the narrow end of the wedge, it was fastened

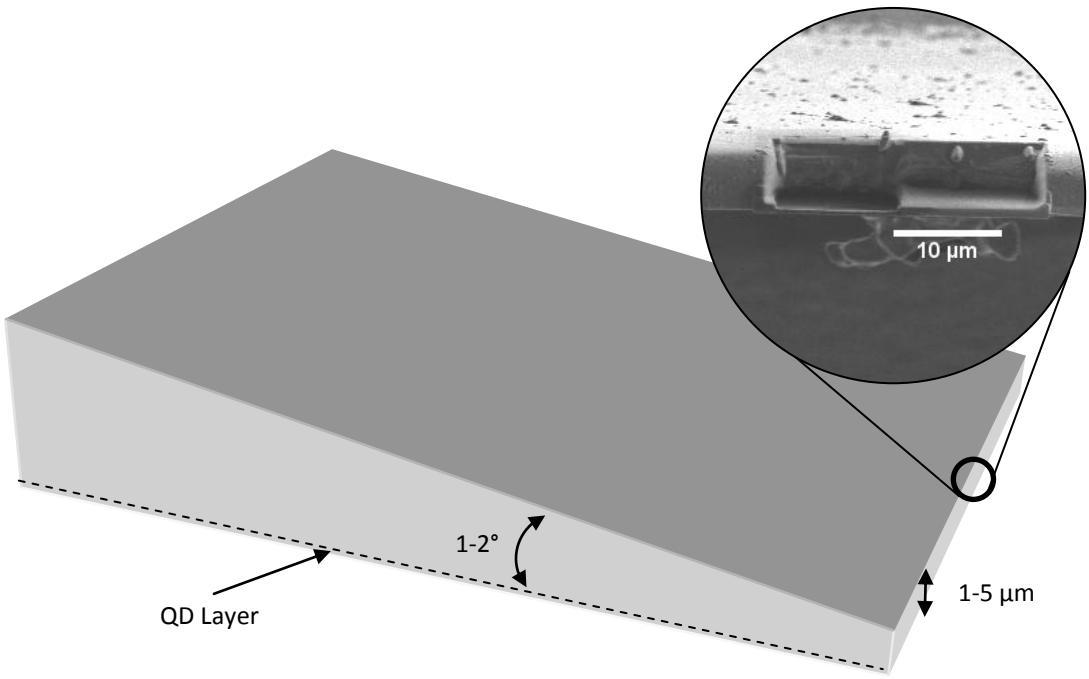

Figure 2.7 Diagram of the wedge prepared for plan view images. The sample is polished into a wedge at a small angle relative to the surface. The sample is transferred when it is a few microns thick to the FIB/SEM to be thinned further.

to a half washer mount. The sample was then transferred to the FIB/SEM and thinned the rest of the way using the FIB. The wedge is diagrammed in Figure 2.7.

The overall process usually takes a few hours.

This method, polishing the samples by hand, has its own set of drawbacks. First of all, hand polishing in wedges is a very slow process for GaAs-based materials. Since GaAs is brittle, we found it to fracture easily with all sizes of diamond grit sheets. In this method, we must use the entire sample (~1-2 millimeters on the side) and it cannot be reused like one can when preparing cuts in the FIB. However, in comparison to the lift-out method as described above, we had a higher success rate preparing the samples using this hybrid method.

Chapter 3

Photoluminescence Results

Recently, our collaborator Haeyeon Yang has submitted a paper for review summarizing our photoluminescence results [56]. My involvement in this experiment included taking some of the photoluminescence measurements, alignments, and partial summaries of each day's results. As explained in earlier chapters, the samples studied are a single stack of self-assembled quantum dot chains. The photoluminescence study suggests that there is a critical annealing temperature for the modified Stranski-Krastanov method used to grow the dots. The following section contains a summary of the paper.

3.1 Optical Properites of QDs Induced by Annealing

3.1.1 Summary

The quantum dots under study are a single stack of QD-chains that form from the strained but flat epilayers during the annealing process. The photoluminescence (PL) spectra from the QDs show strong, narrow linewidths of ~23 meV for annealing temperatures lower than 500°C. The annealing temperature has a critical impact on the optical properties. Increasing the annealing temperature to

500°C induced further flattening of the dots than lower temperatures, which was seen in scanning tunneling microscope (STM) images of the uncapped samples [57]. The flattening of the dots is accompanied by emission linewidth broadening and disappearance of room-temperature PL peak signal.

3.1.2 Sample Growth

Commercially availible n-type GaAs(001) substrate wafers were loaded into the growth chamber of the molecular beam epitaxy (MBE) machine through a preparation chamber [58]. After a GaAs buffer layer over 500 nm thick was grown, the substrate was cooled down to 360°C. A deposition of InGaAs ~10 monolayers (ML) thick resulted in strained but flat surfaces as seen in previous works [57, 58]. It is estimated that the nominal indium concentration to be around 37% [57]. The substrate temperature was ramped at 20°C / min to a temperature 460°C or higher, at which the InGaAs epilayers were annealed for 120 seconds in the growth chamber. It was observed that annealing at temperatures lower than 460°C, QDs without chaining could be obtained and was observed by in-vacuum STM imaging [57]. During the ramp-up and annealing period, the diffraction pattern was monitored in real time for the transition from 2D to 3D by reflection high-energy election diffraction (RHEED) [31,59]. Details on how the low-temperature growth followed by high-temperature annealing produces chains of dots can be found in references [20, 57, 58]. The samples were then transferred into the attached ultra-high vacuum (UHV) STM, Omicron 1, through a UHV port in order to obtain QD morphologies that are contamination free [58]. Separate samples were grown with an additional 100 nm GaAs capplinglayer for PL measurements and transmission electron microscope images (TEM). The first 10 nm of the cap was deposited on top of the InGaAs layer immediately after annealing. The remaining 90 nm was deposited at a temperature of 580°C, just before the sample was taken out of the MBE machine.

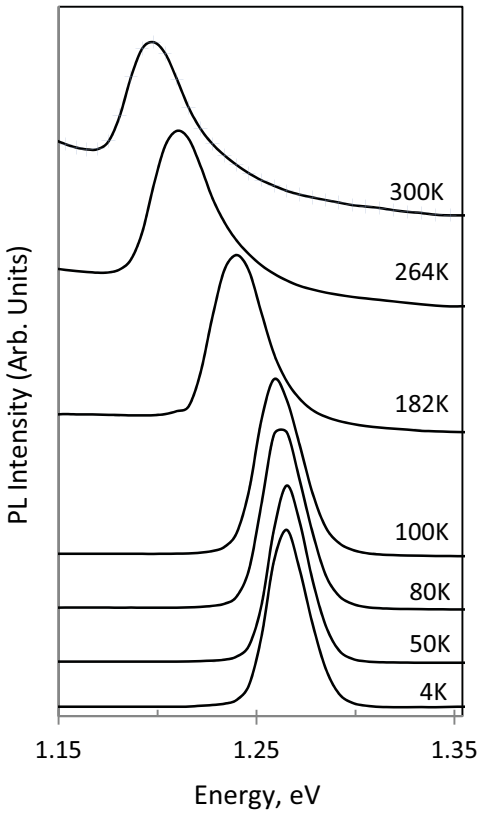

Fig. 3. Normalized PL spectra from sample at various temperature with the excitation intensity of 1pcW/cm². The cross-sectional TEM view of this sample is shown in Fig. 1 along with the STM image of dot-chains.

Figure 3.1 Normalized PL spectra from a 460°C sample at various temperature with the excitation intensity of 160 W/cm^2. From Ref. [56]

3.1.3 Method

PL measurements were made using a cw Ti-Sapphire laser at 780 nm, which was focused onto samples in a cryostat, with a spot diameter of 200 μm and typical power of 50 mW. The emitted light from the samples was collimated and focused into an iHR320 Horiba 0.32 m spectrometer (grating blazed at 1000 nm, 600 lines/mm) for wavelength selectivity. Light emerging from the spectrometer was focused onto and detected with a Thorlabs PDF10C InGaAs detector. The laser beam was chopped at 20 Hz and the data was collected with a standard lock-in technique.

3.1.4 Measurements and Discussion

Fig. 3.1 shows changes in PL spectra with temperature for the sample annealed at 460°C. The peak position shifts to lower energies as the temperature increases [60]. The excitation intensity was 160 W / cm^2, and each spectrum has been normalized by its maximum and shifted vertically for clarity. Unlike PL emissions from stacked QD-chains, no changes in peak position (wavelength) were observed as the excitation intensities were varied from 16 W / cm^2 to 1.6 kW / cm^2 [61]. The state-filling effect, where electrons are pumped into higher orbitals, was not observed over the excitation intensities used [62, 63].

The peak energies are larger than InGaAs QDs grown by the conventional Stranski-Krastanov (SK) method as reported by the Raymond group [63]. This may be attributed to a larger indium composition, resulting in a smaller band gap.

The room temperature luminescence from our samples annealed at 460°C and 480°C are present, although the intensities are much weaker than at low temperatures. However, for the sample annealed at 500°C, the room temperature PL emission intensity goes below the detection limit. According to a recent study of PL emission from QDs in a pulsed magnetic field, the laterally smaller dots dominated the PL emission at high temperatures [64]. The disappearance of room temperature PL could be due to the combined effect of flattening and broadening of the dots at higher annealing temperatures.

Similar shifts in peak position with temperature, as seen in Fig. 3.2, were also observed from the samples annealed at higher temperatures. The figure shows that the peak energy stays the same up to 60K for the sample annealed at 460°C and up to 40K for the samples annealed at 480°C and 500°C. The peak energies for the three samples are higher than those as reported from conventionally grown InGaAs QDs with similar (expected) composition of 40% and similar deposition amount of 10 ML [62].

For comparison, using the Varshni relationship [65] and the bandgap equation for InGaAs alloy

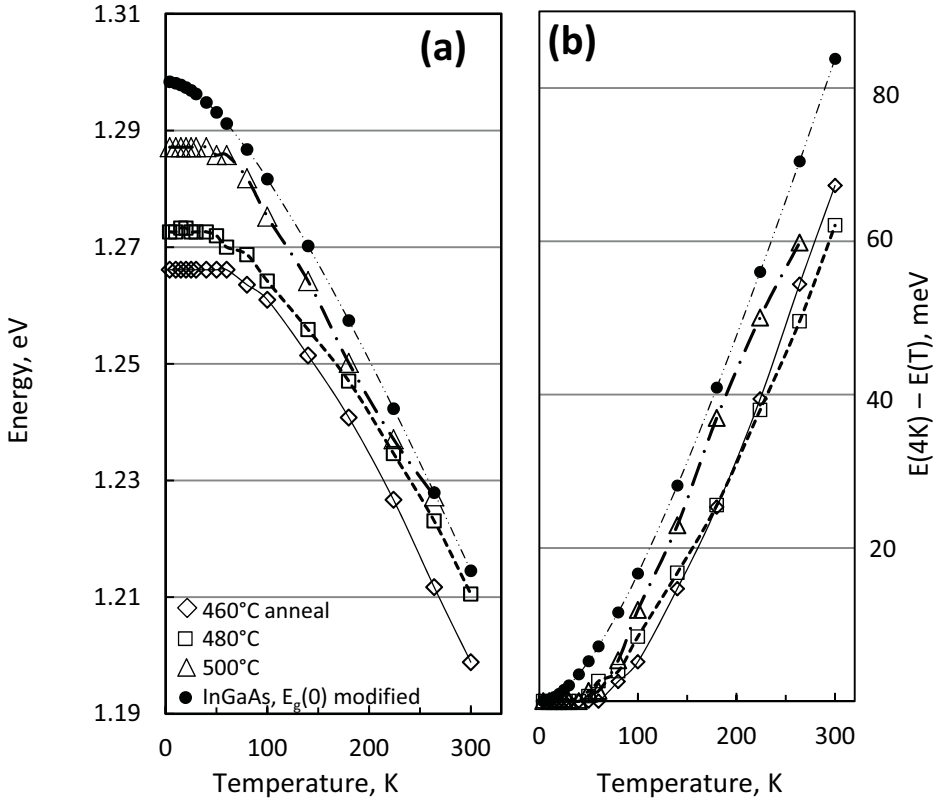

Fig. 4. The change of peak position over temperature is shown in (a) while the relative difference of the peak energy from that of 4K is shown in (b). In (a), the bandgap change of bulk InGaAs over temperature is added with modified $E_g(0)$ value for comparison

Figure 3.2 The change of peak position over temperature is shown in (a) while the relative difference of the peak energy from that of 4K is shown in (b). In (a), the bandgap change of bulk InGaAs over temperature is added with modified $E_g(0)$ value for comparison From Ref. [56]..

with 40% indium [66], bandgap change with temperature is also shown in the figure (as indicated by the filled, black circles) for unstrained InGaAs (40% indium) with modified value at zero kelvin. The QD-chains formed at 460 and 480°C annealing more or less follow the Varshni curve of the InGaAs alloy, while those formed at 500°C show faster red shifts over temperature than those from typical QDs [67]. This suggests that the QD-chains have different thermal escape behavior for excited carriers due to the difference in electronic states. The disappearance of the PL peak at room temperature over the all excitation intensities employed (as seen in the 500°C-annealed sample) is another characteristic of QDs formed with the conventional SK growth method. Thus we see that the 500°C sample has electronic structures more similar to dots grown by the SK

method than to the other QD chain samples.

The low temperature peak positions are higher energy than those of a similar sample as reported by Kamath, which is unexpected [62]. The growth of the conventional QDs in Kamath's sample was done at high temperature, in the range between 500°C and 550°C. Because indium desorbs faster than gallium at high temperature [68], one would expect high temperature growth to yield dots with a lower indium percentage, and a correspondingly higher peak energy. Our dot-chains, by contrast, were grown via strained-but-flat layers produced at a much lower temperature of 360°C, and even our annealing temperatures of 460, 480, and 500°C were lower than the growth temperature of those conventional dots. Thus our dot-chains very likely have a lower fraction of indium than those of Ref. [62]. Therefore, the unexpectedly high peak energies in our samples must be a result of morphology, rather than composition. We attribute this to a flattening of the dots in our dot-chains, which must increase peak energies via an increased quantum confinement vertically despite a larger lateral size.

The PL peak positions of our three quantum dot-chain samples increase in energy with the annealing temperature. This follows the expected trend mentioned above of higher peak energies with higher growth temperatures. Because the total annealing period of the sample annealed at 500°C is only three minutes longer than that of the sample annealed at 480°C, it seems unlikely for significant indium desorption to have occurred. Therefore we again attribute the blue-shift in peak energy with annealing temperature to a flattening of the dots in the dot-chains.

In addition to the peak positions of our samples being higher in energy than those of the conventional dots as mentioned above, it is also interesting to note that the peak position of our 500°C-annealed sample is higher in energy than the 1.274 eV peak seen from a 15 ML thick (about 4 nm) InGaAs quantum well with 30% indium concentration at comparable temperature (20 K) [69]. Again this is surprising at first glance because the smaller indium concentration and smaller nominal thickness of the quantum well relative to our dot layer would be expected to result in a higher

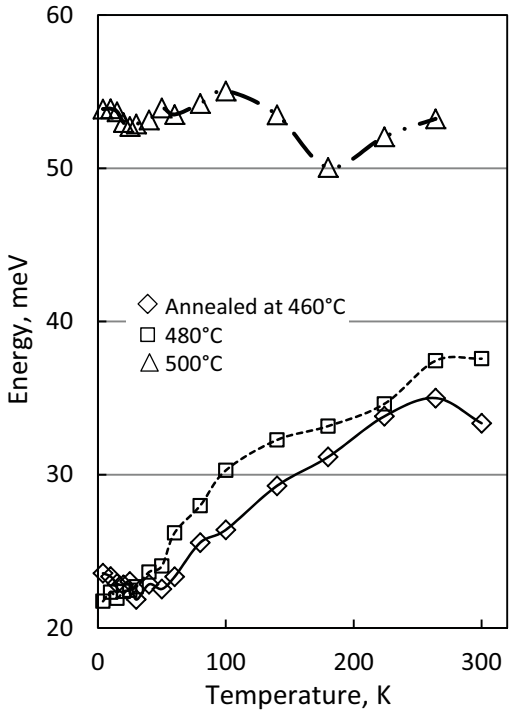

Figure 3.3 Full width at half maxima (FWHM) of the emission peak are shown. There is a big increase in FWHM for the sample annealed at 500°C compared with those from samples annealed at lower temperatures; slight increase in FWHM over temperature is noted for the sample annealed at 480°C compared those from the sample annealed at 460°C. From Ref. [56].

Fig. 5. Full widths at half maxima (FWHM) of the emission peaks are shown. There is a substantial increase in FWHM for the sample annealed at 500°C compared with those from samples annealed at lower temperatures.

energy. In this case, it's likely that lateral confinement in our dot-chains is responsible for the increased peak energy of our sample relative to that quantum well.

The high quality of our dot-chains is evidenced by relatively narrow PL peaks. As can be seen from Fig. 3.3, the major peak of the 460°C and 480°C-annealed samples has a full width at half maximum (FWHM) of 23 meV at 20K, which is much narrower than those from InGaAs QDs grown by MBE with similar nominal composition of 40% indium and thickness of ~10 ML, QDs by atomic layer epitaxy (ALE) with 50% indium composition [70], and dot-chains [61] in superlattice. The narrower linewidth suggests that QDs grown by the annealing technique result in a highly homogeneous distribution in size as the narrow linewidth has been attributed [44, 62] to

narrow size distribution of QDs grown both MBE [62, 71] and ALE [70]. However, much larger linewidths (50 - 55 meV) are observed from QD-chains when the annealing temperature increases to 500ºC. This suggests that the QD size distribution broadens critically at that temperature. The PL linewidth stays roughly constant with temperature for the 500°C annealed sample while the linewidth increases with temperature for the samples annealed at lower temperatures.

The PL data indicate that the two samples annealed at 460°C to 480°C have similar electronic structure, evidenced by the similar emission spectra and linewidths over the temperature range. The similarity is surprising because the STM images from the uncapped sample surfaces indicate that the annealing temperature has a significant impact on the shape and size of dot-chains [57]. The dot-chains become larger laterally but shorter as they get flattened when the annealing temperature is increased by 20°C to 480°C. By contrast, the additional 20°C increase in annealing temperature from 480°C to 500°C (with its additional flattening and lateral size increase) clearly resulted in a large change in electronic structure.

3.1.5 Conclusion

In summary, we have studied the correlation between the optical and structural properties from QD-chains that are produced by annealing strained-but-flat epilayers. Strong PL emissions with rather narrow linewidths are observed from the samples examined. It is found that there is a critical annealing temperature between 480°C and 500°C, above which the optical properties resemble QDs produced by the typical S-K growth technique, which is significant in the growth of material for optoelectronic devices. This novel growth approach, annealing strained-but-flat epilayers, may be useful for high quality optoelectronic devices operating at room temperature.

Details about the morphological properties observed are found in the succeeding chapter.

Chapter 4

TEM Results

4.1 Cross-Section Results

4.1.1 Identifying the QD Layer

In the images below, several layers appear. Although we only have a few deposited layers (GaAs substrate, InGaAs layer which includes the dots, GaAs capping layer, optional carbon layer, and a protective platinum layer), it is supposed that any additional layers are interfaces (e.g. GaAs mixing with platinum, or the platinum peeling from the GaAs surface) and are neglected for this study. The InGaAs layer however is easily identifiable: it sits approximately 100 nm from the surface, has a darker tone in bright field conditions than GaAs, and in some cases will exhibit darker regions around it indicating a lattice strain between the GaAs and InGaAs lattices.

By viewing the sample in different two-beam conditions, it is possible to see contrast from the strain fields. The condition used in the images below are a (220) condition. This is the condition that produced the best strain contrast to see the individual quantum dots in the images. Figure 4.1 shows three side by side images of strains surrounding quantum dots in the (220) condition.

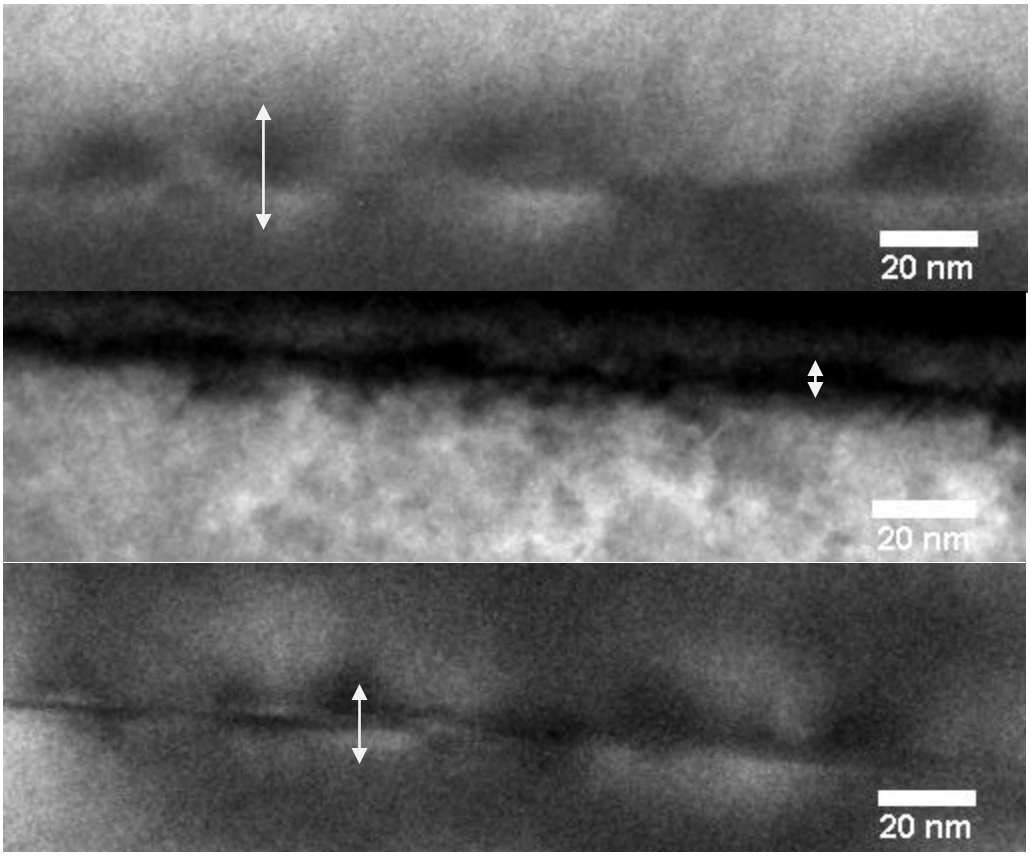

Figure 4.1 The wetting layer line (the dark line between dots) is along the [110] direction. In order to illustrate the morphological evolution between the two annealing temperatures, a side-by-side comparison of the samples is shown. (a) Dark field image of the sample annealed at 460°C (032607A), (b) a dark field image of the sample annealed at 480°C (032907) and (c) a bright field image of the sample annealed at 500°C (032607B). These images show diffraction contrast under the (220) two-beam condition. The arrows show the the edges of the strain fields used in measurements listed in Table 4.2.

4.1.2 Chemical Analysis

We've tried both PEELS and XEDS on our samples, but we have only seen useful results with XEDS. Figure 4.2 shows the PEELS result we obtained for the sample annealed at 500°C; however, with the large GaAs peak and noise, the indium peak is dwarfed using this method. Figure 4.2 shows where the primary peaks are expected.

Figure 4.2 PEELS results for the sample annealed at 500°C (032607B). The indium peak is difficult to distinguish in this spectrum, making EDS the analytical method of choice.

Alternatively, we've turned to XEDS to chemically analyze the quantum dot chains. The XEDS spectrum shown in Figure 4.3 shows the different elements that are observed interacting with x-rays.

4.2 Plan View Results

Plan view cuts of all three samples have been imaged. It is evident that dot-chains exist in all three samples and compare well with the STM images from Ref. [20]. The thickness of the cut-and-thinned sample dictates the imaging quality; the thinner the sample is, the more warping of the sample there is. Macroscopic strains due to warping are seen in Figure 4.4a, which is one of the images from the sample annealed at 500°C.

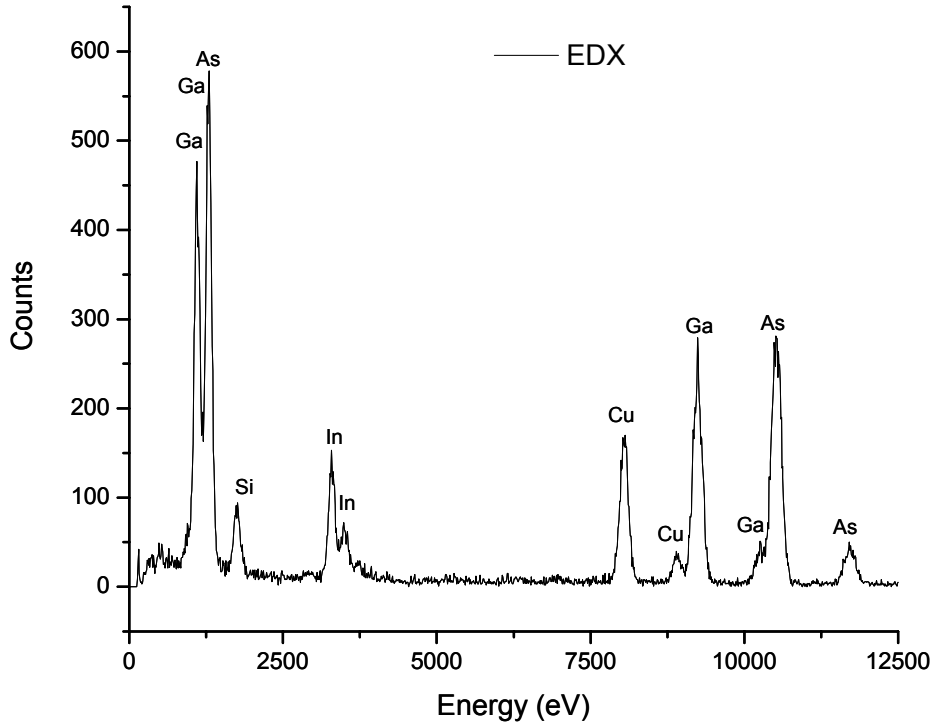

Figure 4.3 The XEDS spectrum showing the energies of x-rays collected, which are related to various elements as labeled. Note that the peak heights do not necessarily correspond to the quantity of these elements.

It should also be noted that one of the (220) two-beam conditions was the best imaging condition for the dots, as was seen with the cross-section.

Figure 4.5 show side-by-side comparisons of each sample's plan view images with different lookup tables than grayscale. Similar images were used in to measure dot widths and dot-chain densities.

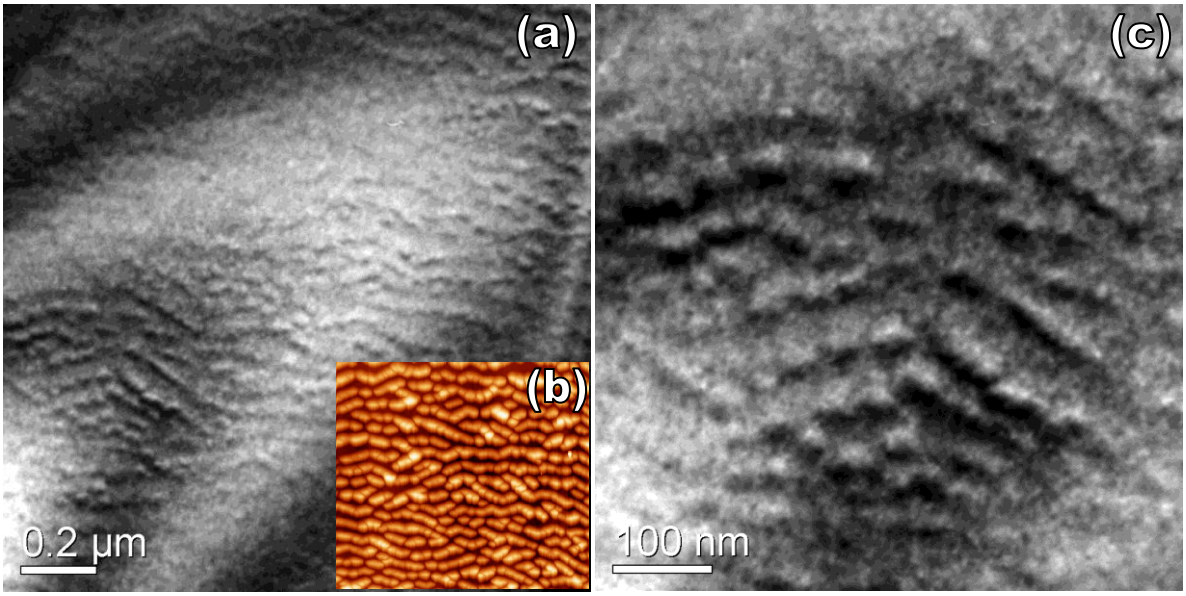

Figure 4.4 Plan view results for the sample annealed at 500°C. (a) A zoomed-out view of the dots' strain fields, in addition to macroscopic strains caused by warping of the sample. (b) This is the former STM image taken before the capping layer was deposited. The pattern of the dots is very similar to the uncapped results. Image taken from [20]. (c) A close-up of a region found in part (a). From these images, it is certain that the dots have remained in their dot-chain formation. From Ref. [56]

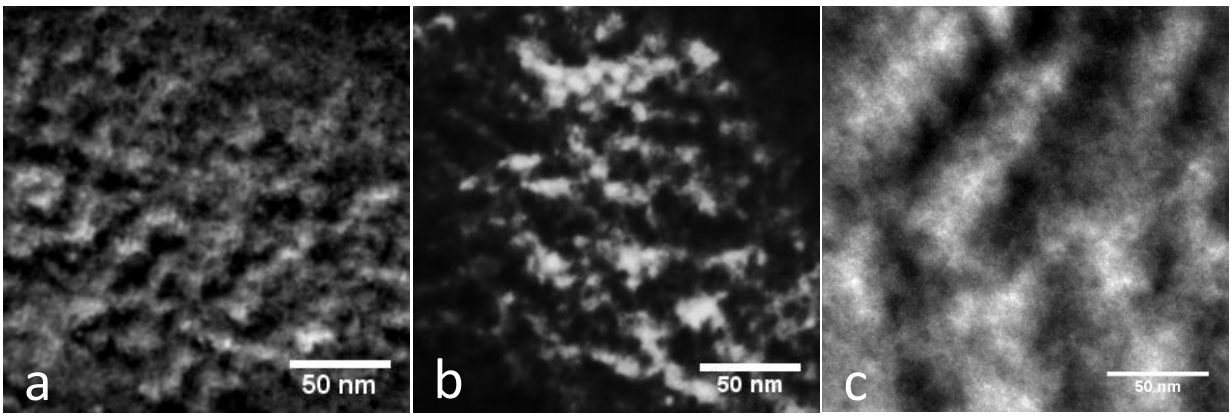

Figure 4.5 Plan view images of dot chains found in three different samples (a) 032607A (460°C), (b) 032907 (480°C), and (c) 032607B (500°C).

4.2.1 Measurements

By measuring the distance over ten chains at several locations in the images for each sample, the chains density were calculated. The average dot width was similarly obtained.

Sample	Average Dot-Chain Density ($\times 10^5$ cm^{-1})	Average Dot Width (nm)	Average Dot Separation (in chain) (nm)
032607A	2.73 ± 1.35	10.2 ± 1.9	11.0 ± 1.9
032907	3.01 ± 0.80	10.9 ± 2.4	11.1 ± 2.7
032607B	1.88 ± 0.19	16.0 ± 4.1	34.4 ± 12.9

Table 4.1 Observed dot-chain densities and dot widths in the three samples.

4.2.2 Cross-section Measurements

Physical Measurements

The height of the strain field was measured using an image processing program, Image J. Edges of the strain field were estimated to be the midpoint between light and dark regions. Measurements were made of all visible dots in the images, a few of which are shown in Figure 4.1. Table 4.2 reports the measurements. The strain fields are larger than the dots themselves, so these measurements do little more than place an upper limit on the dot height and wetting layer thickness. The strains shown in the images do show that we can point out individual dots.

Sample	Height of Strain Field (nm)	Std. Dev. (nm)
032607A (460°C)	21.65	± 4.10
032907 (480°C)	10.95	± 1.90
032607B (500°C)	13.80	± 3.55

Table 4.2 Measurements of the dot's strain fields.

Image quality depends on the thickness of the sample. The sample annealed at 480°C was comparatively thicker than the other two. Although image quality is poor, we are still able to point out locations of individual dots and measure the visible strain field.

Chemical Composition

Several measurements were made on each sample using either spot measurements, line measurements (a series of spot measurements across the QD layer) and area measurements (averaged chemical measurement across a rectangular area). Area measurements were chosen to be displayed in this thesis. The EDS results shown were chosen as the best results based on their arsenic values (closest to the expected 50%). It should be noted that the area measurements collect information from the InGaAs layer with the dots in addition to the GaAs barrier material both above and below that are included in the selected area.

Element	Weight %	Atomic %	Uncertainty %
Ga	43.04	45.85	0.44
As	50.22	49.79	0.53
In	6.73	4.35	0.18

Table 4.3 The XEDS results for the sample annealed at 460°C (032607A). This was the best result obtained from all area measurements centered on the QD layer with dimensions of approx. 50 nm × 10 nm.

Element	Weight %	Atomic %	Uncertainty %
Ga	41.93	44.98	0.34
As	49.57	49.48	0.40
In	8.49	5.53	0.15

Table 4.4 The XEDS results for the sample annealed at 480°C (032907). This was the best result obtained from all area measurements centered on the QD layer with dimensions of approx. 10 nm $\times$ 5 nm.

Element	Weight %	Atomic %	Uncertainty %
Si	2.617	6.853	0.113
Ga	36.965	38.984	0.458
As	45.371	44.527	0.582
In	15.045	9.634	0.330

Table 4.5 The XEDS results for the sample annealed at 500°C (032607B). This was a result obtained from an area measurement centered on the QD layer with dimensions of approx. 7 nm $\times$ 7 nm. Silicon was considered in this scan as a contaminant.

Element	Weight %	Atomic %	Uncertainty %
Ga	39.965	43.33	2.26
As	48.22	48.79	2.64
In	11.91	7.86	4.69

Table 4.6 The XEDS results (not accounting for silicon) for the sample annealed at 500°C (032607B). This was a result obtained from an area measurement centered on the QD layer with dimensions of approx. 7 nm $\times$ 7 nm.

These values are lower than our collaborator's claim of 40% indium. We are able to contribute this to the distribution of the dots in the sample. As seen in STM images of non-capped samples

(see Figure 4.4b), there is space between each dot-chain. We can figure out the geometry of the dot-chains and the percentage that cover the sample; we should get a closer approximation of the chemical composition of the dots.

4.3 Interpretation

These TEM images confirm QDs, QD-chains, and wetting layers after the growth of GaAs capping layers. As observed, there is significant change in the morphology of the dots in the sample annealed at 500°C. In the 460°C and 480°C annealed samples, the dots are approximately the same size and separated roughly the same distances. The dots tend to overlap more in these two samples than seen in the sample annealed at 500°C.

As mentioned above, the chemical percentages of indium listed in the tables are smaller than expected but can be corrected for using the measurements we obtained from the plan view images. To do this correctly, we have to consider the geometry of these dots (see Fig. 4.6). The dots are pyramidal, but they do overlap partially with neighboring dots [57]. We also read in Ref. [57] the height of the dots in the first sample (460°C) to be about 8.3 nm. If we assume the dimensions I measured (listed in Table 4.1), the volume per individual dot (taking into consideration the overlapping volume of neighboring dot) is about 590 nm^3. The wetting layer seen in Fig. 4.1 is about 1 nm thick. The total volume of the dots and wetting layer in a 100 nm-thick sample covered in a 50 nm x 10 nm region would be about 7,300 nm^3. This means that only about 15% of the region is the InGaAs material, and so the corrected indium percentage for the first sample would be 29%. Calculations for the other samples can be found in Table 4.7. Since the values for the height of the dots in the other two samples are unknown, estimate values are used. The height of 8 nm used in the calculations for the 480°C-annealed sample (480°C) was chosen to be close to the measured height of the sample annealed at 460°C. The height of 5 nm used in the calculations for the third

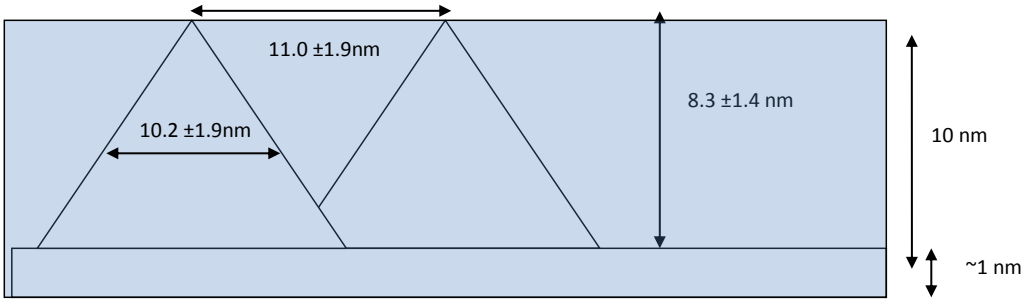

Figure 4.6 Approximate geometry for the sample annealed at 460°C (032607A).

sample was a value suggested by our collaborator [56]. (Note that for $In_{0.4}Ga_{0.6}As$, arsenic already makes up half of the sample, so the 40% indium is actually only 20% of the QD layer.)

It should also be noted that Kim et al. reported the width of the dots in their sample annealed at 460°C to be 29.6 ± 3.8 [20]. Using profile measurements, I measured the width at half-height to be 16.0 ± 4.1 nm, which would be approximately 32.0 nm at its base.

Some of the corrected values are close to the 40% we are expecting to find. Error calculations are also listed in Table. 4.7 using standard deviation error propagation [72]. The errors grow to be very large, which weakens the credibility and usefulness of the calculations.

In Chapter 3, it was shown that the emission peak from photoluminescence experiments fell in the range of 1.19 - 1.22 eV at temperatures approaching room temperature. Comparing this to the bandgap energies of GaAs (1.43 eV) and InAs (0.36 eV), we see that the spectra suggest a larger percentage of gallium than indium in the QD region. Our chemical measurements seem to be relatively consistant with the phololuminescence experiments.

It has been reported that the flattening of dots in the dot-chains occurs with temperature increase, which is confirmed by surface images of uncapped samples [57]. Measurements made on the cross-section images appear to agree. As verified by the measurements, there is significant morphological changes in the sample that was annealed at 500°C. As mentioned in Ref. [57] and in discussion with Haeyeon Yang, the RHEED cheverons were not visible for the samples annealed

at 460°C and 480°C, whereas they were clearly visible for the 500°C annealed sample.

The plan view images confirm that the dots chain along lines in a (110) or a (1$\bar{1}$0) direction.

	032607 (460°C)	Error	032907 (480°C)	Error	032607B (500°C)	Error
Width (FWHM) (nm)	10.2	1.9	10.9	2.4	16	4.1
Height (nm)	8.3	1.4	8	3	5	1
Base width (nm)	20.4	3.8	21.8	4.8	28.9	4.6
Volume of single dot (nm^3)	1151.4	627.8	1267.3	977.3	1706.7	1251.9
Separation b/t Dots (nm)	11	1.9	11.1	2.7	34	12.9
Base of overlap prism (nm)	9.4	3.3	10.7	4.3	0	0
Height of overlap prism (nm)	3.82	0.22	3.93	0.30	0	0
Volume of overlap prism (nm^3)	564.4	456.4	691.1	648.9	0	0
True Vol/dot (nm^3)	587.0	776.2	576.2	1173.1	1706.7	1251.9
Density of chains (/100 nm)	2.73	1.35	3.01	0.80	1.88	0.19
Height of area scanned (nm)	10	1	5	1	7	1
Width of area scaned (nm)	50	1	10	1	7	1
Dots per region	12.41	6.50	2.72	1.01	0.39	0.16
Vol of dots in region (nm^3)	7283.6	10360.8	1562.4	3234.4	660.6	557.6
Vol of region (nm^3)	50000	509901.9	5000	111803.4	4900	98994.9
Fraction of Dots/Region	0.15	1.50	0.31	7.02	0.13	2.73
Indium Atomic % Measured	4.35	0.18	5.53	0.15	7.86	4.69
Corrected In Amount %	29.86	307.48	17.70	397.41	58.30	1179.45
Dots per cm^2	2.48E+11	1.30E+11	2.71E+11	0.98E+11	5.53E+10	2.17E+10

Table 4.7 The XEDS results (not accounting for silicon) for the sample annealed at 500°C (032607B). This was a result obtained from an area measurement centered on the QD layer with dimensions of approx. 7 nm × 7 nm.

Chapter 5

Conclusion

With photoluminescence spectroscopy, we have been able to study the correlation between the optical and structural properties of these quantum dot chains. These dots have resulted in narrow PL peaks corresponding to high quality dots. There is a critical annealing temperature above which the quantum dots will resemble quantum dots produced by the S-K growth technique. This is significant in the growth of material for optoelectronic devices.

We have used transmission electron microscopy to answer morphological questions about our quantum dot chains. We have seen that the capping layer has not significantly altered the geometry of the dots or the wetting layer. We have verified that the dot-chains are still there, consistent with previous STM measurements. The morphology differences between the samples are consistant with what was observed in the RHEED measurements [57]. We have also observed that neither indium segregation nor intermixing has played a dominant role in the growth process.

We have obtained plan view and cross-section images for the samples annealed at three temperatures: 460°C, 480°C, and 500°C. A second paper is in progress, which is meant to supplement Yang's findings and detail the TEM work done [56].

There are many applications to quantum dot chains, and there may be some research opportunities in the future to study them with other techniques. In the meantime, we have been involved with

a number of other projects that similarily deal with nanostructure materials for us to characterize, some of which are summarized in appendices.

Bibliography

[i] Image based on diagram from Technische Universität München website.

[ii] Source: Wikimedia Commons, under GNU Free Documentation License.

[1] M. A. Reed, J. N. Randal, R. J. Aggarwal, R. J. Matyi, T. M. Moore, and A. E. Wetsel, "Observation of Discrete Electronic States in a Zero-Dimensional Semiconductor Nanostructure," Phys. Rev. Lett. **60,** 535 (1988).

[2] Z. M. Wang, Y. I. Mazur, J. L. Shultz, G. J. Salamo, T. D. Mishima, and M. B. Johnson, "One-dimensional postwetting layer in InGaAs/GaAs(100) quantum dot chains," Journal of Applied Physics 99 (2006).

[3] S. Thalman, "Photoluminescence Lifetimes of Quantum Dots,", 2011, senior thesis, Brigham Young University.

[4] A. Jones, "Photoluminescence of Indium Gallium Arsenide Quantum Dots and Dot Chains,", 2010, senior thesis, Brigham Young University.

[5] V. A. Egorov, G. E. Cirlin, N. K. Polyakov, V. N. Petrov, A. A. Tonkikh, B. V. Volovik, Y. G. Musikhin, A. E. Zhukov, A. F. Tsatsulnikov, and V. M. Ustinov, "1.3-1.4 μm Photoluminescence Emission from InAs/GaAs Quantum Dot Multilayer Structures Grown on GaAs Singular and Vicinal Substrates," Nanotech. **11,** 323–326 (2000).

[6] H. C. Liu, M. Gao, J. McCaffrey, Z. R. Wasilewski, and S. Fafard, "Quantum dot infrared photodetectors," Appl. Phys. Lett. **78,** 79–81 (2001).

[7] P. Bhattacharya, S. Ghosh, and A. Stiff-Roberts, "Quantum Dot Opto-Electronic Devices," Annu. Rev. Mater. Res. **34,** 1–40 (2004).

[8] S. Bose, "Quantum Communication through an Unmodulated Spin Chain," Phys. Rev. Lett. **91,** 1–4 (2003).

[9] M. Sugawara, in *Self-Assembled InGaAs/GaAs Quantum Dots*, M. Sugawara, ed., (Academic Press, 1999), pp. 1–116.

[10] R. E. Howard, W. J. Skocpol, and L. D. Jackel, "Nanostructures," Annual Review of Materials Science **16,** 441–466 (1986).

[11] H. Schrift, "Nanoimprint lithography: An old story in modern times? A review," Journal of Vacuum Science & Technology B: Microelectronics and Nanometer Structures **26,** 458–480 (2008).

[12] X. Li, "Metal assisted chemical etching for high aspect ratio nanostructures: A review of characteristics and applications in photovoltaics," Current Opinion in Solid State and Materials Science **16,** 71–81 (2012).

[13] M. DeJarld, J. C. Shin, W. Chern, D. Chanda, K. Balasundaram, J. A. Rogers, and X. Li, "Formation of high aspect ratio GaAs nanostructures with metal-assisted chemical etching," Nano Lett. **11,** 5259–5263 (2011).

[14] Z. M. Wang, S. Seydmohamadi, J. H. Lee, and G. J. Salamo, "Surface ordering of (In,Ga)As quantum dots controlled by GaAs substrate indexes," Appl. Phys. Lett. 85 (2004).

[15] Z. M. Wang, H. Churchill, C. E. George, and G. J. Salamo, "High anistropy of lateral alignment in multilayered (In,Ga)As/GaAs(100) quantum dot structures," Journal of Applied Physics 96 (2004).

[16] Z. M. Wang, L. Zhang, K. Holmes, and G. J. Salamo, "Selective etching of InGaAs/-GaAs(100) multilayers of quantum-dot chains," Appl. Phys. Lett. 86 (2005).

[17] T. V. Hakkarainen, J. Tommila, A. Schramm, A. Tukiainen, R. Ahorinta, M. Dumitrescu, and M. Guina, "Structural characterizatio of InAs quantum dot chains grown by molecular beam epitaxy on nanoimprint lithography patterned GaAs(100)," Nanotechnology **22,** 295604 (2001).

[18] T. V. Hakkarainen, A. Schramm, J. Tommila, and M. Guina, "The effect of InGaAs strain-reducing layer on the optical properties of InAs quantum dot chains grown on patterned GaAs(100)," Journal of Appl. Phys. **111,** 014306 (2012).

[19] T. V. Hakkarainen, V. Polojärvi, A. Schramm, J. Tommila, and M. Guina, "The influence of post-growth annealing on the optical properites of InAs quantum dot chains grown on pre-patterned GaAs(100)," Nanotechnology **23,** 115702 (2012).

[20] D. J. Kim and H. Yang, "Shape control of InGaAs nanostructures on nominal GaAs(001): dashes and dots," Nanotechnology 19 (2008).

[21] S. Yang, A. Bayat, and S. Bose, "Spin state transfer in latterally coupled quantum dot chains disorders," Phys. Rev. A **82,** 022336 (2010).

[22] M. Koecher, J. Yeager, T. Park, D. Fullwood, J. Colton, N. Mara, and N. Hansen, "Characterization of Nickel Nanostrand Nanocomposites through Dielectric Spectroscopy and Nanoindentation," Polymer Engineering and Science (2013).

[23] K. S. Cole and R. H. Cole, "Dispersion and Absorption in Dielectrics - I Alternating Current Characteristics," J. Chem. Phys. **9,** 341–352 .

[24] J. Fritzsche, H. Lorenz, and M. Klüppel, "CNT Based Elastomer-Hybrid-Nanocomposites with Promising Mechanical and Electrical Properties," Macromolecular Materials and Engineering **294,** 551–560 (2009).

[25] J. S. Colton, D. Meyer, K. Clark, D. Craft, J. Cutler, T. Park, and P. White, "Long-lived electron spins in a modulation doped (100) GaAs quantum well," Journal of Applied Physics **112,** 084307 (2012).

[26] P. Weinberger, "John Kerr and his effects found in 1877 and 1878," Philisophical Magazine Letters 88 (2008).

[27] J. Colton, K. Clark, D. Meyer, T. Park, D. Smith, and S. Thalman, "Universal scheme for measuring the electron T1 in semiconductors and applications to a lightly-doped n-GaAs sample," Solid State Communications **152,** 410–413 (2012).

[28] A. Garcia, *Numerical Methods for Physics*, 2nd ed.

[29] G. Metze and A. Calawa, "Effects of very low growthrates on GaAs grown by molecular beam epitaxy at low substrate temperatures," Appl. Phys. Lett. **9,** 818–820 (1982).

[30] K. Ploog, "Molecular beam epitaxy of III-V compounds: technology and growth process," Annual Review of Materials Science **11,** 171–210 (1981).

[31] D. W. Pashley, J. H. Neave, and B. A. Joyce, "A model for the appearance of chevrons on RHEED patterns from InAs quantum dots," Surface Science **476 (1),** 35–42 (2001).

[32] I. N. Stranski and L. von Krastanow, Abhandlungen der Mathematisch-Naturwissenschaftlichen Klasse IIb. **146,** 797–810 (1938).

[33] D. Leonard, M. Krishnamurthy, C. M. Reaves, S. P. Denbaars, and P. M. Petroff, "Direct formation of quantum-sized dots from uniform coherent islands of InGaAs on GaAs surfaces," Appl. Phys. Lett. **63,** 3206 .

[34] D. Leonard, K. Pond, and P. M. Petroff, "Critical layer thickness for self-assembled InAs islands on GaAs," Phys. Rev. B **50,** 11687 .

[35] W.-H. Chang, T.-M. Hsu, K.-F. Tsai, T.-E. Nee, J.-I. Chyi, and N.-T. Yeh, "Excitation Density and Temperature Dependent Photoluminescence of InGaAs Self-Assembled Quantum Dots," Jpn. J. Appl. Phys. **38,** 554–557 (1999).

[36] T. Walther, A. G. Cullis, D. J. Norris, and M. Hopkinson, "Nature of the Stranski-Krastanow Transition during Epitaxy of InGaAs on GaAs," Phys. Rev. Lett. **86,** 2381–2384 (2001).

[37] A. Sauerwalkd, T. Kümmell, G. Bacher, A. Somers, R. Schwertberger, J. P. Reithmaier, and A. Forchel, "Size control of InAs quantum dashes," Applied Physics Letters **86,** 253112 (2005).

[38] J. H. Lee, Z. M. Wang, B. L. Liang, W. T. Black, V. P. Kunets, Y. I. Mazur, and G. J. Salamo, "Selective growth of InGaAs/GaAs quantum dot chains on pre-patterned GaAs(100)," Nanotechnology **17,** 2275 (2006).

[39] J. M. García, J. P. Silveira, and F. Briones, "Strain relaxation and segregation effects during self-assembled InAs quantum dots formation on GaAs(001)," Appl. Phys. Lett 77 (2000).

[40] A. Ohtake and M. Ozeki, "In situ observation of surface processes in InAs/GaAs(001) heteroepitaxy: The role of As on the growth mode," Appl. Phys. Lett. **78,** 431–433 (2001).

[41] G. Biasiol, S. Heun, G. B. Golinelli, A. Locatelli, T. O. Mentes, F. Z. Guo, C. Hofer, C. Teichert, and L. Sorba, "Surface compositional gradients of InAs/GaAs quantum dots," Appl. Phys. Lett. **87,** 223106 (2005).

[42] S. Sanguinetti, T. Mano, M. Oshima, T. Tateno, M. Wakaki, and N. Koguchi, "Temperature dependence of the photoluminescence of InGaAs/GaAs quantum dot structures without wetting layer," Appl. Phys. Lett **81,** 3067–3069 (2002).

[43] S. Raymond, X. Guo, J. L. Merz, and S. Farad, "Excited-state radiative lifetimes in self-assembled quantum dots obtained from state-filling spectroscopy," Physical Review B **59,** 7624–7630 (1999).

[44] R. P. Mirin, J. P. Ibbetson, K. Nishi, A. C. Gossard, and J. E. Bowers, "1.3 μm photoluminescence from InGaAs quantum dots on GaAs," Appl. Phys. Lett. **67,** 3795–3797 (1995).

[45] X. Y. Wang, W. Q. Ma, J. Y. Zhang, G. J. Salamo, M. Xiao, and C. K. Shih, "Photoluminescence intermittency of InGaAs/GaAs quantum dots confined in a planar microcavity," Nano Lett. **5,** 1873–1877 (2005).

[46] L. Reimer, *Transmission Electron Microscopy: Physics of Image Formation and Microanalysis* (Springer-Verlag, 1984).

[47] D. B. Williams and C. B. Carter, *Transmission Electron Microscopy: Basics* (Plenum Press, 1996), Vol. 1.

[48] L. Reimer, *Transmission Electron Microscopy: Physics of Image Formation and Microanalysis* (Springer-Verlag, 1984).

[49] E. Rutherford, "The scattering of α and β particles by matter and the structure of the atom," Philosophical Magazine 21 (1911).

[50] G. F. Iriarte, "Using transmission electron microscopy (TEM) for chemical analysis of semiconductors," Microscopy: Science, Technology, Applications and Eduation .

[51] L. A. J. Garvie and A. J. Craven, "Parallel electron energy-loss spectroscopy (PEELS) study of B in minerals: The electron energy-loss enar structure (ELNES) of the B K edge," American Minerologist **80,** 1132–1144 (1995).

[52] F. A. Stevie *et al.*, "Application of focused ion beam lift-out specimen preparatio nto TEM, SEM, STEM, AES and SIMS analysis," Surface and Interface Analysis **31,** 345–351 (2001).

[53] A. O. Kosogov *et al.*, "Structural and optical properties of InAs-GaAs quantum dots subjected to high temperature annealing," Appl. Phys. Lett. **69,** 3072 (1996).

[54] P. Werner, K. Scheerschmidt, N. D. Zakharov, R. Hillebrand, M. Grundmann, and R. Schneider, "Quantum dot structures in the InGaAs system investigated by TEM techniques," Cryst. Res. Technol. **35,** 759–768 (2000).

[55] R. Anderson and S. J. Klepeis, "Combined tripod polishing and FIB method for preparing semiconductor plan view specimens," MRS Proceedings 480 (1997).

[56] H. Yang, D.-J. Kim, J. Colton, T. Park, A. Jones, S. Thalman, D. Smith, K. Clark, D. Meyer, and S. Brown, "Critical annealing temperature for InGaAs quantum nanostructures," submitted to Journal of Vacuum Science and Technology in June 2013 .

[57] D. J. Kim, E. A. Everett, and H. Yang, "Annealing induced transition of flat strained InGaAs epilayers into three-dimensional islands," Journal of Applied Physics **101,** 106106 (2007).

[58] D. J. Kim, D. Cha, G. J. Salamo, and H. Yang, "Enabling in situ atomic scale surface imaging for verticle molecular beam epitaxy machines," Journal of Vacuum Science & Technology B: Microelectronics and Nanometer Structures **24,** 2776–2778 (2006).

[59] L. Hao, R. Lowe-Webb, W. Yang, and P. C. Sercel, "Determination of the shape of self-organized InAs/GaAs quantum dots by reflection high energy electron diffraction," Applied Physics Letters 72 (1998).

[60] T. H. Gfroerer, "Photoluminescence in Analysis of Surfaces and Interfaces," Encyclopedia of Analytical Chemistry pp. 9209–9231 (2000).

[61] Y. I. Mazur, W. Q. Ma, X. Wang, Z. M. Wang, G. J. Salamo, M. Xiao, T. D. Mishima, , and M. B. Johnson, "InGaAs/GaAs three-dimensionally-ordered array of quantum dots," Appl. Phys. Lett. **83,** 987 (2003).

[62] K. Kamath, P. Bhattacharya, T. Sosnowski, T. Norris, and J. Phillips, "Room-temperature operation of In0.4Ga0.6As/GaAs self-organized quantum dot lasers," Electronics Letters **32,** 1374 (1996).

[63] S. Raymond, S. Fafard, P. J. Poole, A. Wojs, P. Hawrylak, S. Charbonneau, D. Leonard, R. Leon, P. M. Petroff, and J. L. Merz, "State filling and time-resolved photoluminescence of excited states in $In_xGa_{1-x}As/GaAs$ self-assembled quantum dots," Phys. Rev. B **54,** 11548 (1996).

[64] T. Nuytten, M. Hayne, M. Henini, and V. V. Moshchalkov, "Temperature dependence of the photoluminescence of self-assembled InAs/GaAs quantum dots in pulsed magnetic fields," Phys. Rev. B **77,** 115348 (2008).

[65] Y. P. Varshni, "Temperature dependence of the energy gap in semiconductors," Physica **34,** 149–154 (1967).

[66] K.-H. Goetz, D. Bimberg, H. Jürgensen, J. Selders, A. V. Solomonov, G. F. Glinskii, and M. Razeghi, "Optical and crystallographic properties and impurity incorporation of $Ga_xIn_{1-x}As$ (0.44<x<0.49) grown by liquid phase epitaxy, vapor phase epitaxy, and metal organic chemical vapor deposition," Journal of Applied Physics **54,** 4543 (1983).

[67] A. Polimeni, A. Patanè, M. Henini, L. Eaves, and P. C. Main, "Temperature dependence of the optical properties of $InAs/Al_yGa_{1-y}As$ self-organized quantum dots," Physical Review B **59,** 5064 (1999).

[68] J.-P. Reithmaier, H. Riechert, H. Schlötterer, and G. Weimann, "Indium desorption during MBE growth of strained InGaAs layers," Journal of Crystal Growth **111,** 407–412 (1991).

[69] S. Fafard, S. Raymond, G. Wang, R. Leon, D. Leonard, S. Charbonneau, J. L. Merz, P. M. Petroff, and J. E. Bowers, "Temperature effects on the radiative recombination in self-assembled quantum dots.(Report)," Surface Science **361-362,** 778(5) (1996).

[70] K. Mukai, N. Ohtsuka, and N. Sugawara, "High photoluminescence efficiency of InGaAs/-GaAs quantum dots self-formed by atomic layer epitaxy technique," Appl. Phys. Lett. **70,** 2416–2418 (1997).

[71] M. Grundmann *et al.*, "Ultranarrow luminescence lines from single quantum dots," Phys. Rev. Lett. **74,** 4043–4046 (1995).

[72] V. Lindberg, "Uncertainties and Error Propagation: Part I of a manual on Uncertainties, Graphing, and the Vernier Caliper,", 2000.

Appendix A

MATLAB Code for a Dual-Well System

This code is a MATLAB code for a dual-well system as described in Chapter 1 of the thesis. The dual well has delta-dirac barriers at x=0 and x=+50, but the example only shows interaction with the barrier at x=0.

```
% schro − Program to solve the Schrodinger equation
% for a free particle using the Crank−Nicolson scheme
clear all; help schro; % Clear memory and print header

%% ∗ Initialize parameters (grid spacing, time step, etc.)
i_imag = sqrt(−1); % Imaginary i
N = input('Enter number of grid points: ');
L = 100; % System extends from −L/2 to L/2
h = L/(N−1); % Grid size
x = h∗(0:N−1) − L/2; % Coordinates of grid points
h_bar = 1; mass = 1; % Natural units
tau = input('Enter time step: ');
```

```
U = input('Enter the amplitude of the delta potential: ');


%% * Set up the Hamiltonian operator matrix
ham = zeros(N); % Set all elements to zero
coeff = -h_bar^2/(2*mass*h^2);
for i=2:(N-1)
   ham(i,i-1) = coeff;
   ham(i,i) = -2*coeff; % Set interior rows
   ham(i,i+1) = coeff;
end
% First and last rows for periodic boundary conditions
ham(1,N) = coeff; ham(1,1) = -2*coeff; ham(1,2) = coeff;
ham(N,N-1) = coeff; ham(N,N) = -2*coeff; ham(N,1) = coeff;
ham(N,N) = ham(N,N) * U/h;
ham(N/2,N/2) = ham(N/2,N/2) * U/h


%% * Compute the Crank-Nicolson matrix
dCN = ( inv(eye(N) + .5*i_imag*tau/h_bar*ham) * ...
                    (eye(N) - .5*i_imag*tau/h_bar*ham) );


%% * Initialize the wavefunction
x0 = -L/4; % Location of the center of the wavepacket
velocity = 0.5; % Average velocity of the packet
```

```
k0 = mass*velocity/h_bar; % Average wavenumber
sigma0 = L/20; % Standard deviation of the wavefunction
Norm_psi = 1/(sqrt(sigma0*sqrt(pi))); % Normalization
psi = Norm_psi * exp(i_imag*k0*x') .* ...
                        exp(-(x'-x0).^2/(2*sigma0^2));

%% * Plot the initial wavefunction
figure(1); clf;
plot(x,real(psi),'-',x,imag(psi),'--');
title('Initial wave function');
xlabel('x'); ylabel('\psi(x)'); legend('Real ','Imag ');
drawnow; pause(1);

%% * Initialize loop and plot variables
max_iter = L/(velocity*tau); % Particle should circle system
plot_iter = max_iter/20; % Produce 20 curves
p_plot(:,1) = psi.*conj(psi); % Record initial condition
iplot = 1;
figure(2); clf;
axisV = [-L/2 L/2 0 max(p_plot)]; % Fix axis min and max

%% * Loop over desired number of steps (wave circles system once)
for iter=1:max_iter

  %* Compute new wave function using the Crank-Nicolson scheme
```

```
  psi = dCN*psi;

  %* Periodically record values for plotting
  if( rem(iter,plot_iter) < 1 )
    iplot = iplot+1;
    p_plot(:,iplot) = psi.*conj(psi);
    plot(x,p_plot(:,iplot)); % Display snap-shot of P(x)
    xlabel('x'); ylabel('P(x,t)');
    title(sprintf('Finished %g of %g iterations',iter,max_iter));
    axis(axisV); drawnow;
    F(iplot-1) = getframe;
  end


end

%% * Plot probability versus position at various times
pFinal = psi.*conj(psi);
plot(x,p_plot(:,1:3:iplot),x,pFinal);
xlabel('x'); ylabel('P(x,t)');
title('Probability density at various times');

movie(F,10,6);
```

Appendix B

Characterization of Nickel Nanostrand Nanocomposites Through Dielectric Spectroscopy and Nanoindentation

As mentioned in Chapter 1 of the thesis, one of the other projects I have been involved in deals with nickel nanostrand nanocomposites and characterizing them using dielectric spectroscopy. My involvement includes programming the LabView code that controls the capacitance measurement scans, measuring the capacitances of each of the samples, calculating the relative permittivity of each sample, curve fitting the permittivity vs. frequency measurements with the Cole-Cole equation, and calculating the average junction distance between nanostrands using the fitting parameters obtained from fitting. This included paper details the experimental setup and lists the measured and calculated values.

Characterization of Nickel Nanostrand Nanocomposites Through Dielectric Spectroscopy and Nanoindentation

Michael Koecher,[1] John D. Yeager,[2] Tyler Park,[1] David Fullwood,[1] John S. Colton,[1] Nathan Mara,[2] Nathan Hansen[3]
[1] *435 CTB, Brigham Young University, Provo, Utah 84602*

[2] *Los Alamos National Laboratory, Los Alamos, New Mexico 87545*

[3] *Conductive Composites, 357 West 910 South, Heber City, Utah 84032*

One particularly promising model of electrical properties of conductive nanocomposites involves a combined quantum tunneling/percolation approach. However, two key inputs to the model—the polymer matrix barrier height and the average gap between conductive filler particles—are difficult to determine experimentally. This article demonstrates improved methods for determining barrier height in polymer materials via conductive nanoindentation, with barrier heights measured between 0.4 and 1.7 eV for five different polymers. By using dielectric spectroscopy techniques, combined with the barrier height measurements, the average junction gap was determined for the first time for nickel-nanostrand nanocomposites with six different polymer matrices; the values range from 1.31 to 3.28 nm. Using those measured values for barrier height and junction gap distances in a simple model, we have tested predictions for bulk resistivity of six polymers. The model worked well for four of the six, which suggests that for a given volume fraction of filler, knowledge of the barrier height and the junction distance may in many cases be sufficient to provide an estimate of the bulk resistivity of the polymer-nanostrand blend, an important parameter in nanocomposite engineering. POLYM. ENG. SCI., 00:000–000, 2013.

The work was performed, in part, at the Center for Integrated Nanotechnologies, a U.S. Department of Energy, Office of Basic Energy Sciences user facility. Los Alamos National Laboratory, an affirmative action equal opportunity employer, is operated by Los Alamos National Security, LLC, for the National Nuclear Security Administration of the U.S. Department of Energy under contract DE-AC52-06NA25396. Yeager is supported by an Agnew National Security Postdoctoral Fellowship. Various materials and samples were produced and donated by Conductive Composites Company, Heber City, UT.
Correspondence to: David Fullwood; e-mail: dfullwood@byu.edu
Contract grant sponsor: NSF; contract grant number: CMMI-1235365.
DOI 10.1002/pen.23511
Published online in Wiley Online Library (wileyonlinelibrary.com).

INTRODUCTION

Interest in nanocomposites has multiplied in the past few years due to the advantageous material properties obtained when nanoscale particles are combined with a bulk material [1]. Vital properties such as conductivity can be modified by using nanoparticles or nanosized wires [2–4]. These specialized conductive nanocomposites are finding many applications in industry such as electromagnetic interference shielding [5], flexible circuits, and high fatigue life electrodes for biomedical applications [6]. One promising function of conductive nanocomposites exploits the piezoresistivity that they exhibit to measure strain in a material [6–8].

Common conductive fillers used in these nanocomposites are carbon nanotubes[9], carbon black [10], and nickel nanostrands (Ni-Nss) [11]. Although multiple research articles have focused on carbon nanotubes and carbon black, recent research into Ni-Ns fillers has demonstrated the potential to increase bulk conductivity beyond that of typical carbon-based nanocomposites [12].

Ni-Nss exhibit a highly bifurcated structure with a high aspect ratio and a nanometer scale diameter (Fig. 1). This unique structure promotes electrical conductivity at very small volume fractions of Ni-Ns and improved conductivity compared to many other filled nanocomposites [13, 14] (see Table 1 for percolation thresholds and percolation limits based on several of the polymers studied in this article; the percolation indicates when the matrix is saturated with filler, and conductivity does not significantly increase beyond this volume percentage). Similar to various other nanocomposites with conductive fillers [15–18], Ni-Ns-based nanocomposites show a substantial change in resistance when placed under strain [12]. To better understand the piezoresistivity of the nanocomposite an accurate model of the relationship between microstructure and conductivity is required.

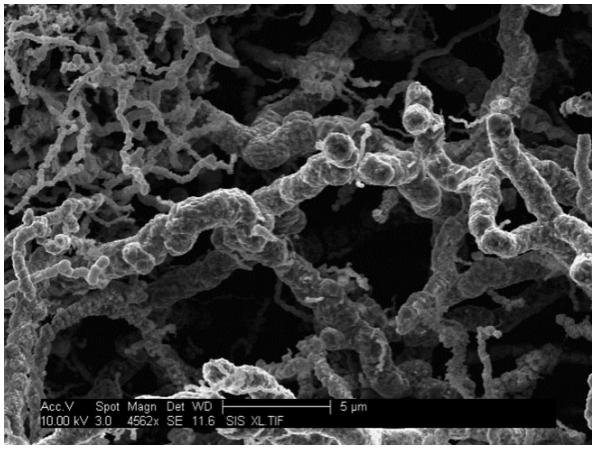

FIG. 1. Scanning electron micrograph of nickel nanostrands using a Philips XL30 ESEM FEG at 10 kV and a spot size of 3.

The conductivity of nanocomposites of this type is commonly (and perhaps, most successfully) modeled using percolation theory in conjunction with quantum tunneling [19, 20]. In this approach, the bulk conductivity is dominated by resistance across nanoscale gaps between conductive strands. The sizes of the gaps are generally assumed to be controlled by the thickness of an adsorbed layer of polymer that separates the filler particles. When the gaps are on the order of a nanometer, quantum tunneling enables electron flow across the otherwise insulating polymer matrix. The sensitivity of resulting electrical flow to the gap size allows the junction between filler particles to be considered a switch; the switch is "on" if the gap is small enough to allow significant electron flow, and "off" otherwise. This view of a network of switches then fits well with a percolation model. As the number of "on" switches increases the probability of electrical flow across the bulk material rises, with a rapid increase in flow once a path of "on" switches crosses the whole material at the percolation threshold. This modeling approach is most likely to be able to predict the piezoresistive phenomena, which is not captured by models that consider only volume fraction or filler orientation/alignment.

Perhaps the biggest difficulty facing general adoption of percolation/tunneling models in the analysis of conductive nanocomposites relates to the lack of information regarding the distribution of junctions across the filler network, including gap-size, and the quantum tunneling barrier height for matrix polymers. The former relates to the adsorbed layer thickness for the matrix polymer, and the latter dictates the resistance versus gap size for the junctions. In this article, we use dielectric spectroscopy techniques to obtain the average junction size, and a new nanoindentation technique to obtain the barrier height for a given polymer, and apply these to a simple percolation/tunneling model for the nanocomposites being tested. The resultant model shows promise for several matrix materials. More sophisticated models, based on the fundamental physical parameters uncovered using the methods in this article, could readily be formulated for general conductive composites applications.

TABLE 1. Percolation thresholds and limits (in volume percent) for several polymers filled with nickel nanostrands.

Tradename/type	Percolation threshold (%)	Percolation limit (%)	Conductivity at percolation limit (S/cm)
Desothane® urethane	0.017	0.15	58
Irogran® TPU	0.015	0.15	630
Polycrylic® acrylic urethane	0.016	0.20	250
Sylgard® silicone	0.055	0.20	12

Percolation Theory and Quantum Tunneling

Percolation theory examines the distribution of, and connections between, locations in a conductive network, termed "sites." Between two sites, there is some probability that an electrical connection exists. These connections/switches are referred to as "bonds." If the number of bonds is increased beyond a level known as the percolation threshold, a conductive network is created and a dramatic decrease in the resistivity of the nanocomposite results. One commonly assumed relationship between the probability of individual bond formation and the overall conductivity of a material (and the view taken in this article) is shown in *Eq. 1*:

$$\sigma_c \sim (p - p_c)^t \tag{1}$$

where σ_c is the effective conductivity of the composite, t is a scaling law exponent, p is the probability of a given bond being present between two chosen neighboring sites, and p_c is the critical bond probability for percolation to occur [21, 22]. In a nanocomposite, the sites are conductive nanoparticles and the bonds are junctions between nanoparticles that are conducive to electron tunneling through the insulating polymer.

The percolation model requires that quantum tunneling occur to create (or "switch on") the bonds which are essential for a conductive network in the nanocomposite. The tunneling resistivity in the barrier between two conductive particles is

$$\rho = \frac{2h^2}{3e^2\sqrt{2m_e\lambda}} \exp\left(\frac{4\pi\sqrt{2m_e\lambda}}{h}\delta\right) \tag{2}$$

where h is the Planck constant, e is the charge of an electron, m_e is the mass of an electron, λ is the barrier height, and δ is the junction distance [23]. Thus quantum tunneling (and the related probability of a bond occurring in the percolation model) is dependent on the barrier height λ and the junction distance between conductive nanostrands, δ.

We note at this point that the traditional application of percolation theory to conductive composites assumes that the conductive particles themselves are the bonds, and hence the probability of bond occurrence is proportional

DOI 10.1002/pen

to the volume fraction of the conductive filler. In quantum tunneling/percolation model the resistivity of the filler is assumed to be negligible compared with that of the junctions between particles, hence the probability of bond occurrence relates to the volume fraction of junctions with a small enough gap, and low enough barrier height, to enable significant conductance. This probability will no doubt be influenced by filler volume fraction because a higher volume fraction will press the particles closer together, decreasing the average junction gap. Furthermore, more filler particles per unit volume will increase the number of neighbors for each site, hence affecting the percolation threshold. However, we will not consider volume fraction of filler directly in this article, but will hold it constant for the tests on different polymers.

The particular insulating polymer between nanostrands dictates the barrier height, λ, as well as the minimum junction distance, δ, between strands. With the knowledge of the minimum junction distance and the barrier height for individual polymers an accurate percolation model for Ni-Ns-filled nanocomposites can be obtained.

The minimum junction distance between particles depends heavily on the interaction of polymer chains with the nanoparticle. The portions of the polymer chains closest to the particle become immobilized or bound to the surface of the particle [24]. This layer is called the adsorbed layer and its thickness can been calculated using nuclear magnetic resonance [25], transmission electron microscopy (TEM) coupled with scanning tunneling microscopy (STM) [26], TEM coupled with thermal gravimetric analysis methods [27], and dissolution methods [28]. Each of these methods assumes that the minimum junction distance is twice the adsorbed layer thickness. Klüppel [29] discovered that by simply measuring the permittivity versus frequency curves with dielectric spectroscopy the average junction distance between nanoparticles can be obtained. When the volume fraction of filler is above the traditional percolation threshold (enough filler is present to create a path of filler across the sample), it is assumed that dielectric spectroscopy will yield the average tunneling gap across nanojunctions, and that this distance will be close to twice the adsorbed layer thickness. Dielectric spectroscopy has been used to measure the junction distance with carbon black [30] and carbon nanotube [23] nanocomposites; the distance has been shown to vary with polymer. No such study currently exists for Ni-Ns nanocomposites.

Woo et al. [31] demonstrated that minute changes in a liquid barrier material had significant effects on the tunneling distance between gold particles. This suggests that percolation models for conductive nanocomposites also require precise determination of the barrier height for the polymer material used as the matrix. Previous studies have used STM to measure the barrier height of a substance [32, 33]. STM techniques require an aqueous solution to represent the barrier material. This can be a limitation for many complex materials, both in terms of sample preparation and assumptions required to compare the aqueous solution to the actual solid composite. Johnson et al. [7] implemented a new method described as nanoindentation tunneling microscopy (NTM) to calculate barrier heights in solid barrier materials (e.g. cured polymer). In this indentation method, a conductive indentor tip is pressed through a thin film of the material and into a conductive substrate while the instrument measures the gap distance and conductance simultaneously.

Here, we present an extension of Johnson et al.'s work, with an improved and simplified nanoindenter setup and subsequent analysis, to calculate barrier heights for common and complex polymer materials of interest for formulation of nickel nanocomposites. Barrier height measurements of the pure polymers are complemented with dielectric measurements of Ni-Ns-filled polymers to calculate junction distance. By combining these two techniques we can quantitatively determine the potential of the various polymers for multifunctional Ni-Ns composites.

EXPERIMENTATION

Material and Sample Preparation

The Ni-Nss used in the research were provided by Conductive Composites Company (Heber, UT). The polymers studied are widely available commercial products described in Table 2. These polymers have the advantage of being easy to use, relevant to commercial applications, and previously studied in Ni-Ns nanocomposite systems [34]. The dielectric measurements required polymers which contained dispersed Ni-Ns, forming a percolating conductive nanocomposite. The dispersion was accomplished by

TABLE 2. Polymers used in this study with accompanying solvents used for processing.

Name	Manufacturer	Type	Processing solvent
Armorseal® 1000 HS clear	Sherwin Williams®	Epoxy	MEK/xylene/ethanol
CARC Clear MIL-DTL-64159 Ty II	Spectrum Coatings	Aliphatic polyurethane	Water
CP1 (LaRC-CP1)®	NeXolve®	Polyimide	Diglyme
Desothane® HS CA8201/F Clear	PRC-DeSoto	Urethane	Methyl ethyl ketone
Irogran® PS455–302P (IRO)	Huntsman	Thermoplastic polyurethane	Tetrahydrofuran
Polycrylic®	Minwax®	Acrylic/urethane	Water
Sylgard 184	Dow Corning®	Silicone	Xylol

adding Ni-Ns and solvent (if necessary) to the uncured polymer and mixing with a standard planetary mixer. The solvents used for each polymer are given in Table 2. The uncured nanocomposites were placed into molds to create dielectric disc shaped samples that were 1 in. in diameter and between 0.05 and 0.1 in. thick. The polymers were then cured according to the manufacturer's specifications.

Barrier height measurements of the pure polymers required extremely thin polymer samples to simulate the nanometer scale gap distances commonly found in the conductive nanocomposites. This was accomplished by depositing thin films of the polymers onto nickel substrates. Nickel substrates were polished with standard slurry polishing procedures followed by a final electropolishing step to minimize surface roughness. Substrates were then cleaned with an acetone wash and 5 min of atmospheric plasma etching immediately before coating. Polymer films were fabricated on the nickel substrates by use of a controlled dip-coating procedure which has been previously established to create nanometer-scale organic films [35]. Briefly, the polymers of interest were dissolved in appropriate organic solvents (Table 2) to create solutions of approximately 1 wt%, and the nickel substrates were dipped into and removed from the solutions in humidity-regulated room temperature environment at a constant speed of 25 mm/min. The samples appeared dry after several seconds but were allowed to dry for a minimum of 24 h before analyzing. The thicknesses of the polymers were measured by a variable angle spectroscopic ellipsometer from J.A. Woolam Co. (Lincoln, NE) [36].

Barrier Height Measurement

For the purposes of nanocomposites or other conductor-insulator-conductor systems, the barrier height λ is defined as the energy difference between the conduction band of the insulator and that of the conductor. *Equation 2* shows the interrelationship of λ and the junction distance with the tunneling properties of the composite. To obtain λ for the polymers in Table 2, a conductive nanoindentation scheme was used which was modified from our initial reported attempts [37]. The previous work cannibalized a nanoindenter with a conductive tip and an *ad hoc*, and somewhat noisy, electrical circuit to determine the resistance versus height across the gap of thin film samples of a single matrix material (Silgard). Newly developed functionality for the Hysitron TriboIndenter, used in conjuction with a boron-doped conductive diamond tip and conductivity measurement software (nanoECR®), allowed far more accurate continuous measurement of the current and voltage between the tip and the substrate during indentation of a range of polymer samples. A gold standard was used for calibrating the system at an applied bias of 1 V, and a typical current versus depth (s) curve is shown in Fig. 2.

We note that the barrier height is a function of both the polymer and the substrate material (in this case nickel). Ideally the height would be measured for a thin film of polymer between two nickel probes, representing two nanoparticles. Original trials with a nickel coated nanoindenter tip were unsuccessful due to damage to the tip. Hence substituting the boron-doped diamond tip for one polymer/nickel interface introduces some error into the barrier height determination, compared to that of the nanocomposite material. We expect that the error will be low; furthermore, the resultant relative barrier heights between the various polymers will be indicative of the true relative values despite any unintended bias in the readings.

Traditional explorations of barrier height phenomena describe tunneling theory in terms of conductance, though the actual current is used here. The tunneling conductance equation is

$$G = G_0 \exp(-1.025\sqrt{\lambda}s) \tag{3}$$

where G_0 is the conductance when the plate and tip are in contact, λ is the barrier height, and s is the distance from indenter tip to plate [31]. Linearizing *Eq. 3*, the following is obtained:

$$\ln(G) = -1.025\sqrt{\lambda}s + \ln(G_0). \tag{4}$$

Thus, with knowledge of the conductance as a function of gap distance the barrier height can be calculated from the slope of an ln(G) versus s plot; the slope, m, is

$$m = -1.025\sqrt{\lambda}. \tag{5}$$

Using linear regression to solve for the slope the mean barrier height can be obtained:

$$\lambda = \left(\frac{m}{1.025}\right)^2. \tag{6}$$

The nanoECR setup measures current as a function of depth for a given voltage, or voltage as a function of

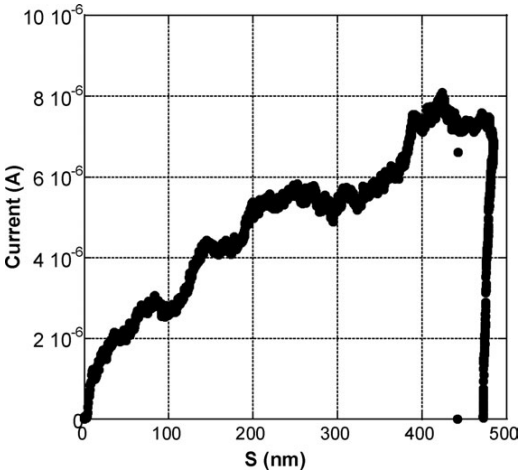

FIG. 2. Current as a function of indentation depth for gold at 1 V.

DOI 10.1002/pen

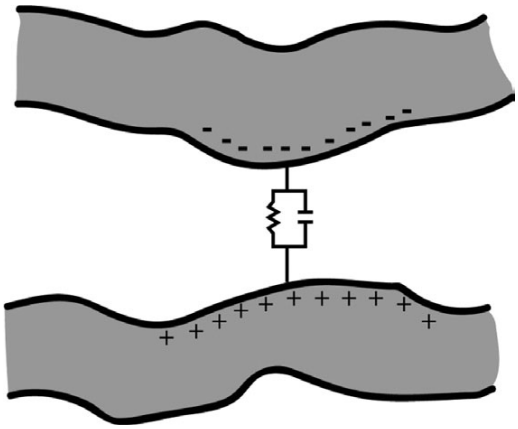

FIG. 3. Parallel resistor and capacitor model of nanojunctions.

depth for a given current. The software provides an excellent way to obtain conductance data: indentation is performed to a given depth, at which point an I–V sweep is performed to measure conductance directly. However, results given by this method were considered unreliable for our very thin and compliant polymer films due to the difficulty of finding the exact position of the polymer surface, and the possibility of creep of the polymer while the indenter was held at a given depth. Both factors would significantly convolute the data. Thus, we decided to only use the accurately measured current versus depth data and assume the voltage varied linearly (from 0 to the applied bias) over the junction distance. This assumption was chosen based on our previous experience, in which the voltage was approximately exponential over the course of the entire indent but largely linear over the range of interest [37].

Junction Distance Measurement

The junction between conductive nanoparticles in a nanocomposite has been successfully modeled as a resistor and capacitor circuit in parallel, as is illustrated in Fig. 3 [23, 30, 38–40]. In this model the dielectric response is treated as a gigantic network of these resistor–capacitor circuits.

With this circuit model the characteristic frequency at a nanojunction is

$$\omega_c = \frac{1}{RC} \tag{7}$$

where ω is relaxation frequency, R is the resistance, and C is the capacitance. For capacitance

$$C = \frac{\varepsilon_0 \varepsilon A}{\delta} \tag{8}$$

where ε_0 is the permittivity of free space, and ε is the relative permittivity (often referred to as the dielectric constant). Inserting *Eq. 8* and an altered *Eq. 2* using $R = \rho l/A = \rho\delta/A$ into *Eq. 7* we obtain

$$\omega_c \frac{3e^2}{8\pi h\varepsilon_0}\frac{k_0}{\varepsilon}e^{-k_0\delta} \tag{9}$$

where $k_0 = 4\pi\sqrt{(2m_e\lambda)}/h$. Thus, with knowledge of the characteristic frequency, ω_c, the junction distance, δ, can be calculated.

To obtain the characteristic frequency, the relative permittivity is needed at various frequencies. An HP model 4192A impedance analyzer with a frequency range of 5 Hz to 13 MHz was used. Stray admittance and residual impedance are sources of error with this equipment. To eliminate these errors an HP 16451B dielectric test fixture for dielectric constant measurement of solid materials was attached. The electrode used in this fixture was a 5-mm guarded electrode which eliminates edge capacitance error.

Depending on the polymer used there was varying amount of roughness and compressibility in the samples being tested. To prevent these variables from affecting the results, a noncontacting electrode method was used per the manufacturer's specifications. In this method two tests are run using the analyzer, one with the sample between the parallel plates of the analyzer and the other without the sample between the plates (see Fig. 4). When the sample is between the parallel plates it is modeled as two parallel capacitors (sample-filled region and the air space region). The relative permittivity can then be calculated using *Eq. 10*

$$\varepsilon_r = \frac{1}{1-\left(1-\frac{C_{s1}}{C_{s2}}\right)\frac{s_g}{s_a}} \tag{10}$$

where ε_r is the relative permittivity, C_{s1} is the capacitance without the sample inserted, C_{s2} is the capacitance with the sample inserted, s_g is the distance between electrodes, and s_a is the thickness of the sample.

Measuring the relative permittivity with a broad range of frequencies the Cole–Cole equation (*Eq. 11*) can be used to fit the dielectric data [41]. It is noted that using a single real term of summation obtains good fits. The fit yields values for σ_{dc}, the relaxation time τ, the relaxation strength $\Delta\varepsilon$, and the broadness parameter α. Because $\omega_c = 1/\tau$ the characteristic frequency can be obtained and

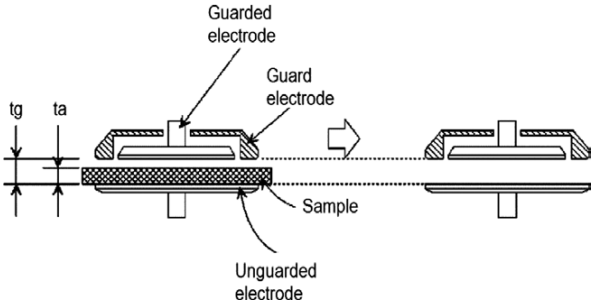

FIG. 4. Noncontacting electrode method.

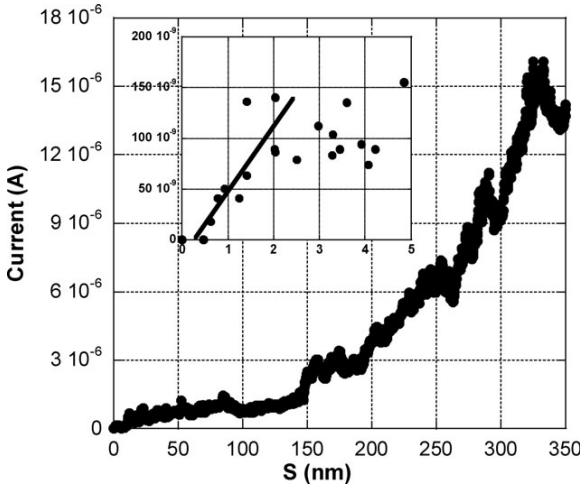

FIG. 5. Current versus depth for a typical indent into the CARC-coated Ni sample. The inset is a magnified view of the first 5 nm, where the initial increase in current is from the tunneling that occurs before the tip has penetrated the polymer and contacted the Ni.

plugged into *Eq. 5* and the junction distance can be evaluated.

$$\varepsilon(\omega) = \varepsilon_\infty + \sum_j \frac{\Delta\varepsilon_j}{1 + (i\omega\tau_j)^{\alpha_j}} + \frac{\sigma_{dc}}{i\omega\varepsilon_0}. \qquad (11)$$

RESULTS AND DISCUSSION

Conductive Nanoindentation for Barrier Height Determination

A typical current versus depth plot is shown is Fig. 5. For all the thin polymer samples, the initial jump in current represents the depth at which electrons from the conductive tip tunnel through the polymer. Subsequent variations in the current occur well after the indenter has completely passed through the polymer and into the nickel. Inset into Fig. 5 is a magnified view of the initial current jump, along with a linear fit for the data. The voltage is assumed to vary linearly over the approximately linear current region, allowing for calculation of G and graphing of $\ln(G)$ versus s to determine the slope m.

Table 3 gives the polymers tested in this way, along with the thickness values from ellipsometry and the calculated barrier heights. The polymer thickness does not directly affect the conductivity measurements, but using extremely thin films enables measurement of the barrier height before the polymer has time to mechanically deform. Mechanical deformation of the material would likely alter the shape of the current–depth curve and introduce a new source of error into the measurement. The films used were therefore as thin as possible, and in all cases were less than 30 nm thick.

TABLE 3. Polymers tested with conductive indentation.

Name	Thickness (nm)	Barrier height (eV)
Armorseal	9.9 ± 3.0	0.5 ± 0.2
CARC	22.7 ± 3.7	0.9 ± 0.7
CP1	8.7 ± 3.8	0.4 ± 0.2
Desothane® HS	10.5 ± 0.9	1.7 ± 0.9
Polycrylic®	26.1 ± 4.1	0.9 ± 0.5

We note that barrier height ranges for polymers often fall in the 0.1–1.9 eV range [42]. Although the Desothane sample has a slightly elevated barrier height, we feel that the values for all the polymers are sufficient for first order calculations. Subsequent experiments are underway to attempt to reduce the error (here, caused by variability between indents and sample size).

Dielectric Measurements and Junction Distance Calculations

The permittivity results obtained from the dielectric measurements can be seen in Fig. 6 with the accompanying fits for each polymer. The relaxation process that is observed at high frequencies is caused by the relaxation of charge carriers at the polymer/nanostrand interface due to field reversal. It is evident from Fig. 6 that the frequency and strength of the relaxation process is heavily dependent on the polymer showing that the adsorbed layer thickness is polymer dependent. The measured relaxation transition occurs at higher frequencies in the order of $\omega_{Syl} < \omega_{IRO} < \omega_{CARC} < \omega_{Des} < \omega_{Arm} < \omega_{CP1} < \omega_{Poly}$ (Table 4). It is noted that for the relaxation curves for Polycrylic, Armorseal, and CP1 (see Table 2) that the relaxation process is not as dramatic as the other polymers at the maximum frequency range of the measuring equipment. Regardless, the fitted line can be extrapolated to give the relaxation frequencies for these polymers using the Cole–Cole equation.

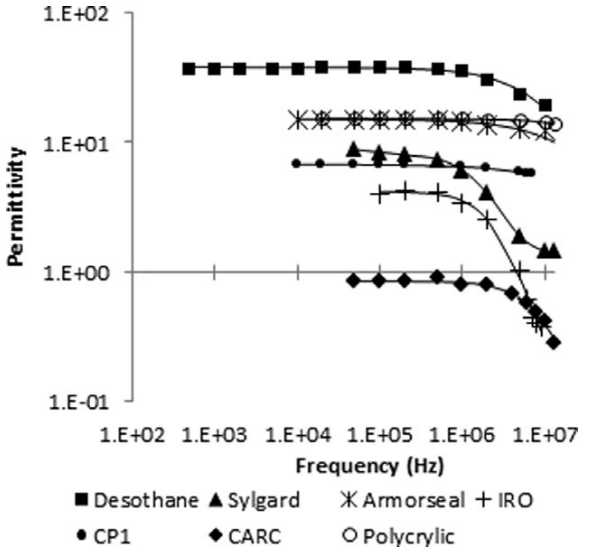

FIG. 6. Permittivity measurements (markers) with accompanying fits (solid lines) for various polymers filled with 15% volume fraction of Ni-Ns.

DOI 10.1002/pen

TABLE 4. Fitted parameter values and calculated barrier height and junction distance for various polymers.

Polymer	ω_c (MHz)	α	$\Delta\varepsilon$	λ (eV)	δ (nm)
Armorseal	25.6	0.7112	15.2	0.5	2.19
CARC	9.21	0.9336	0.8513	0.9	1.77
CP1	43.9	0.6733	6.774	0.4	2.35
Desothane	9.37	0.7456	38.17	1.7	1.31
Irogran	2.48	0.9763	4.18	—	—
Polycrylic	67.2	0.8846	15.26	0.9	1.56
Sylgard	1.83	0.7562	9.001	0.28	3.28

Application of Determined Parameters to Bulk Composite Resistivity

The main motivation behind finding the barrier height and typical junction distance in a polymer is to model the physical properties of a nanocomposite, and perhaps design better materials. In the case of the materials discussed in this article, the physical property of greatest concern is the bulk resistivity of a Ni-Ns-filled nanocomposite. *Equation 2* yields the tunneling resistivity at a single nanojunction, but not for the bulk nanocomposite. To relate the junction resistivity to bulk resistivity of the nanocomposite, it is assumed (for simplicity) that there is a linear relationship between the bulk resistivity and the nanojunction resistivity as defined in *Eq. 12*:

$$\rho_{\text{bulk}} = m\rho_{\text{junction}} \tag{12}$$

where the proportionality constant, m, does not depend on polymer type due to each sample having the same volume fraction of Ni-Ns homogenously mixed in each sample. The proportionality constant is assumed to be based on the number of conducting bonds in the nanocomposite as well as the overall geometry of the nanocircuitry.

The bulk resistivity of each nanocomposite was measured and compared to the calculated junction resistivity. A value of $m = 6.43 \times 10^{-4}$ was used to calculate the bulk resistivity from the junction resistivity which can be seen in Table 5. This was obtained by minimizing the difference between measured and calculated values in Table 5. Each calculated bulk resistivity is within an order of magnitude of the measured bulk resistivity. This suggests that with knowledge of the barrier height and the junction distance in a nanocomposite at a constant volume fraction of filler a rough estimate of the bulk resistivity of a nanocomposite can be determined.

TABLE 5. Calculated bulk resistivity from junction resistivity.

Polymer	Measured bulk resistivity (Ω·m)	Calculated bulk resistivity (Ω·m)	Junction resistivity (Ω·m)
Armorseal	0.4620	0.1493	232.3
CARC	0.4973	0.4243	660.0
CP1	0.9325	0.0882	137.2
Desothane	0.4530	0.4150	645.4
Polycrylic	0.6034	0.0551	85.7
Sylgard	0.9578	1.3564	2109.7

It is important to note that increasing calculated bulk resistivity does not correlate exactly to increasing measured bulk resistivity of the polymers—specifically for the cases of Polycrylic and CP1, for example This suggests although the linear relationship defined in *Eq. 12* does give a rough value for the bulk resistivity of the nanocomposites, its assumptions are not entirely correct. Future work will be needed to evaluate the number of nanojunctions and the nanocircuitry in these conductive nanocomposites to improve on the model.

CONCLUSIONS

Improved methods, based on newly developed functionality of nanoindenters, have been developed to calculate the barrier height of polymers using nanoindentation. The barrier height for various polymers using the improved nanoindentation method were calculated and used to determine the junction distance which yielded results in the 1–3 nm range, correlating well to previous research.

Dielectric spectroscopic methods used to calculate junction distance in typical conductive nanocomposites have been applied successfully to our Ni-Ns materials. This is the first report of junction distances in Ni-Ns. The junction distance can be used to determine the adsorbed layer thickness of polymers on Ni-Nss and inform design principles for future advanced Ni-Ns-based composites.

Measured barrier heights and the junction distances for the polymer samples enabled calculation of the resistivity of the Ni-Ns–polymer nanojunction. Using the nanojunction resistivity and a proportionality constant the resistivity of a bulk nanocomposite was determined and yielded reasonable results for the bulk resistivity of the analyzed polymers with widely different barrier height and junction gap properties. The less accurate results for two of the polymers (Polycrylic and CP1) suggest a different nanofiller circuitry resulting from the processing route, or some other missing factor in the framework. More work is required to establish relationships between polymers, solvents, processing routes, etc. and valid modeling assumptions; each processing variable potentially modifies the distribution of the Ni-Ns (the composite microstructure) in different ways.

With these options for measuring intrinsic material properties the tools are now in place for determining the physical constants necessary for informing a quantum tunneling/percolation model of conductive nanocomposites.

REFERENCES

1. E. Manias, *Nat. Mater.*, **6**, 9 (2007).
2. M.H. Al-Saleh and U. Sundararaj, *Carbon*, **47**, 2 (2009).
3. H.M. Ma and X.L. Gao, *Polymer*, **49**, 4230 (2008).
4. N. Grossiord, J. Loos, L. van Laake, M. Maugey, C. Zakri, C.E. Koning, and A.J. Hart, *Adv. Funct. Mater.*, **18**, 3226 (2008).

5. N. Li, Y. Huang, F. Du, X. He, X. Lin, H. Gao, Y. Ma, F. Li, Y. Chen, and P.C. Eklund, *Nano Lett*., **6**, 1141 (2006).
6. J.H. Lalli, R.O. Claus, A.B. Hill, J.B. Mecham, B.A. Davis, S. Subramanayan, and R.M. Goff, "Smart structures and materials 2005," in *SPIE*, V.W. Edward, Ed., 1 (2005).
7. O. Johnson, C. Gardner, D. Seegmiller, N. Mara, A. Dattelbaum, P. Rae, G. Kaschner, T. Mason, D. Fullwood, and G. Hansen, *Metall. Mater. Trans. A*, **42**, 3898 (2011).
8. J.-M. Park, D.-S. Kim, S.-J. Kim, P.-G. Kim, D.-J. Yoon, and K.L. DeVries, *Composites Part B*, **38**, 847 (2007).
9. J.-M. Park, P.-G. Kim, J.-H. Jang, Z. Wang, J.-W. Kim, W.-I. Lee, J.-G. Park, and K. Lawrence DeVries, *Composites Part B*, **39**, 1170 (2008).
10. N. Stübler, J. Fritzsche, and M. Klüppel, *Polym. Eng. Sci*., **51**, 1206 (2011).
11. T.M. Johnson, D.T. Fullwood, and G. Hansen, *Composites Part B.,* **43**, 1155 (2012).
12. O.K. Johnson, C.J. Gardner, D.T. Fullwood, B.L. Adams, G. Hansen, and N. Hansen, *Comput. Mater. Con*., **15**, 24 (2010).
13. N. Hansen and G. Hansen, *SAMPE J*., **47**, 6 (2011).
14. N. Hansen, D.O. Adams, and D.T. Fullwood, *J. Appl. Polym. Sci*., in review.
15. J.F. Zhou, Y.H. Song, Q. Zheng, Q. Wu, and M.Q. Zhang, *Carbon*, **46**, 679 (2008).
16. S. Radhakrishnan, *Mater. Lett*., **18**, 358 (1994).
17. M. Taya, W.J. Kim, and K. Ono, *Mech. Mater*., **28**, 53 (1998).
18. L. Bokobza, *Polymer*, **48**, 4907 (2007).
19. K. Li, X.L. Gao, J.C. Fielding, and T. Benson Tolle, *J. Comput. Theor. Nanosci*., **6**, 494 (2009).
20. E.P. Mamunya, V.V. Davidenko, and E.V. Lebedev, *Compos. Interfaces*, **4**, 169 (1996).
21. G. Grimmett, *Percolation*, 1 ed., Springer, New York (1989).
22. D. Stauffer and A. Aharony, *Introduction to Percolation Theory*, 2 ed., CRC Press, London (1994).
23. J. Fritzsche, H. Lorenz, and M. Klüppel, *Macromol. Mater. Eng*., **294**, 551 (2009).
24. V.M. Litvinov and P.A.M. Steeman, *Macromolecules*, **32**, 8476 (1999).
25. V.M. Litvinov, R.A. Orza, M. Klüppel, M. van Duin, and P.C.M.M. Magusin, *Macromolecules*, **44**, 4887 (2011).
26. M.T. Reetz, W. Helbig, S.A. Quaiser, U. Stimming, N. Breuer, and R. Vogel, *Science*, **267**, 367 (1995).
27. E. Tadd, A. Zeno, M. Zubris, N. Dan, and R. Tannenbaum, *Macromolecules*, **36**, 6497 (2003).
28. I. Pliskin and N. Tokita, *J. Appl. Polym. Sci*., **16**, 473 (1972).
29. M. Klüppel, *Adv. Polym. Sci*., **164**, 1 (2003).
30. J.G. Meier, J.W. Mani, and M. Klüppel, *Phys. Rev. B: Condens. Matter*, **75**, 054202 (2007).
31. D.H. Woo, E.M. Choi, Y.H. Yoon, K.J. Kim, I.C. Jeon, and H. Kang, *Surf. Sci*., **601**, 1554 (2007).
32. L. Nam-Suk, Q. Dong-Jin, S. Hoon-Kyu, and K. Young-Soo, *Nanotechnology Materials and Devices Conference, 2006*. NMDC 2006. IEEE, 570 (2006).
33. Y. Yamada, A. Sinsarp, M. Sasaki, and S. Yamamoto, *Jpn. J. Appl. Phys*., **42**, 4898 (2003).
34. N. Hansen, D.O. Adams, K.L. DeVries, A. Goff, and G. Hansen, *J. Adhes. Sci. Technol*., **25**, 2659 (2011).
35. J.D. Yeager, M. Dubey, M.J. Wolverton, M.S. Jablin, J. Majewski, D.F. Bahr, and D.E. Hooks, *Polymer*, **52**, 3762 (2011).
36. J.B. Theeten and D.E. Aspnes, *Annu. Rev. Mater. Sci*., **11**, 97 (1981).
37. O. Johnson, D. Seegmiller, D. Fullwood, A. Dattelbaum, N. Mara, G. Kaschner, T. Mason, and J.D. Yeager, *Society for the Advancement of Material and Process Engineering*, Long Beach, CA, 9 (2011).
38. H. Kawamoto, *Carbon Black—Polymer Composites, the Physics of Electrically Conducting Composites*, Marcel Dekker Inc, New York (1982).
39. K.-M. Jager, D.H. McQueen, I.A. Tchmutin, N.G. Ryvkina, and M. Klüppel, *J. Phys. D: Appl. Phys*., **34**, 8 (2001).
40. A.I. Medalia, *Rubber Chem. Technol*., **59**, 23 (1986).
41. K.S. Cole and R.H. Cole, *J. Chem. Phys*., **9**, 341 (1941).
42. Y. Yang, Q. Pei, and A.J. Heeger, *J. Appl. Phys*., **79**, 934 (1996).

DOI 10.1002/pen

Appendix C

T_1 Spin Lifetime Measurements

One of the Colton group's specialites is measuring spin lifetimes. Spin lifetime measurements (T_1) of a 14 nm (100) GaAs quantum well is described in the attached paper. My involvement in this experiment included instrument alignment, beam profile measurements, collecting spin lifetime data, and extrapolating the resulting decays for decay times.

Long-lived electron spins in a modulation doped (100) GaAs quantum well

J. S. Colton,[a] D. Meyer, K. Clark, D. Craft, J. Cutler, T. Park, and P. White
Department of Physics and Astronomy, Brigham Young University, Provo, Utah 84602, USA

(Received 20 July 2012; accepted 25 September 2012; published online 18 October 2012)

We have measured T_1 spin lifetimes of a 14 nm modulation-doped (100) GaAs quantum well using a time-resolved pump-probe Kerr rotation technique. The quantum well was selected by tuning the wavelength of the probe laser. T_1 lifetimes in excess of 1 μs were measured at 1.5 K and 5.5 T, exceeding the typical T_2^* lifetimes that have been measured in GaAs and II-VI quantum wells by orders of magnitude. We observed effects from nuclear polarization, which were largely removable by simultaneous nuclear magnetic resonance, along with two distinct lifetimes under some conditions that likely result from probing two differently localized subsets of electrons. © *2012 American Institute of Physics*. [http://dx.doi.org/10.1063/1.4759320]

I. INTRODUCTION

Since the initial proposal of spin-based quantum computing[1] and the discovery of very long inhomogeneous dephasing spin lifetimes (T_2^*) in GaAs,[2] a tremendous amount of research effort has been put forth to better understand the interaction of electronic spin states ("spins") with each other and with their environment, and to create structures on the nanoscale that allow for better control and study of the spins.[3] Among the key requirements for semiconductor spintronic devices is an understanding of the spin dephasing mechanisms in semiconductors.[4] Optical techniques for interacting with spins in semiconductor heterostructures are powerful tools for the initialization, manipulation, and study of spin dynamics.[5] GaAs/AlGaAs heterostructures are ideally suited for such experiments, as GaAs is a direct-gap semiconductor with well-known selection rules connecting optical polarization to the spin degree of freedom. Additionally, the band-gaps of GaAs/AlGaAs heterostructures readily match commercially available lasers such as Ti:sapphire, which allows for resonant excitation and detection of the electronic spins.

Many experimental studies on GaAs have focused on lightly doped *n*-type bulk material, where electrons localize on donor sites at low temperature. Spin lifetimes much longer than the optical lifetimes can be obtained with these doped electrons. A wide variety of experimental techniques have been employed to study this type of bulk material, including (but not limited to) Hanle effect depolarization,[6] time-resolved Faraday or Kerr rotation (TRFR),[2,7] optically detected electron spin resonance,[8,9] time-resolved decay of photoluminescence polarization[10,11] or polarization-dependent luminescence,[12] optically controlled spin echo,[13] Kerr rotation imaging,[14,15] and spin noise spectroscopy.[16] Other experimental studies have focused on InAs or InGaAs quantum dots embedded in a GaAs barrier, again with doped electrons added to the dots to allow the electron spin information to be preserved beyond the radiative recombination time. In self-assembled quantum dots, for example, optical techniques have allowed the electron spins to be precisely controlled on time scales of micro- or milliseconds.[17–20]

Bridging the gap between bulk material and 0D quantum dots, 2D systems can serve as well-defined model systems for studies in spin dynamics. Early studies of spins in quantum wells often focused on exciton dynamics.[21] However, time-resolved studies have also served to shed light on properties of the electrons in GaAs quantum wells, allowing the dephasing of spins in subnanosecond[22] and nanosecond[23,24] time scales to be directly measured. The longest spin dephasing times in GaAs quantum wells have ranged from 10 to 30 ns.[24,25] Other promising results have been obtained in II-VI quantum wells, where spin dephasing times of 30 ns have also been observed through various techniques[26,27] and some degree of optical control of spins has been established.[28]

Throughout these previous experiments, the spin lifetimes in quantum wells that have been the focus of research have nearly always been the T_2^* lifetimes, also called the inhomogeneous dephasing times. By contrast, in this paper, we present experimental measurements of T_1 spin lifetimes, also known as spin flip times. While T_2^* is measured with the field perpendicular to the spin orientation, T_1 is measured with a parallel field. T_2^* and T_1 are generally considered lower and upper bounds for T_2, the true dephasing time.

In this work, we have measured the T_1 spin lifetime of a 14 nm GaAs quantum well using a time-resolved pump-probe Kerr rotation technique. The spin lifetimes were quite long—10 and 100 ns at most fields (from 0 to 7 T) and temperatures (1.5 and 5 K), and exceeding 1 μs at the lowest temperature and highest field. This paper is structured as follows: Sec. II describes the sample. Section III discusses the polarization and detection scheme, along with some wavelength-dependent results. Section IV gives details on our experimental setup for spin lifetime measurements. The main experimental results and discussion are found in Sec. V, after which we provide some discussion in Sec. VI. We conclude in Sec. VII.

II. SAMPLE

We studied a 14 nm wide GaAs quantum well which was grown through molecular beam epitaxy and modulation

[a]Author to whom correspondence should be addressed. Electronic mail: john_colton@byu.edu.

doped with silicon donors to produce a carrier concentration of $n = 3 \times 10^{10}\,\mathrm{cm}^{-2}$ in the well. It is part of a multi-quantum well sample containing five total wells with thicknesses of 2.8, 4.2, 6.2, 8.4, and 14 nm. More details on the sample's structure and electronic properties can be found in Ref. 29. The 14 nm well was selected by tuning our laser to the optical transition of that well, approximately 807 nm. As with experiments in other *n*-type bulk, quantum dot, and quantum well samples mentioned in the Introduction, the doping allows spin information to be preserved through the ground state electrons.

This particular well of this particular sample has been the study of other spin-related investigations by our group and others, including Hanle effect measurements of T_2^*,[30] time resolved Kerr rotation measurements to study optical initialization and T_2^* lifetimes,[23] and optically detected electron spin resonance measurements which manipulated spin states with microwaves.[31]

III. SPIN POLARIZATION AND DETECTION

The modulation doping causes a background of electrons to exist in the well, which can interact with optically injected excitons to form trion states. We consider only the lowest energy, singlet trions, where two electrons of opposite spin form a bound state with a hole which can be either spin-up or spin-down. The hole spin can be either $\pm 3/2$ or $\pm 1/2$, depending on whether it is a heavy or light hole. Because the two electrons in the singlet state have opposite spins, the overall spin of the trion follows the hole spin and is either $\pm 3/2$ or $\pm 1/2$. The details of trion formation rely critically on whether the optical photon has spin $+1$ (labeled σ^+) or spin -1 (labeled σ^-), and are depicted in Fig. 1.

The polarization of the ground state electron spins in doped quantum wells has typically been done through resonant excitation of a trion state.[23,32,33] That mechanism relies on fast hole relaxation in the excited state: with σ^+ photons (for example) resonant with the heavy hole trion transition, electrons are taken out of the $+1/2$ state into the $+3/2$ heavy hole trion. The rapid hole relaxation causes the trion population to be equalized between the $+3/2$ and $-3/2$ states. In GaAs, this can occur extremely rapidly, even when compared to the ~50 ps optical lifetime.[23] The $+3/2$ trions decay into the $+1/2$ ground state; the $-3/2$ trions decay into the $-1/2$ ground state. The net result is a transfer of spin population out of the $+1/2$ into the $-1/2$ ground state, and a ground state spin polarization occurs. (If there were no hole spin flips, the $+3/2$ trion would simply decay back into the $+1/2$ ground state and no ground state spin polarization would accumulate.)

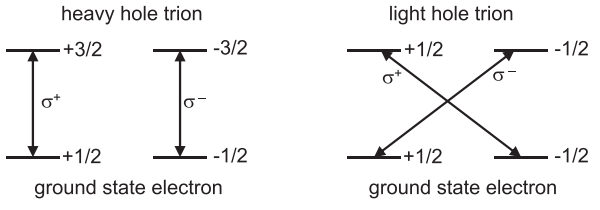

FIG. 1. Heavy and light hole trion transitions and selection rules. The trion forms when a ground state electron ($+1/2$ or $-1/2$) combines with an optically injected electron hole pair. Because the two electrons are in a singlet state, the spin state of the trion matches the spin state of the hole ($+3/2$ or $-3/2$ for the heavy hole trion; $+1/2$ or $-1/2$ for the light hole trion). Photon spin states of $+1$ and -1 are indicated by σ^+ and σ^-, respectively.

Our approach was slightly different. We performed a two-color experiment with pump and probe photons having different energies. Although our probe laser was resonant with a trion transition (details below), our pump laser (781 nm) was at a much higher energy. Our pump laser, therefore, excited both heavy and light hole trions simultaneously. Again considering σ^+ photons: they will excite heavy hole trions and pump spins out of the $+1/2$ ground state as described in the previous paragraph; however, they will also pump spins out of the $-1/2$ ground state by exciting light hole trions. As in the case of *n*-type bulk material—where the heavy and light hole states are degenerate at the band edge and are thus always excited simultaneously with a pump laser—we rely on unequal transition probabilities for the heavy hole state compared to the light hole state to generate a net spin polarization for the ground state electrons. Two-color experiments have been done in II-VI quantum wells in order to separate the effects of detecting the exciton vs. trion transitions[27,33,34] and have been proposed for use in a non-resonant pumping scheme such as we employed,[34] but we are not familiar with any other actual two-color experiments in GaAs quantum wells.

To detect the persisting electron spin polarization, we tune the probe laser to be resonant with the trion transitions. This is quite similar to those groups cited above who employed a single-color resonant pump-probe scheme. We use the Kerr effect, i.e., the rotation of the angle of polarization of our linearly polarized probe beam, to detect the ground state spin population. Under typical conditions when the probe laser is tuned resonant with the quantum well's

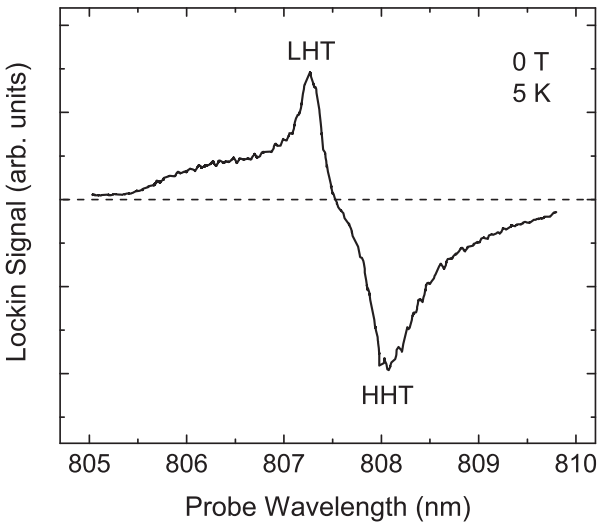

FIG. 2. Kerr rotation signal taken at 0 T, 5 K, as a function of probe laser wavelength. Data were obtained with pump and probe pulses each set for 50% duty cycle and overlapping each other in time. The dashed line indicates the zero position; the two peaks have opposite sign due to the optical selection rules. LHT and HHT label the light and heavy hole trion peaks, respectively.

optical transition, there is a clear signal with two features (see Fig. 2). The feature at 807.3 nm is from the light hole trion; the one at 808.1 nm is from the heavy hole trion. (As noted by Kennedy *et al.*, the heavy hole *exciton* transition likely partially overlaps the light hole trion.[23]) The peaks are opposite in sign because of the opposite selection rules depicted in Fig. 1.

In principle, the ground state electron spin polarization should be able to be measured through either the heavy hole or light hole trion transitions; in practice, it proved easier for us to set our probe laser to the light hole trion transition because at some fields the heavy hole trion feature was difficult to observe (see Fig. 3(a) for a collection of wavelength-dependent data at various fields). The peak positions of Fig. 3(a) are summarized in Fig. 3(b). The peak positions of the heavy and light hole trions as a function of magnetic field follow the well-known quadratic "diamagnetic shift," in this case given by the following equations fitted from the data with energies in eV and fields in T:

$$E_{LHT} = 1.5360 + 4.289 \times 10^{-5} B^2, \quad (1a)$$

$$E_{HHT} = 1.5344 + 4.289 \times 10^{-5} B^2. \quad (1b)$$

The two trion peaks maintain a constant separation of 1.57 meV which is in good agreement for the LHT-HHT separation reported in Ref. 23.

IV. EXPERIMENTAL SETUP

To study the T_1 behavior of the ground state electron spins, we used a two-color pump-probe technique described in detail in Ref. 7. The magnetic field is oriented in Faraday (longitudinal) geometry, with the field parallel to the spin alignment. As mentioned in Sec. III, the spins are aligned using a circularly polarized pump laser and detected via the Kerr rotation of a linearly polarized probe laser. Both pump and probe lasers are pulsed, and the delay between the two of them is varied. This is similar to the traditional TRFR technique used by many to measure the inhomogeneous dephasing lifetime, T_2^*, of various semiconductors. However, in order to access the much longer lifetimes that are involved with T_1 as opposed to T_2^*, we employed electronic gating of pump and probe pulses instead of a mechanical delay line to vary the delay. Also, because the spins are parallel to the external field, we do not see the precession oscillations that are a hallmark of the traditional TRFR technique.

The pulses in the probe beam, a tunable cw Ti:sapphire laser, were produced with an acousto-optic modulator (AOM). Because the probe beam was quasi-cw—only pulsing on the time scales of 10 ns in response to our AOM—its bandwidth is essentially infinitely narrow on the scales of Figs. 2 and 3 and excellent wavelength resolution was achieved. The pump beam, a fast diode laser, was modulated on/off via a direct modulation input. The two beams were synchronously controlled with a two-channel pulse generator. To separate out the spin effects from sources of noise and to reduce dynamic nuclear polarization, we modulated the helicity of the pump laser from σ^+ to σ^- with a 42 kHz photo-elastic modulator and detected the signal with a lockin amplifier referenced to that frequency. The lockin signal is proportional to the spin polarization of the electrons in the sample.

The pump beam was set to 25 mW unpulsed and was focused (partially) to a diameter of 0.22 mm. The probe beam was set to a diameter of 0.21 mm, and its power was either 3.5 mW unpulsed (for the 5 K data) or 2 mW unpulsed (for the 1.5 K data). The overall time for a given pulse repetition cycle was chosen to be much *longer* than the decay time (by at least a factor of five or six) so that complete decays could be observed, and pulse widths were set to be much *shorter* than the decay time so that the measured decays were not substantially affected by the finite size of the probe pulse width. Duty cycles of 4% for the pump and 2% for the probe were common.

The sample was placed in a superconducting electromagnet with integrated cryostat where fields up to 7 T and temperatures down to 1.5 K could be investigated.

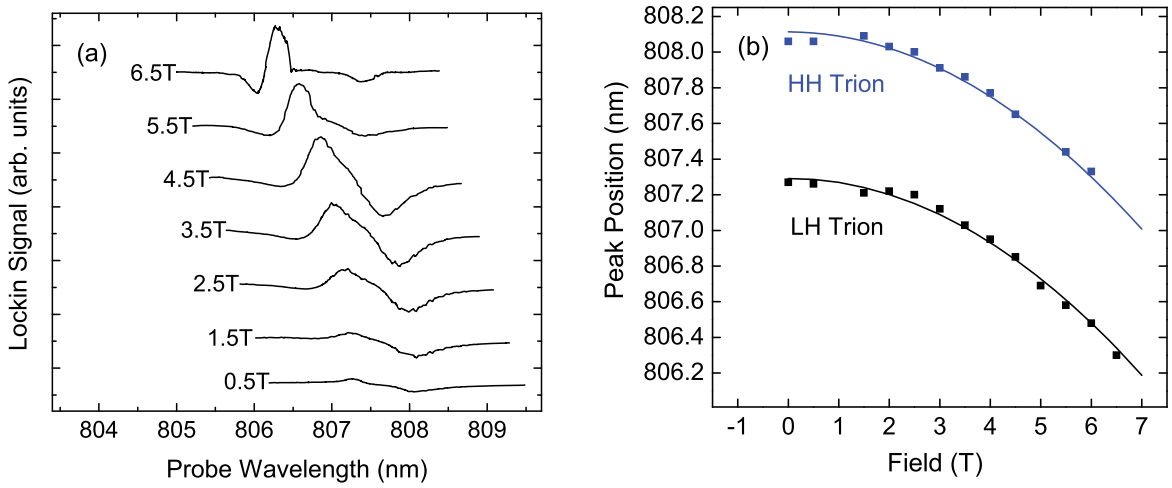

FIG. 3. (a) cw Kerr rotation signal vs. probe laser wavelength at 5 K for selected fields. Data were obtained under the same conditions as Fig. 2. (b) Summary of peak positions, fitted to a quadratic function in energy.

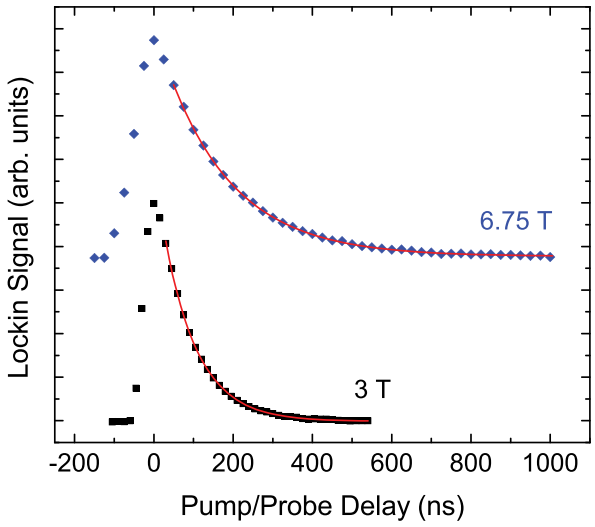

FIG. 4. Representative 5 K data taken at 3 T and 6.75 T: spin polarization vs. delay between pump and probe pulses. The raw data for the spin decays (points) was fitted to exponential decays (solid curves), yielding spin lifetimes of 84.5 ns and 169 ns for the 3 T and 6.75 T data, respectively. The 6.75 T data has been shifted vertically for clarity.

V. RESULTS

For a given set of experimental parameters, the delay between pump and probe was varied in order to trace out the decay of spin polarization. As the delay is varied, the probe pulse temporally "enters" the pump pulse, causing the lock-in signal to rapidly rise, then "exits" the pump pulse causing a decrease in signal. Any signal which exists after the probe pulse has exited the pump pulse is a result of persisting spin information. The polarization typically decays exponentially as

$$P = P_0 \exp(-t/T_1). \tag{2}$$

Fig. 4 shows two representative decays and their fits, which in this case yielded spin lifetimes of 84.5 ns and 169 ns for the 3 T and 6.75 T data, respectively. The specific pulse widths used for these decays were 42 ns (pump) and 30 ns (probe) for the 3 T data, and 42 ns (pump) and 30 ns (probe) for the 6.75 T data. The fits were performed using only data from after the probe pulse had temporally left the pump pulse.

Figure 5 displays a summary of our spin lifetime results for spin decays measured at both 5 K and 1.5 K. Spin lifetimes from 44 ns to 170 ns were measured at 5 K, and lifetimes from 44 ns to 1040 ns were measured at 1.5 K. These lifetimes far exceed the T_2^* value of 2.5 ns reported by Kennedy *et al.* for this particular quantum well (at 0 T, 6 K),[23] and are also much longer than the longest lifetimes (also T_2^*) of ~30 ns reported for *any* quantum wells of which we are aware, as referenced in the Introduction. T_1 is generally considered an upper bound for the true coherence time T_2, and in (100) quantum wells, T_2 is expected to be on the same order of magnitude as T_1.[41] Therefore, these long T_1 results may be an indication that spin coherence can persist in quantum wells much longer than has generally been considered to be the case, and that spin echo experiments should be pursued in quantum well samples.

Nearly all of the raw data followed precise exponential decays like the two representative plots in Fig. 4. However, at 1.5 K there were some field points which did not follow a simple exponential decay. For those points, the lifetime that is plotted is simply the $1/e$ fall-off point for the raw data after the peak.

One reason for non-exponential decays is the presence of a nuclear spin polarization. Dynamic nuclear polarization is expected to occur whenever the electron spin polarization is far from thermal equilibrium. This is especially the case for us for the high field, low temperature situations. From simple Boltzmann statistics, the polarization of a two level spin system is

$$P = \tanh(g\mu_B B/2k_B T). \tag{3}$$

The g-factor for this well was obtained in previous spin resonance experiments,[31] $|g| = 0.346$, so at 1.5 K the thermal equilibrium polarization of the electrons will be 30%, 37%,

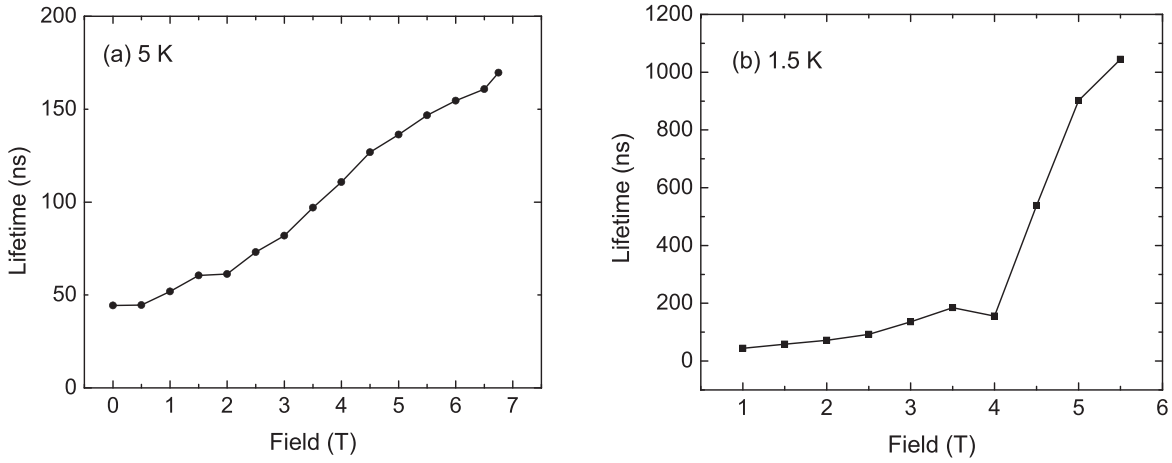

FIG. 5. Measured electron spin lifetimes as a function of magnetic field for (a) 5 K and (b) 1.5 K. For the 1.5 K data, the scans for fields at 4 T and above were done with rf applied to remove nuclear polarization (which may have caused some heating of the sample).

and 43% for fields of 4, 5, and 6 T, respectively. However, the pump laser—with its helicity modulated between σ^+ and σ^- as described above—will be driving the electron polarization towards 0%, at least on time scales long compared to the modulation time of $(42\,\text{kHz})^{-1}$. As the electrons are driven toward zero polarization, they will attempt to return to their thermal equilibrium value by interacting with the nuclear spin bath via the hyperfine interaction. This will polarize the nuclear spins to some degree.[35] Polarized nuclei impact the electrons via the Overhauser effect and generate an effective field for the electrons. This effective field can vary both physically across our laser beams, as well as temporally during our scans, and can change the measured spin response in unpredictable ways.

That there is substantial nuclear spin polarization present in the material under some conditions was evident. Fig. 6 displays two spin decays taken at 5.5 T and 1.5 K, under nearly identical conditions. The only difference is that the solid curve was performed while rf was applied to a Helmholtz coil surrounding the sample, sweeping through the frequencies needed for nuclear magnetic resonance (NMR) of the four nuclear isotopes present in the quantum well and barrier: ^{75}As, ^{69}Ga, ^{71}Ga, and ^{27}Al. This was done via a function generator with customizable frequency modulation. With rf applied to remove built-up nuclear polarization, a relatively normal decay was observed. However, without rf the shape was both non-exponential and non-reproducible. As can be seen, for the data presented in Fig. 6, the spin polarization initially remained *constant* as the probe pulse begins to arrive after the pump. Something is changing inside the sample (i.e., the nuclear spins) in order to preserve the electron spin polarization! This is very reminiscent of the "spin dragging" effect that has been observed in electron spin resonance of bulk GaAs[36] and GaAs-based quantum dots,[37] where nuclear polarization has also been seen to adjust to keep the electronic polarization constant. These nuclear polarization effects were seen for all of the 1.5 K data at fields of 4 T and higher, but not for fields below 4 T, nor for any of the 5 K data. The lifetimes plotted in Fig. 5(b) for these fields are for the "rf on" set of measurements. Although the decays for these points looked reasonable, as in the rf on curve of Fig. 5(b), they could not be fitted to simple exponential decays—indicating that our removal of the effects from nuclear polarization was incomplete. The rf likely also caused some small heating of the sample, which could explain the unexpected decrease in lifetime in Fig. 5(b) going from 3.5 T (no rf) to 4 T (with rf).

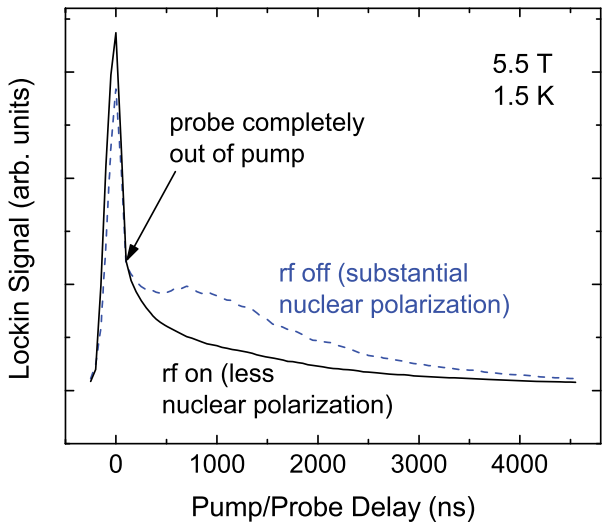

FIG. 6. Spin decays measured at 5.5 T and 1.5 K. The solid and dashed lines are for conditions with and without rf applied to depolarize the nuclear spins.

VI. DISCUSSION

To discuss our spin relaxation results further, we first review some of the theoretical work on spin lifetimes in quantum wells. Spin scattering in quantum wells was first discussed by D'yakonov and Kachorovskii (DK).[38] In GaAs-based quantum wells, the lack of bulk inversion symmetry leads to spin-splitting of the conduction band. This spin splitting can be regarded as an internal magnetic field, about which electrons precess between momentum scattering events. This leads to information loss about the initial spin state and is called the D'yakonov-Perel mechanism. D'yakonov and Kachorovskii analyzed that mechanism in the context of quantum wells to obtain this result for the spin lifetime

$$\tau_s = \frac{E_g \hbar^2}{\alpha^2 E_1^2 k_B T} \frac{1}{\tau_v}, \tag{4}$$

where $E_g =$ is the band gap energy, E_1 is the electron's quantized energy in the well, T is the temperature, τ_v is the momentum scattering time (which also depends on temperature), and α is a parameter related to the spin splitting of the conduction band. An important result is that generally speaking a short momentum scattering time (τ_v) will result in a long spin lifetime (τ_s), and vice versa. In asymmetric quantum wells, there is additionally a structural inversion asymmetry, which can add to or subtract from the effects of the bulk inversion asymmetry. This has recently been used in an experiment by Balocchi *et al.* to partially cancel the relaxation term from bulk inversion asymmetry (Dresselhaus) with the term from structural inversion asymmetry (Rashba).[24]

The general theoretical approach is, therefore, often to model the momentum-scattering mechanisms that contribute to τ_v; for example, Bastard and Ferreira used the DK theory to describe ionized impurity scattering, often the most efficient scatterers at low T.[39] They found that τ_v shortens considerably at low temperatures due to inefficient screening, yielding spin flip times that are the longest for wide wells and low temperatures. For their particular impurity concentration and screening model, they predicted τ_s to be 2.5 ns at 10 K for a 15 nm GaAs/AlGaAs well, and their data points suggest that τ_s should increase rapidly with a decreasing temperature. A simple extrapolation of their data suggests a factor of 10 or 100 increase in lifetime as temperature decreases to 1.5 K. Bastard extended the DK theory to a high magnetic field situation using Landau levels and a point-like defect model for the scatterers, to obtain a prediction of 1-2 ns for a

9 nm well for fields between 6 and 15 T and a $B^{1/2}$ dependence of lifetime on field.[40]

Experimentally, Terauchi *et al.* measured spin lifetimes at 0 T and 300 K in a series of 7.5 nm multi-quantum well samples and verified the $\tau_s \sim 1/\tau_v$ prediction of the DK theory, although the spin lifetimes were about an order of magnitude higher than the theory predicted.[41] Lau *et al.* built upon the DK theory in two papers, using a 14 band **k·p** model to describe bulk[42] and structural inversion asymmetry,[43] and overcame the order of magnitude discrepancy that had been seen. T_1 and T_2 were predicted to be the same order of magnitude, with T_2 ranging from $2T_1/3$ to $2T_1$ in (100) wells depending on the value of α. Their calculated T_1 values matched the room temperature experiments of Terauchi *et al.*,[41] and the T_2 values matched the original experiments of Kikkawa and Awschalom[2] for temperatures of 100 K and above. They issued the disclaimer, however, that their theory might not be applicable at lower temperatures.

More recent theory on spin relaxation in *n*-doped quantum wells is sparse, the work of Harmon *et al.* being a notable exception.[44] Their work focuses on spin dephasing from the hyperfine interaction, applicable to T_2^* but not to T_1. They also explicitly account for doping via donors inside the well, and mention that their theory is consequently not applicable for modulation doped wells (such as used in our experiment).

Considering our measured value of 44 ns for T_1 at 0 T and 5 K, our results seem fairly solidly in the Bastard and Ferriera regime (if the low temperature extrapolation of their data is to be believed), and likely indicate that ionized impurity scattering within the DK model is our primary relaxation mechanism. Our quantum well is modulation doped, so there are no *intentional* impurities in the well, but this sample did have a slight *n*-type background. Our spin lifetime increase with magnetic field did not exactly follow the $B^{1/2}$ prediction of Bastard, but our lifetimes did increase nearly monotonically with field as Bastard's theory predicts. Comparing our results to other experimental results, one would expect our 0 T, 5 K value for T_1 to match fairly closely the 0 T, 6 K value for T_2^* of Kennedy *et al.*,[23] since the sample is the same and T_2^* and T_1 are equivalent in the absence of a magnetic field. However, the value of Kennedy *et al.* seems to have been obtained from a fit of a decay measured only between 0 and 1.5 ns, and consequently, their value of 2.5 ns may not be completely trustworthy.

Finally, in two previous papers on T_2^* lifetimes in II-VI quantum wells, two distinct spin lifetimes were seen for a given temperature and field.[27,34] In each case, the difference arose when detecting the spin of the electrons through the trion transition vs. through the exciton transition: a factor of 6 difference in lifetime for Ref. 27 and a factor of 2 for Ref. 34. Each group attributed the difference in lifetimes to a difference in localization of the subset of electrons being probed: localized electrons in the case of the trion transition and quasi-free electrons in the case of the exciton transition. The trion and exciton transitions are clearly resolvable in II-VI quantum wells, but in our GaAs quantum well, the light hole trion transition and heavy hole exciton were likely both contained in the "light hole trion region" marked in Fig. 2 (which is where we probed). Nevertheless, we may have seen this effect in our T_1 measurements as well. Fig. 7 displays the results of a fine-scale wavelength adjustment: measuring the spin lifetimes as we varied the probe laser across the light hole trion peak. The trion peak from the non-time-resolved wavelength-dependent Kerr rotation signal (as in Fig. 2) is shown as a dashed line. As the wavelength was tuned from one side of the peak to the other, there was an abrupt shift in spin lifetime. It seems likely that this shift in lifetime is a result of probing different subsets of electrons (e.g., localized vs. quasi-free), just as was seen in the II-VI quantum well experiments. The presence of localized electrons also helps explain why the dynamic nuclear polarization effects described above could be so pronounced, when delocalized electrons alone would not typically polarize the nuclei very much.

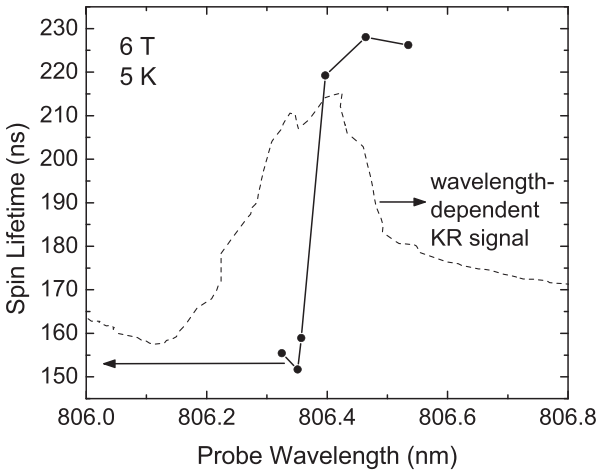

FIG. 7. Spin lifetimes as a function of probe laser wavelength, for 6 T and 5 K. Note the abrupt shift in lifetime over a very small wavelength range. For reference, the wavelength-dependent Kerr rotation for these conditions, showing the light hole trion peak, is also displayed (dashed line).

VII. CONCLUSION

In conclusion, we have measured T_1 spin flip times in a GaAs quantum well by tuning a probe laser to be resonant with the optical transition of the well in a longitudinal (Faraday) geometry. The well had extremely long spin lifetimes, exceeding 1 μs for 1.5 K and 5.5 T. This quite likely indicates long T_2 lifetimes as well. Lifetimes increase with field and decrease with temperature. Nuclear polarization effects were significant at the highest fields at 1.5 K, but could largely be removed with nuclear magnetic resonance. Different lifetimes were observed with small changes in wavelength for one set of experimental conditions, likely indicating responses from two differently localized subsets of electrons.

ACKNOWLEDGMENTS

The authors acknowledge partial funding from the NASA EPSCOR program.

[1]D. Loss and D. P. DiVincenzo, Phys. Rev. A **57**, 120 (1998).
[2]J. M. Kikkawa and D. D. Awschalom, Phys. Rev. Lett. **80**, 4313 (1998).

[3]See M. W. Wu, J. H. Jiang, and M. Q. Weng, Phys. Rep. **493**, 61 (2010) for a recent and extensive review article on the topic.
[4]*Spin Physics in Semiconductors*, edited by M. I. Dyakonov (Springer, Berlin, 2008).
[5]*Optical Orientation*, edited by F. Meier and B. P. Zakharchenya (North-Holland, Amsterdam, 1984).
[6]R. I. Dzhioev, K. V. Kavokin, V. L. Korenev, M. V. Lazarev, B. Ya. Meltser, M. N. Stepanova, B. P. Zakharchenya, D. Gammon, and D. S. Katzer, Phys. Rev. B **66**, 245204 (2002).
[7]J. S. Colton, K. Clark, D. Meyer, T. Park, D. Smith, and S. Thalman, Solid State Commun. **152**, 410 (2012).
[8]J. S. Colton, T. A. Kennedy, A. S. Bracker, D. Gammon, and J. B. Miller, Phys. Rev. B **67**, 165315 (2003).
[9]J. S. Colton, T. A. Kennedy, A. S. Bracker, D. Gammon, and J. Miller, Solid State Commun. **132**, 613 (2004).
[10]J. S. Colton, T. A. Kennedy, A. S. Bracker, and D. Gammon, Phys. Rev. B **69**, 121307(R) (2004).
[11]J. S. Colton, M. E. Heeb, P. Schroeder, A. Stokes, L. R. Wienkes, and A. S. Bracker, Phys. Rev. B **75**, 205201 (2007).
[12]K.-M. Fu, W. Yeo, S. Clark, C. Santori, C. Stanley, M. C. Holland, and Y. Yamamoto, Phys. Rev. B **74**, 121304(R) (2006).
[13]S. M. Clark, K.-M. Fu, Q. Zhang, T. D. Ladd, C. Stanley, and Y. Yamamoto, Phys. Rev. Lett. **102**, 247601 (2009).
[14]J. M. Kikkawa and D. D. Awschalom, Nature **397**, 139 (1999).
[15]S. A. Crooker and D. L. Smith, Phys. Rev. Lett. **94**, 236601 (2005).
[16]S. A. Crooker, L. Cheng, and D. L. Smith, Phys. Rev. B **79**, 035208 (2009).
[17]M. Kroutvar, Y. Ducommun, D. Heiss, M. Bichler, D. Schuh, G. Abstreiter, and J. F. Finley, Nature **432**, 81 (2004).
[18]A. Greilich, D. R. Yakovlev, A. Shabaev, Al. L. Efros, I. A. Yugova, R. Oulton, V. Stavarache, D. Reuter, A. Wieck, and M. Bayer, Science **313**, 341 (2006).
[19]A. Greilich, A. Shabaev, D. R. Yakovlev, Al. L. Efros, I. A. Yugova, D. Reuter, A. D. Wieck, and M. Bayer, Science **317**, 1896 (2007).
[20]D. Press, K. De Greve, P. L. McMahon, T. D. Ladd, B. Friess, C. Schneider, M. Jamp, S. Höfling, A. Forchel, and Y. Yamamoto, Nature Photon. **4**, 367 (2010).
[21]See Chapter 3 of Reference 4 for a review: T. Amand and X. Marie, Exciton Spin Dynamics in Semiconductor Quantum Wells.
[22]A. Malinowski and R. T. Harley, Phys. Rev. B **62**, 2051 (2000).
[23]T. A. Kennedy, A. Shabaev, M. Scheibner, A. L. Efros, A. S. Bracker, and D. Gammon, Phys. Rev. B **73**, 045307 (2006).
[24]A. Balocchi, Q. H. Duong, P. Renucci, B. L. Liu, C. Fontaine, T. Amand, D. Lagarde, and X. Marie, Phys. Rev. Lett. **107**, 136604 (2011).
[25]R. I. Dzhioev, V. L. Korenev, B. P. Zakharchenya, D. Gammon, A. S. Bracker, J. G. Tischler, and D. S. Katzer, Phys. Rev. B **66**, 153409 (2002).
[26]E. A. Zhukov, D. R. Yakovlev, M. Bayer, G. Karczewski, T. Wojtowicz, and J. Kossut, Phys. Status Solidi B **243**, 878 (2006).
[27]H. Hoffmann, G. V. Astakhov, T. Kiessling, W. Ossau, G. Karczewski, T. Wojtowicz, J. Kossut, and L. W. Molenkamp, Phys. Rev. B **74**, 073407 (2006).
[28]E. A. Zhukov, D. R. Yakovlev, M. M. Glazov, L. Fokina, G. Karczewski, T. Wojtowicz, J. Kossut, and M. Bayer, Phys. Rev. B **81**, 235320 (2010).
[29]J. G. Tischler, A. S. Bracker, D. Gammon, and D. Park, Phys. Rev. B **66**, 081310(R) (2002).
[30]R. I. Dzhioev, V. L. Korenev, I. A. Merkulov, B. P. Zakharchenya, D. Gammon, Al. L. Efros, and D. S. Katzer, Phys. Rev. Lett. **88**, 256801 (2002).
[31]B. Heaton, J. S. Colton, D. N. Jenson, M. J. Johnson, and A. S. Bracker, Solid State Commun. **150**, 244 (2010).
[32]W. Ungier and R. Buczko, J. Phys.: Condens. Matter **21**, 045802 (2009).
[33]Z. Chen, S. G. Carter, R. Bratschitsch, and S. T. Cundiff, Physica E **42**, 1803 (2010).
[34]E. A. Zhukov, D. R. Yakovlev, M. Bayer, M. M. Glazov, E. L. Ivchenko, G. Karczewski, T. Wojtowicz, and J. Kossut, Phys. Rev. B **76**, 205310 (2007).
[35]The presence of dynamic nuclear polarization even while using a σ^+/σ^--modulated pump laser has been seen previously by our group and others, the first reference to such perhaps being C. Weisbuch and C. Hermann, Phys. Rev. B **15**, 816 (1977).
[36]T. A. Kennedy, J. Whitaker, A. Shabaev, A. S. Bracker, and D. Gammon, Phys. Rev. B **74**, 161201R (2006).
[37]I. T. Vink, K. C. Nowack, F. H. L. Koppens, J. Danon, Y. V. Nazarov, and L. M. K. Vandersypen, Nat. Phys. **5**, 764 (2009).
[38]M. I. D'yakonov and V. Yu. Kachorovskii, Sov. Phys. Semicond. **20**, 110 (1986).
[39]G. Bastard and R. Ferreira, Surf. Sci. **267**, 335 (1992).
[40]G. Bastard, Phys. Rev. B **46**, 4253 (1992).
[41]R. Terauchi, Y. Ohno, T. Adachi, A. Sato, F. Matsukura, A. Tackeuchi, and H. Ohno, Jpn. J. Appl. Phys. **38**, 2549 (1999).
[42]W. H. Lau, J. T. Olesberg, and M. E. Flatte, Phys. Rev. B **64**, 161301 (2001).
[43]W. H. Lau and M. E. Flatte, J. Appl. Phys. **91**, 8682 (2002).
[44]N. J. Harmon, W. O. Putikka, and R. Joynt, Phys. Rev. B **81**, 085320 (2010).

Appendix D

Critical annealing temperature for optical properties of InGaAs quantum nanostructures

Chapter 3 summarizes the contents of the attached paper. My involvement in this portion of the experiments includes assisting with collecting the photoluminescence (PL) data. Notable results from this paper include that there is a critical annealing temperature, at which the quantum dots electronically resemble dots grown with the conventional method. The photoluminescence study shows some results from our temperature-dependance experiments and compares the PL peak widths of the three samples studied.

Critical annealing temperature for optical properties of InGaAs quantum nanostructures

Haeyeon Yang,*[1] Dong-Jun Kim,[1] John Colton,[2] Tyler Park,[2] David Meyer,[2] Aaron M. Jones,[2] Scott Thalman,[2] Dallas Smith,[2] Ken Clark,[2] and Steve Brown[2]

1. Department of Nanoscience and Nanoengineering, South Dakota School of Mines and Technology, Rapid City, SD 57701
2. Department of Physics and Astronomy, Brigham Young University, Provo, UT 84602

* To whom the correspondence should be addressed, e-mail: haeyeon.yang@sdsmt.edu

Abstract

We report optical properties of a single stack of quantum dot (QD) chains along with their structural characterizations. The self-assembly of QD-chains isinduced by annealing strained-but-flat InGaAs epilayers that are grown at a temperature lower than the conventional Stranski-Krastanov growth method.The study of photoluminescence suggests that there is critical annealing temperature whichcan be used to control the optical properties of QD-chains. The comparison of optical properties with structural images suggests that flattening of dot-chains is one of the reasons for a higheremission energy for QD-chains formed at a higher annealing temperature. The flattening may also result in opening up the non-radiative relaxation of excited carriers at room temperatureas the light emission decreases beyond the detection limit for one sample prepared at the critical annealing temperature.

Study of optical properties of novel quantum nanostructures (QNs) is important for optoelectronic device applications because the optical properties are directly related to their electronic structures. The understanding of electronic structure is necessary for designing novel optoelectronic devices based on QNs as the electronic properties can be correlated with growth parameters that control the size and compositional disorder of QNs.[1] Behaviors of excited carriers with temperature, especially near room temperature, have been studied extensively for their potential[1-5] in commercial devices such as QN-based lasers operating at room temperature.[6]

Recently a novel growth technique has been reported[7] that allows quantum nanostructures of different morphology, either quantum dots (QD), dashes[8] or dot-chains be produced depending on growth parameters. Annealing at higher than 460°C resulted in chaining of dots while self-assembly of regular QDs is observed when the strained-but-flat epilayers are annealed at temperatures lower than 440°C. An alternative route towards QD-chains has been also pursued, where a superlattice is formed by stacking alternating InGaAs/GaAs layers.[9] Broadenings of linewidth, full width at half maximum (FWHM), from 40meV to 85meV, are observed with increasing excitation intensity as well as with an increase in sample temperature although room temperature light emission from these QD-chains is not reported.[9]

In this work, we discuss the optical and morphological properties of the single stack of QD-chains that transform from the strained-but-flat epilayers during the annealing process. The photoluminescence (PL) spectra from the dot-chains are strong with narrow linewidths of ~23 meV when the annealing temperature is lower than 500°C.The annealing temperature has a critical impact on the optical properties. Increasing the annealing temperature to 500°C induced further flattening of dots in QD-chains and is accompanied by emission linewidth broadening and disappearance of PL peak signal at room temperature.

Commercially available n-type GaAs(001) substrate wafers were loaded into the growth chamber of a molecular beam epitaxy (MBE) machine via a preparation chamber.[10] After growth of a GaAs buffer layer over 500nm thick, the substrate was cooled down to 360°C, where deposition of a~10 monolayer (ML) thick InGaAs layer resulted in strained-but-flat surfaces with nominal indium composition around 37%.[7]Then the substrate temperature was ramped C at 20°C/min to a temperature higher than 460°, at which the InGaAs epilayers were annealed for 120 seconds in the growth chamber. When annealed at temperatures lower than 460°C, QDs without chaining can be obtained, as has been observed by *in-vacuum* scanning tunneling microscope (STM) imaging.[7] During the ramp-up and annealing period, the diffraction pattern at 2x orientation was monitored in real time for the transition from 2D to 3D by reflection high energy electron diffraction (RHEED). Details on how the technique of low temperature growth followed by high temperature annealing produces chains of dots can be found in references.[7,8,10] The samples were then transferred into the attached ultra-high vacuum (UHV) STM, Omicron 1, through a UHV port,[10] in order to obtain QD morphologies that are contamination free. Separate samples were grown with an additional 100 nm GaAs capping layer for photoluminescence (PL) measurements and transmission electron microscope images. The first 10nm of the cap were deposited on top of the InGaAs layer immediately after annealing; the remaining 90 nm were deposited at a temperature of 580°C, just before the sample was taken out of the MBE machine.

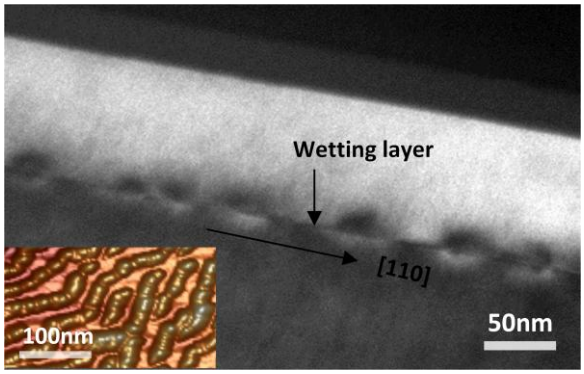

Figure 1. Cross-sectional, dark field (220) TEM image is obtained from a sample annealed at 460 °C. The specimen was lifted off the sample to expose the cross-sectional area that is perpendicular to the chaining direction [11b0] direction so that the wetting layer line (the dark line separating dots) is along the [110] direction. The inset at the bottom left corner is the STM image of uncapped dot-chains from the sample annealed at the same temperature, 460 °C.

For PL measurements, a cw Ti-Sapphire laser at 780 nm was focused onto the samples in a cryostat, with a spot diameter of200 micrometers and typical power of 50 mW. The emitted light from the samples was collimated and focused into an iHR320 (Horiba) 0.32 m spectrometer (grating blazed at 1000 nm, 600 line/mm) for wavelength selectivity. Light emerging from the spectrometer was then focused onto and detected with a ThorlabsPDF10C InGaAs detector. The laser beam was chopped at 20 Hz, and data collected with a standard lock-in technique.

Plan view and cross-sectional transmission electron microscopy (TEM) images of the capped samples were obtained using FEI Tecnai TF20 operating at 200 kV. A focused ion beam (FIB) was used to prepare TEM specimens from the PL-examined samples using a lift-off technique.

The TEM images confirm QDs, QD-chains and wetting layers after the growth of GaAs capping layers. The TEM image in Fig. 1was obtained from a sample annealed at 460°C, and shows the cross-sectional image

perpendicular to the chaining direction. The wetting layer, dark line between dots, is running along the [110] direction which is perpendicular to the chaining direction of dot-chains as shown[7] in the inset at the bottom left in Fig. 1.The inset is an STM image of *un-capped* dot-chains that were obtained from samples annealed at the same temperature. The comparison of the TEM image with the STM image suggests the measured base width and height of dots in dot-chains of the capped samples are similar to those[7] obtained from the STM images for the same annealing temperature.

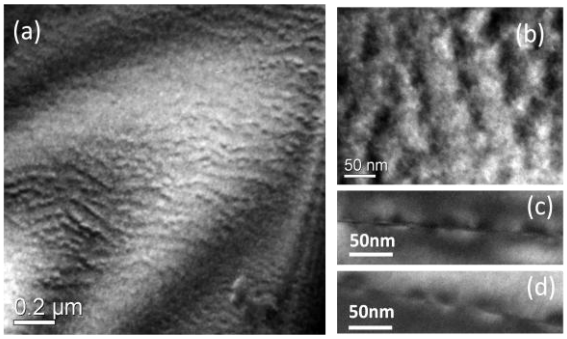

Figure 2. Plan view and cross-sectional TEM images obtained from a sample annealed at 500 °C. Large scale image shows dots are aligned to form chains. The rings in (a) are due to warping of the specimen. High resolution image (b) shows individual dots. The wetting layer line (the dark line separating dots) is along [110] direction as in Fig. 1. In order to illustrate the morphological evolution between the two annealing temperatures, a cropped out image from Fig. 1 (460°C anneal) is shown in (d).

It has been reported[7] that flattening of dots in the dot-chains occurs with temperature increase as confirmed by *as-grown* surface images of un-capped samples. It is apparent that chaining phenomena extend to even higher annealing temperatures up to 500°C. This is shown by large scale plan view TEM images. Plan view TEM images in Fig. 2 confirm that the dots are chaining along lines, which is similar to the reported STM images[7] seen from the uncapped samples that were annealed at temperatures lower than 500°C. Further flattening of dots with annealing temperature is observed, indicated by the cross-section TEM images. Flattening of dots is clearly shown in the images from Fig. 2-(c) and 2-(d), that smaller dots in height are induced at the higher annealing temperature of 500°C when compared with those annealed at 460°C. The observed morphological evolution, especially dot height confirms that the previously reported trend[7] of flattening of dots with annealing temperature persists through the capping process. The dot height can be estimated from the cross-section TEM image as ~5nm for QDs prepared by 500°C annealing while it is 8.3nm from STM images[7] and Fig. 2-(d) for QDs prepared by 460°C annealing. The size of QDs in Fig. 2-(a) to (c) is smaller than reported[11] InAs QDs with nominal deposition of 2nm but larger than that of 0.6nm deposition.

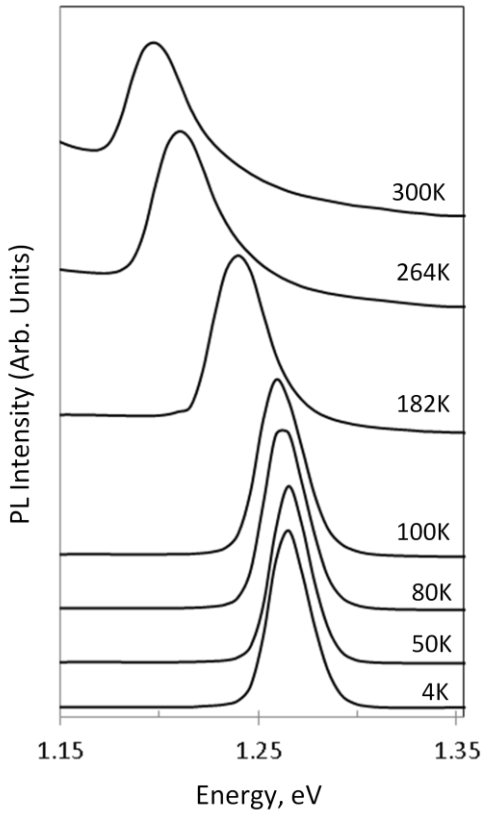

Figure 3. Normalized PL spectra from sample at various temperature with the excitation intensity of 160 W/cm2. The cross-sectional TEM view of this sample is shown in Fig. 1 along with the STM image of dot-chains.

Fig. 3 shows the change of PL spectra with temperature for the sample annealed at 460°C. The peak position shifts to lower energies at the temperature increases. The excitation intensity was 160 W/cm^2, and each

spectrum has been normalized by its maximum. Unlike PL emissions from stacked QD-chains,[9] no changes in peak position were observed at various excitation intensities ranging from 16 W/cm^2 to 1.6k W/cm^2 from all the samples examined. The state filling effect[6,12] was not observed over the excitation intensity used.

The peak energies are larger than those reported by InGaAs QDs grown by the conventional Stranski-Krastanov (S-K) growth method with nominal 50% indium composition and smaller nominal deposition amount of 6.5 ML but higher growth temperature of 530°C using MBE.[12] This can be attributed to the fact that larger indium composition may result in smaller transition energies.

The luminescence is clearly present at room temperature from our samples annealed at 460 and 480°C, althoughroom temperature intensities are much weaker than at low temperatures. However, for the samples annealed at 500°C, the PL emission intensity at room temperature goes below the detection limit. A recent study of PL emission from QDs in pulsed magnetic field reported that the laterally smaller dots increasingly dominate the PL emission at high temperature.[2] The TEM images in Fig. 2 indicate that the base width of QDs in dot-chains increases with annealing temperature. The disappearance of room temperature PL could therefore be due to the combined effect of flattening and broadening of dots at higher annealing temperature and higher emission energy (compared with those annealed lower than 500°C) which pushed the electronic energy states so close toward the continuum state of GaAs matrix that excited carriers spilled into the barrier material where the non-radiative recombinations[3] occur.

Similar shifts in peak position with temperature were also observed from the samples annealed at higher temperatures. Fig. 4-(a) shows that the peak energy stays the same up to 60K for samples annealed at 460°C and 40K for samples annealed at 480 and 500°C. The peak energies for the three samples are higher than those (~1.24 eV at 18K) reported from conventionally grown InGaAs QDs with similar indium composition of 40% with similar deposition amount of 10ML.[6]

For comparison, using the Varshni relationship[13] and the bandgap equation for InGaAs alloy with 40% indium,[14] bandgap change with temperature is also shown in the figure for unstrained InGaAs (40% indium) with modified value at zero kelvin. The QD-chains formed at 460 and 480°C annealing more-or-less follow the Varshni curve of the InGaAs alloy, while those formed at 500°C show faster red shifts over temperature than those from typical QDs.[1] This suggests that the QD-chains have different thermal escape behavior for excited carriers due to the difference in electronic states. The disappearance of the PL peak at room temperature over the all excitation intensities employed (as seen in the 500°C-annealed sample) is another characteristic of QDs formed with the conventional S-K growth method. Thus we see that the 500°C sample has similar electronic structures as those dots grown by the S-K method.

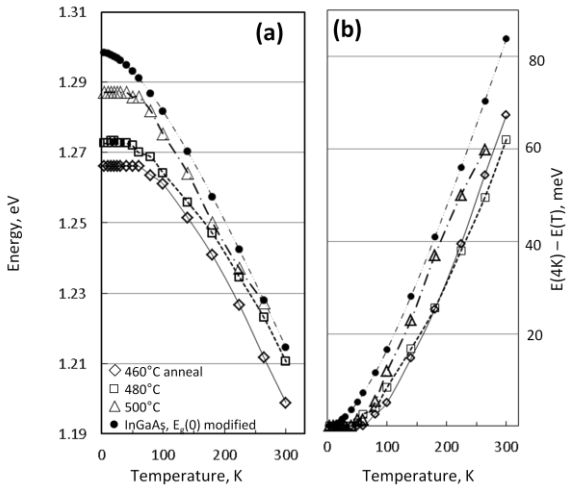

Figure 4. The change of peak position over temperature is shown in (a) while the relative difference of the peak energy from that of 4K is shown in (b). In (a), the bandgap change of bulk InGaAs over temperature is added with modified Eg(0) value for comparison.

The low temperature peak positions shown in Fig. 4-(a) for our three dot-chain samples, ~1.27-1.29 eV, are higher in energy than those reported for conventionally grown InGaAs QDs with a similar indium composition

of 40% and similar deposition amount of 10 ML (~1.24 eV at 18K).[6] This is unexpected. The growth of the conventional QDs in that reference was done at high temperature, in the range between 500 and 550°C. Because indium desorbs faster than gallium at high temperature,[15] one would expect high temperature growth to yield dots with a lower indium percentage, and a correspondingly higher peak energy. Our dot-chains, by contrast, were grown via strained-but-flat layers produced at a much lower temperature of 360°C, and even our annealing temperatures of 460, 480, and 500°C were lower than the growth temperature of those conventional dots. Thus our dot-chains very likely have a *lower* fraction of indium than those of Ref 6. Therefore the unexpectedly high peak energies in our samples must be a result of morphology, rather than composition. We attribute this to a flattening of the dots in our dot-chains, which must increase peak energies via an increased quantum confinement vertically despite a larger lateral size. TEM images in Fig. 2 indicate flattening of dots with annealing temperature, which confirms STM observations[7] of flattening of *un-capped* QDs with the annealing temperature.

The PL peak positions of our three dot-chain samples increase in energy with the annealing temperature. This follows the expected trend mentioned above of higher peak energies with higher growth temperatures; however, because the total annealing period of the sample annealed at 500°C is only three minutes longer than that of the sample annealed at 480°C, it seems unlikely for significant indium desorption to have occurred. Therefore we again attribute the blue-shift in peak energy with annealing temperature to a flattening of the dots in the dot-chains.

In addition to the peak positions of our samples being higher in energy than those of the conventional dots from Ref. 5 mentioned above, it is also interesting to note that the peak position of our 500°C-annealed sample is higher in energy than the 1.274 eV peak seen from a 15 ML thick (about 4 nm) InGaAs quantum well with 30% indium concentration at comparable temperature (20 K) [Ref 5]. Again this is surprising at first glance because the smaller indium concentration and smaller nominal thickness of the quantum well relative to our dot layer would be expected to result in a higher energy. In this case, it's likely that *lateral* confinement in our dot-chains is responsible for the increased peak energy of our sample relative to that quantum well. (The lateral extent of the dots in our dot-chains is visible in Fig. 2.)

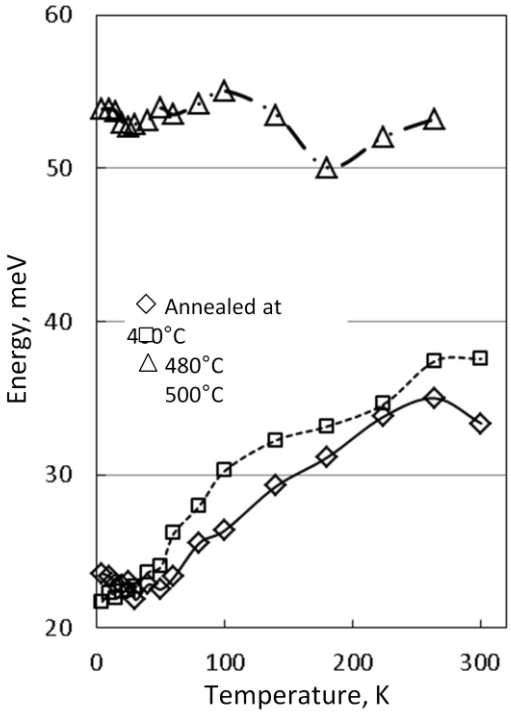

Figure 5. . Full width at half maxima (FWHM) of the emission peak are shown. There is a big increase in FWHM for the sample annealed at 500°C compared with those from samples annealed at lower temperatures; slight increase in FWHM over temperature is noted for the sample annealed at 480°C compared those from the sample annealed at 460°C.

The high quality of our dot-chains is evidenced by narrow PL peaks. As can be seen from Fig.5, the major peak of the 460°C and 480°C-annealed samples has a has full width at half maximum (FWHM) of 23 meV at 20K, which is much narrower than those from InGaAs QDs grown by MBE[6] with similar nominal composition of 40% indium and thickness of ~10ML,QDs by atomic layer epitaxy (ALE) with 50% indium composition,[4] and dot-chains[9]

in superlattice. The narrower linewidth suggests that QDs grown by the annealing technique result in a highly homogeneous distribution in size as the narrow linewidth has been attributed[6,16] to narrow size distribution of QDs grown both MBE[6,11] and ALE.[4] However, much larger linewidths (50-55meV) are observed from QD-chains when the annealing temperature increases to 500ºC. This suggests that the QD size distribution broadens critically at that temperature. The PL linewidth stays roughly constant with temperature for the 500ºC annealed sample while the linewidth increases with temperature for the samples annealed at lower temperatures.

The PL data indicate that the two samples annealed at 460°C to 480°C have similar electronic structure, evidenced by the similar emission spectra and linewidths over the temperature range. The similarity is surprising because the STM images from the uncapped sample surfaces indicate that the annealing temperature has a significant impact on the shape and size of dot-chains.[7] The dot-chains become larger laterally but shorter as they get flattened when the annealing temperature is increased by 20°C to 480°C.By contrast, the additional 20°C increase in annealing temperature from 480°C to 500°C (with its additional flattening and lateral size increase) clearly resulted in a large change in electronic structure.

In summary, we have studied the correlation between the optical and structural properties from QD-chains that are produced by annealing strained-but-flat epilayers. Strong PL emissions with rather narrow linewidths are observed from the samples examined. It is found that there is a critical annealing temperature above which the optical properties resemble QDs produced by the typical S-K growth technique, which is significant in the growth of material for optoelectronic devices. This novel growth approach, annealing strained-but-flat epilayers, may be useful for high quality optoelectronic devices operating at room temperature.

Financial support from the National Science Foundation, grant numbers CBET-0854313, CBET-1143543 and 1143543, is gratefully acknowledged. We note with sadness the passing of coauthor Steve Brown, who participated in the experimental phase of the work presented here.

Reference

[1] A. Polimeni, A. Patanè, M. Henini, L. Eaves, and P. C. Main, Physical Review B **59** (7), 5064 (1999).

[2] T. Nuytten, M. Hayne, M. Henini, and V. V. Moshchalkov, Physical Review B **77** (11), 115348 (2008).

[3] S. Sanguinetti, D. Colombo, M. Guzzi, E. Grilli, M. Gurioli, L. Seravalli, P. Frigeri, and S. Franchi, Physical Review B **74** (20), 205302 (2006).

[4] Kohki Mukai, Nobuyuki Ohtsuka, and Mitsuru Sugawara, Applied Physics Letters **70** (18), 2416 (1997).

[5] S. Fafard, S. Raymond, G. Wang, R. Leon, D. Leonard, S. Charbonneau, J. L. Merz, P. M. Petroff, and J. E. Bowers, Surface Science **361–362** (0), 778 (1996).

[6] K. Kamath, P. Bhattacharya, T. Sosnowski, T. Norris, and J. Phillips, Electronics Letters **32** (15), 1374 (1996).

[7] Dong Jun Kim, E. Addison Everett, and Haeyeon Yang, Journal of Applied Physics **101** (10), 106106 (2007).

[8] Kim Dong Jun and Yang Haeyeon, Nanotechnology **19** (47), 475601 (2008).

[9] Yu I. Mazur, W. Q. Ma, X. Wang, Z. M. Wang, G. J. Salamo, M. Xiao, T. D. Mishima, and M. B. Johnson, Applied Physics Letters **83** (5), 987 (2003).

[10] Dong Jun Kim, Deokjoon Cha, Gregory J. Salamo, and Haeyeon Yang, Journal of Vacuum Science & Technology B: Microelectronics and Nanometer Structures **24** (6), 2776 (2006).

[11] M. Grundmann, J. Christen, N. N. Ledentsov, J. Böhrer, D. Bimberg, ‡ S. S. Ruvimov, P. Werner, U. Richter, U. Gösele, J. Heydenreich, V. M. Ustinov, A. Yu Egorov, A. E. Zhukov, P. S. Kop'ev, and Zh I. Alferov, Physical Review Letters **74** (20), 4043 (1995).

[12] S. Raymond, S. Fafard, P. J. Poole, A. Wojs, P. Hawrylak, S. Charbonneau, D. Leonard, R. Leon, P. M. Petroff, and J. L. Merz, Physical Review B **54** (16), 11548 (1996).

[13] Y. P. Varshni, Physica **34** (1), 149 (1967).

[14] K. H. Goetz, D. Bimberg, H. Jurgensen, J. Selders, A. V. Solomonov, G. F. Glinskii, and M. Razeghi, Journal of Applied Physics **54** (8), 4543 (1983).

[15] J. P. Reithmaier, H. Riechert, H. Schlötterer, and G. Weimann, Journal of Crystal Growth **111** (1–4), 407 (1991).

[16] R. P. Mirin, J. P. Ibbetson, K. Nishi, A. C. Gossard, and J. E. Bowers, Applied Physics Letters **67** (25), 3795 (1995).

Index

Cross-section, 22, 34
Cryostat, 14

Diffraction contrast, 17

Epitaxy, 7

Full width at half maximum, 32

Intermixing, 10

Mass-thickness contrast, 17
Molecular Beam Epitaxy, 27

Nanostructures, 2

Partial electron energy-loss spectrometry, 19, 35
Photoluminescence, 1, 12, 14, 26
Plan View, 22, 36

Quantum dots, 2
Quantum well, 5

Scanning transmission electron microscopy, 17
Segregation, 10
State filling effect, 29
Stranski-Krastanov, 29

Time-resolved photoluminescence, 1
Transmission electron microscopy, 2, 15, 20, 34
    Scanning, 17
Tunneling, 5
Two-beam condition, 17

Varshni relationship, 29

X-ray energy dispersive spectrometry, 19, 35